

Machine Learning Assisted Signal Enhancement

by

Longfei Felix Yan

A thesis
submitted to the Victoria University of Wellington
and the Australian National University
in fulfilment of the
requirements for the degree of
Doctor of Philosophy
in Engineering.

Victoria University of Wellington
Australian National University
2024

Abstract

In an era of abundant signals, the ability to obtain desired signals while rejecting undesired ones has become increasingly crucial. Often, the desired signals are mixed with interference or contaminated by noise. Signal enhancement techniques play a vital role in performing tasks such as signal separation, extraction, and suppression. This thesis addresses critical challenges in signal enhancement tasks by harnessing the power of machine learning techniques.

Firstly, we propose a novel independence criterion called the Finite Basis Independence Criterion (FBIC). This criterion estimates the Hirschfeld-Gebelein-Rényi maximum correlation coefficient between tested variables and is based on mapping functions from a subspace of finite basis. FBIC detects dependence between variables in linear time and outperforms more computationally expensive kernel-based counterparts. Extensive testing in Independent Component Analysis benchmarks demonstrates its potential for various signal separation applications.

Secondly, we conduct a comprehensive robustness analysis of a popular signal enhancement approach: fixed beamforming based on first-order linear Differential Microphone Arrays (DMAs). We demonstrate that both bounded and unbounded phase errors of microphones can affect the mainlobe orientation of the beamformer. Analytically derived white noise gain thresholds indicate when mainlobe misorientation occurs. Through rigorous mathematical derivations, we prove that a higher number of microphones and increased spacing between microphones contribute to the robustness of the beamformer. This work provides practical guidelines for designing robust first-order linear DMAs.

Thirdly, we propose a neural network model to optimize both the geometry and spatial filter of linear DMAs. The model consists of two feed forward neural networks and is trained end-to-end. The signals enhanced by this model exhibit superior quality compared to those obtained from conventional DMA approaches. Furthermore, the model offers flexibility in controlling the tradeoff between different performance metrics, allowing for customized optimization.

Lastly, we extend the neural network model to a general framework that allows optimization of microphone arrays of any geometry, along with their spatial filters. This model employs ResNets and augmented Lagrangian techniques to achieve state-of-the-art frequency-invariant fixed beamforming performance. We showcase our performance in linear, circular, and concentric circular microphone arrays. Moreover, our findings challenge the conventional belief that concentric circular arrays require multiple rings, as we demonstrate that good performance can be achieved with only one ring.

Overall, this thesis contributes novel techniques and insights to the field of signal enhancement, leveraging machine learning approaches to address key challenges. The proposed criteria, guidelines and models have the potential to advance various signal separation applications and enhance the overall quality of processed signals.

Acknowledgments

First and foremost, I would like to express my profound gratitude to my esteemed supervisors, Bastiaan Kleijn and Thushara Abhayapala. Their constant guidance, invaluable insights, and professional advice have been indispensable throughout my PhD journey.

I am deeply grateful to David Balduzzi for opening the door to the world of academia for me. His initial encouragement and support laid the foundation for my research endeavors.

I extend my heartfelt appreciation to the dedicated members of the university staff who have provided invaluable assistance along the way. My sincere thanks go to Paul Teal, Prasanga Samarasinghe, Steven Archer, Hui Ma, Yi Mei, and Peter Andreae (Pondy) for their support and contributions.

I am grateful for the financial support generously provided by Victoria University of Wellington and the Australian National University. I am also grateful for the financial support provided by my mother. Their sponsorship has enabled me to focus on my research and has been instrumental in the successful completion of my PhD.

Furthermore, I would like to acknowledge and embrace the failures and obstacles encountered during my research journey. As the saying goes, "what does not kill me makes me stronger." These challenges have undoubtedly contributed to my growth and development as a researcher.

I would also like to extend my heartfelt appreciation to my friends and colleagues who have been an integral part of my PhD years. Your support

and encouragement have been invaluable to the completion of my doctoral studies. I am particularly grateful to Sachi Dhula, Vanamali Gopal, Daniel Braithwaite, Ganlong Wang, Kelson Chua, Matt O'Connor, Steven Van Kuyk, Kurt Ma, Wageesha Manamperi, Aimee Zhang, June Sun and Fei Ma for their camaraderie and assistance.

Importantly, I am eternally grateful to my partner, Yunshi Xiao. Your unswerving moral and emotional support have been the pillars of strength that made my PhD mission possible. Thank you for choosing to stand by me during the most challenging times, even when I was emotionally overwhelmed. I am forever indebted to your boundless love and support. I am also grateful to Yunshi's parents, Tiyong Xiao and Darong Wu, who have been selfless supporters of our relationship and life.

Lastly, I want to dedicate my thesis to my deceased grandma, Guifen Huang, who always valued my life more than her own. I would not have survived in this world without her nurturing, let alone pursue a PhD. My life is a continuation of her life, and my love for others originates from her.

Contents

1	Introduction	1
1.1	Problem Statement	1
1.2	Motivations	5
1.2.1	Independence Criteria	6
1.2.2	Robustness Analysis of First-Order Linear DMAs	7
1.2.3	Fixed Beamforming on Linear Array	8
1.2.4	Fixed Beamforming with Flexible Geometry	9
1.3	Contributions, Publications and Thesis Organization	10
1.3.1	Contributions	10
1.3.2	Publication list	11
1.3.3	Thesis Organization	11
2	Background	15
2.1	Independence Criteria	15
2.1.1	Maximal Correlation	16
2.1.2	Mutual Information	17
2.1.3	Integral Probability Metric	20
2.2	Artificial Neural Network	21
2.2.1	Common Structures of ANNs	21
2.2.2	ResNet	24
2.2.3	Neural Ordinary Differential Equations	24
2.2.4	Multichannel Variational Autoencoder (MVAE)	26

2.2.5	Multi-Resolution Convolutional Autoencoder (MR-CAE)	27
2.2.6	Beta VAE	28
2.2.7	FactorVAE	30
2.2.8	Training of ANNs	31
2.3	Microphone Array Fixed Beamforming	33
2.3.1	Notations	34
2.3.2	Delay-and-Sum	35
2.3.3	Maximum Directivity Factor	38
2.3.4	Differential Beamforming	41
2.4	Mathematical Derivations	47
2.4.1	Minimum Norm Solution	47
2.4.2	Verify Positive Semidefinite Matrix	48
2.4.3	Trace of Matrix Product	49
2.4.4	Trace Inequality	49
2.4.5	Condition Number for Inversion	50
3	Linear Time Finite Basis Independence Criterion	51
3.1	Introduction	52
3.2	Background	55
3.2.1	RKHS-based Independence Measures	55
3.2.2	From HSIC to FSIC	57
3.3	FBIC	62
3.3.1	Definition of FBIC	63
3.3.2	Basis Functions in FBIC	64
3.3.3	Justifications for FBIC	65
3.3.4	Computational Complexity	67
3.3.5	FBIC vs FSIC	68
3.4	Experimental Studies	69
3.4.1	Simulated Data	69
3.4.2	Preprocessing	70

3.4.3	Neural Network settings	71
3.4.4	Parameter Choices for RBFs	72
3.4.5	Multi-Channel Extension of FBIC	76
3.4.6	Results and Discussions	76
3.5	Conclusions	79
4	Robustness Analysis of First-Order Linear Differential Microphone Arrays	81
4.1	Introduction	82
4.2	Background	83
4.2.1	Signal Model	83
4.2.2	Metrics of First-Order LDMA	84
4.3	Analysis of Gain Errors	85
4.4	Analysis of Phase Errors	87
4.4.1	Analysis of Bounded Phase Errors	87
4.4.2	Analysis of Unbounded Phase Errors	91
4.5	Experimental Results	93
4.6	Conclusion	95
5	Neural Optimization of Non-Uniform Linear Arrays	99
5.1	Introduction	99
5.2	Signal Model	102
5.3	Performance Measures	103
5.4	Models For Geometry Optimization	104
5.4.1	PSO Models	104
5.4.2	NONULA	105
5.5	Experimental Results	107
5.6	Conclusion	110
6	Geometrically Optimized Neural Fixed Beamformers	115
6.1	Introduction	116
6.2	Signal Model and Problem Formulation	119

6.3	Performance Measures	124
6.4	DMA Beamformers	126
6.5	Neural Network Model	128
6.5.1	Loss Function	132
6.6	Experiments	134
6.6.1	Neural Network Training Details	134
6.6.2	Linear Array	134
6.6.3	Circular Array	135
6.6.4	Validation of ResBlocks Design	137
6.6.5	Concentric Circular Array	139
6.6.6	Arbitrary Discal Array	141
6.7	Conclusions	144
7	Conclusions and Future Research	147
7.1	Conclusions	147
7.2	Future Work	148
7.2.1	Multi-channel Speech Separation Guided by Independence Criteria	149
7.2.2	Disentanglement	149
7.2.3	Fixed Beamforming with Rectangular Arrays	150

Chapter 1

Introduction

This chapter first provides an introductory overview of the research problem that we aim to address. Next, we discuss the motivations behind our research findings, presenting the driving factors that have guided our work. Finally, we outline the contributions made, highlight our publications, and provide a clear organizational structure for the thesis. This opening chapter sets the stage for the subsequent chapters, laying a strong foundation for the exploration and presentation of our research journey.

1.1 Problem Statement

A signal can be perceived as a time-dependent function [137] that conveys valuable information pertaining to various systems or phenomena. Natural signals are omnipresent in our surroundings, allowing us to perceive them through different senses. We hear signals in the form of acoustic waves, see signals through light waves, and feel signals in the guise of thermal radiation. Additionally, signals can be artificially generated using electrical quantities, enabling us to record, transmit, and analyze them using digital signal processing techniques.

In the era of information, the ability to identify and gather the desired information has become significantly imperative. However, information

seldom arrives in a pure state, making the acquisition of relevant data highly dependent on signal enhancement techniques. These techniques involve the separation and extraction of pertinent signals while suppressing irrelevant ones. Certain signal enhancement tasks tap into the innate capabilities of humans. For instance, individuals possess exceptional aptitude in discerning the target speaker amidst a cacophony of simultaneous speeches and noises, a scenario commonly referred to as the "cocktail party problem" [25]. The endeavor to impart similar signal enhancement abilities to machines is an actively pursued research area.

Blind Source Separation (BSS) is a powerful signal separation technique that enables the extraction of original independent source signals when only the mixed observed signals are available [111]. The term "blind" emphasizes the lack of prior knowledge regarding both the input signals and the mixing system [93]. Over the past two decades, BSS has gained widespread recognition and utilization due to its profound theoretical underpinnings and practical applicability.

Numerous methodologies have been proposed to tackle BSS problems, including notable approaches like Independent Component Analysis (ICA) and Non-negative Matrix Factorization (NMF) [123, 110]. Among these methods, ICA stands out as one of the earliest and most widely adopted techniques [123]. The fundamental premise underlying ICA is the assumption of statistical independence among the original sources [30]. From a probabilistic standpoint, the concept of statistical independence among signals suggests that the joint probability density function of the signal mixture can be decomposed into the product of the marginal probability density functions pertaining to each individual source signal. By unveiling the latent components within the observed signal mixtures, ICA effectively reconstructs the original source signals, offering a powerful means of signal separation and recovery.

Various ICA methods utilize different contrast functions to quantify the statistical independence of output components [175]. These functions

can be constructed using measurements on statistical quantities such as non-Gaussianity, mutual information, and cross-cumulants [75, 5, 18]. Recently, there has been a growing interest in utilizing measurements in the Reproducing Kernel Hilbert Space (RKHS), which has demonstrated superior performance in detecting statistical dependence [3, 55]. In their work, Bach and Jordan proposed a kernel method to search for mapping functions in the RKHS that can achieve maximal correlation between observed signals, known as Kernel ICA. This approach exhibits robustness to source densities, near-Gaussianity, and outliers [3]. Furthermore, the Hilbert Schmidt Independence Criterion (HSIC) introduced by [55] has shown the most promising performance among kernel-based methods to date. HSIC, based on an integral probability metric, searches for RKHS functions that maximize the norm of the cross-covariance operator. It demonstrates robustness under challenging environments and sensitivity to small deviations from independence.

In scenarios where additional information about the target signals is available, such as sensor locations and the direction of the source signal, beamforming techniques can be effectively employed for signal enhancement. Unlike signal separation methods, beamforming excels at attenuating signals originating from unwanted directions while enhancing the signal-to-noise ratio of the desired signals. This is accomplished by creating a beam-like reception pattern in the desired direction through the application of spatial filters that adjust the phases and weights of the received signals [160]. As a result, beamforming techniques find widespread applications in signal enhancement fields such as sonar, radar, and antenna array processing [10].

Speech signal enhancement tasks commonly leverage the benefits of beamforming techniques through the utilization of microphone arrays. By employing beamforming, it becomes possible to enhance speech quality and intelligibility by mitigating interference signals, reverberation, and noise. In scenarios where the acoustic environment remains stationary or

prioritizing robustness is crucial, fixed beamforming techniques prove to be particularly advantageous for microphone arrays. These techniques employ fixed spatial filters that are independent of the input data, enabling consistent and reliable performance.

Frequency-invariant fixed beamforming has gained significant attention from researchers in addressing artifacts caused by distorted frequency responses, particularly in broadband speech signals. Over the past two decades, Differential Microphone Arrays (DMAs) have emerged as a popular choice for fixed beamforming due to their ability to provide a relative frequency-invariant approach for processing speech signals [9]. Moreover, DMAs exhibit compact apertures as they approximate the differential acoustic pressure field, making them highly feasible for implementation. In comparison to conventional fixed beamformers such as Delay-and-Sum (DS) and superdirective beamformers [10], DMAs offer more balanced Directivity Factors (DFs) and White Noise Gains (WNGs).

The order of DMAs corresponds to the order of the differential acoustic pressure field. Traditional DMAs employ a direct derivative definition, achieved by subtractively combining microphone outputs, which necessitates $N + 1$ microphones to construct an N th-order DMA [40]. However, this approach lacks flexibility when designing beampatterns of varying orders. To address this limitation, [6] proposes utilizing the short-time Fourier Transform (STFT) domain to design DMAs in each subband. This technique enables the approximation of target beampatterns using MacLaurin's series or Jacobi-Anger expansion [178]. Nonetheless, the presence of unavoidable approximation errors can impact the performance of the approximated beampattern. Alternatively, in [10], the authors suggest employing null-constrained linear systems to derive spatial filters for DMAs. This approach draws inspiration from the observation that the order of DMAs corresponds to the number of nulls in the beampattern.

Several geometry settings of DMAs have been thoroughly investigated in prior research. These include the uniform linear array [69], non-uniform

linear array [131], uniform circular array [7], and uniform concentric circular array [165]. Among these configurations, non-uniform linear arrays have been found to better accommodate the frequency-invariant requirement of speech signals for linear DMAs [79]. On the other hand, for circular and concentric circular DMAs, null-constrained methods have demonstrated superior performance by effectively mitigating deep null problems [165].

In recent years, machine learning has experienced remarkable advancements across various domains, leveraging its ability to automatically learn optimal parameters for problem-solving purposes [48]. Various learning paradigms, including supervised learning, unsupervised learning, and reinforcement learning, have been extensively investigated, unleashing the potential of machine learning techniques. Considering the vital role of parameter estimation in signal enhancement tasks, it is only natural to explore and exploit machine learning methods in this field. However, the application of machine learning in blind source separation (BSS) and fixed beamforming has been somewhat limited thus far. Despite its potential, machine learning remains relatively underutilized in these specific areas, leaving ample room for exploration and further advancements.

This thesis aims to address the under-utilization of prevalent machine learning techniques in the realm of signal enhancement, with a particular focus on BSS and fixed beamforming tasks. By bridging this gap and harnessing the untapped potential of machine learning in BSS and fixed beamforming, we can potentially achieve breakthroughs and introduce various applications in signal enhancement .

1.2 Motivations

In this section, we will delve into the limitations of existing research and outline the motivations behind our own investigation across four key areas: independence criteria, robustness analysis of first-order LDMA, fixed

beamforming on linear arrays, and fixed beamforming with flexible geometry.

1.2.1 Independence Criteria

The existing measures of independence for signal separation exhibit certain limitations. Take HSIC, for instance, which, despite its advantages, is accompanied by certain trade-offs. The computation of independence using HSIC is significantly slowed down due to its quadratic computational time. Moreover, when dealing with input signal sample sizes exceeding 6000, the utilization of HSIC for statistical independence calculation becomes impractical [81]. This drawback becomes particularly critical in the context of the current era of big data. Furthermore, it has been observed that HSIC lacks guaranteed stability, being sensitive to initial conditions. In ICA experiments, if the initial demixing matrix is not appropriately estimated, HSIC may encounter issues such as converging to local optima and exhibiting poor performance [148].

To overcome the computational inefficiency of HSIC, an alternative criterion called the Finite Set Independence Criterion (FSIC) has been developed as a subsequent solution [81]. Rather than constructing a Gram matrix that involves pairwise computations between every single pair of signal observations, FSIC selects a finite set of test locations to compare with the input signals. Empirical evidence has demonstrated that a small set of test locations is sufficient to achieve adequate testing power [81]. This characteristic allows FSIC to operate in linear time, making it a more efficient algorithm. By focusing on the key regions captured by the selected test locations, which indicate the differences between two input signals, the estimation of the covariance matrix becomes more efficient and accurate.

To identify key regions and optimize kernel parameters, FSIC necessitates the division of data into training and test sets. Only the training

set is utilized for parameter tuning to prevent overfitting, while the test set is solely employed for independence measurement. However, this approach presents two inherent challenges. Firstly, the training stage of FSIC inhibits its suitability as an online algorithm. Secondly, the task of data splitting itself can be problematic. For instance, if the data distribution lacks stationarity, there is a high likelihood that the training set will fail to accurately reflect the true properties of the test set. These drawbacks render the integration of FSIC into contemporary machine learning algorithms for signal separation laborious and impractical.

1.2.2 Robustness Analysis of First-Order Linear DMAs

Linear DMAs commonly encounter challenges such as white noise amplification and microphone mismatches [34, 177, 37, 16]. By investigating the robustness of first-order DMAs, we can develop a deeper understanding of how higher-order linear DMAs exhibit robustness. Additionally, the principles derived from this robustness analysis can be utilized to inform the design of robust first-order linear DMAs.

In [24], a comprehensive robustness analysis is conducted on linear DMAs approximated by Maclaurin Series, focusing specifically on the phenomenon of Mainlobe Orientation Reversal (MOR). The authors confirm that microphone gain errors in first-order linear DMAs do not lead to the MOR phenomenon. To analyze the effect of microphone phase errors, they introduce a crucial parameter χ in Equation (26) of their work:

$$\chi = \frac{-3}{2M-1} \left[\psi_1(\omega) - \frac{2 \sum_{m=2}^M (m-1) \psi_m(\omega)}{M(M-1)} \right], \quad (1.1)$$

where M represents the total number of microphones in the array, and $\psi_m(\omega)$ denotes the phase error associated with the m th microphone at angular frequency ω . Through mathematical derivations, the authors demonstrate that MOR occurs when $\chi < 0$. However, it is important to note that

their subsequent analysis implicitly assumes a strong condition regarding the microphone phase errors $\psi_m(\omega)$, namely that these phase errors are nearly identical. This assumption is illustrated in their Equation (48), where $\Delta\psi$ is employed to replace individual $\psi_m(\omega)$ values.

The strong assumption of nearly identical microphone phase errors, as presented in [24], is not practical as it does not reflect real-life conditions. In practical scenarios, phase errors commonly vary across different microphones. Therefore, the conclusion drawn in [24] regarding microphone phase errors cannot be generalized to real-world situations.

1.2.3 Fixed Beamforming on Linear Array

Speech signals are broadband, ranging from a few hundred to a few thousand Hertz ([31]). Uniform linear arrays are suboptimal for processing such broadband signals due to the challenges they pose in avoiding spatial aliasing and white noise amplification. Uniformly large spacing in linear arrays leads to spatial aliasing, while uniformly small spacing makes the arrays susceptible to white noise [6, 9, 170]. To address this dilemma, researchers have explored various non-uniform linear array designs.

One approach for designing non-uniform linear arrays involves utilizing convex optimization techniques [95]. To reformulate the array optimization as a convex problem, discrete potential microphone positions must be selected in advance. Choosing the optimal microphone positions from the pre-selected positions becomes a mixed-integer problem. Unfortunately, this problem is NP-hard, which means that its computational complexity exponentially increases with the number of microphone position candidates. Consequently, achieving the global optimal solution through this method is infeasible.

Another approach to non-uniform linear array optimization utilizes Particle Swarm Optimization (PSO) [131]. However, this approach has a significant drawback in that it fails to satisfy the distortionless constraint.

As a result, undesirable artifacts can occur across frequency bands, compromising the quality of received signals. Furthermore, this approach relies on DMAs that are not robust at low frequency bins.

1.2.4 Fixed Beamforming with Flexible Geometry

Fixed beamforming has been extensively investigated across various geometry settings, encompassing linear arrays [69], circular arrays [7], and concentric circular arrays [165], among others. Each geometry exhibits its own set of advantages and disadvantages. For instance, linear arrays offer excellent directionality towards the end-fire direction but lack flexibility in steering. While each geometry has been individually examined, a unified framework that enables consistent study of all geometry settings from a neural network perspective is yet to be established.

Prior fixed beamformers primarily rely on DMAs, which strike a favorable balance between DFs and WNGs compared to DS or superdirective beamformers [9]. Nevertheless, the issue of white noise amplification at low frequencies remains a fundamental challenge for DMAs that has not been adequately addressed. Additionally, many of the target beampatterns of DMAs are either derived from empirical experience or optimized with respect to a single performance metric. For instance, the hypercardioid beampattern exhibits optimal DFs but suffers from low WNGs. Moreover, the null-constrained approach of DMAs also exhibits drawbacks, as the key parameters, such as null directions, are manually selected by human experts. These issues collectively impede the performance of fixed beamformers from achieving a globally optimal perspective.

Circular DMAs are particularly susceptible to deep null problems, wherein array performance experiences severe degradation at specific frequencies. In [67], the authors attribute deep nulls to zero values of the Bessel function when employing the Jacobi-Anger expansion for beampattern ap-

proximation. However, similar deep null problems have been observed in the DMA approach based on MacLaurin series and null-constraints. To alleviate these deep nulls, [165] suggests increasing the number of rings in circular DMAs.

1.3 Contributions, Publications and Thesis Organization

This section serves to provide a concise summary of our research contributions and highlights the publications we have produced throughout the course of my PhD journey. Furthermore, we outline the organization of the thesis and establish the connections between the thesis chapters and our published works. By presenting this overview, readers can gain a clear understanding of our research endeavors and the cohesive structure of our thesis in relation to our publications.

1.3.1 Contributions

In this thesis, our primary focus is to address crucial challenges in signal enhancement through the application of both machine learning and signal processing techniques. Signal enhancement encompasses the tasks of signal separation, extraction, and suppression. Firstly, we present a linear-time independence criterion that serves as a valuable guide for ICA algorithms and other signal separation applications. Secondly, we look into a comprehensive analysis of the robustness of first-order linear DMAs, addressing misunderstandings that exist within the research community. To this end, we establish new WNG thresholds that facilitate effective fixed beamforming. Thirdly, we propose a neural network-based model specifically designed to optimize linear microphone arrays, achieving improved enhancement of target signals while effectively suppressing unwanted interference and noise. Finally, we extend our neural network model to a

general framework capable of accommodating arrays with diverse geometric configurations, allowing for enhanced signal processing in arrays of any given geometry.

1.3.2 Publication list

The publications listed below are completed as part of my PhD research. They are either peer-reviewed or going to be peer-reviewed:

1. "A linear-time independence criterion based on a finite basis approximation." International Conference on Artificial Intelligence and Statistics (AISTATS). PMLR, 2020.
2. "Phase Error Analysis for First-Order Linear Differential Microphone Arrays." 2022 International Workshop on Acoustic Signal Enhancement (IWAENC). IEEE, 2022.
3. "Neural Optimization Of Geometry And Fixed Beamformer For Linear Microphone Arrays." 2023 IEEE International Conference on Acoustics, Speech and Signal Processing (ICASSP). IEEE, 2023.
4. "Neural Optimization of Fixed Beamformers with Flexible Geometric Constraints". To be submitted to an IEEE transaction.

1.3.3 Thesis Organization

This thesis consists of seven chapters in total. A summary of the six following chapters are given below.

Chapter 2: Background

This chapter introduces essential background knowledge and literature review that are pertinent to our research contributions. The research background of three key areas is elaborated upon, namely: independence criteria, artificial neural network, and microphone array fixed beamforming.

Furthermore, this chapter presents relevant mathematical derivations to enhance readers' understanding.

Chapter 3: Linear Time Finite Basis Independence Criterion

This chapter is based on the peer-reviewed publication titled "A linear-time independence criterion based on a finite basis approximation". It proposes a linear-time independence criterion that is an upper bound of the maximum correlation coefficient. Through extensive testing on classic ICA benchmarks, our proposed independence criterion demonstrates exceptional performance, surpassing kernel methods like HSIC and FSIC, thus establishing a new state-of-the-art standard.

Chapter 4: Robustness Analysis of First-Order Linear Differential Microphone Arrays

This chapter is grounded in the peer-reviewed publication titled "Phase Error Analysis for First-Order Linear Differential Microphone Arrays". It presents a thorough analysis of both bounded and unbounded phase errors in first-order linear DMAs. In particular, we establish WNG thresholds that effectively prevent mainlobe misorientation of the beamformer beampattern. Furthermore, through rigorous analytical proofs, we demonstrate that increasing the number of microphones and the spacing between them can enhance the robustness of first-order linear DMAs. This work illuminates the path for designing robust first-order LDMA.

Chapter 5: Neural Optimization of Non-Uniform Linear Arrays

This chapter is founded on the peer-reviewed publication titled "Neural Optimization Of Geometry And Fixed Beamformer For Linear Microphone Arrays." It introduces a novel neural network model that enables the joint optimization of both the array geometry and the spatial filter of a fixed beamformer. This end-to-end model consists of two feedforward

neural networks. Through extensive experiments, we have demonstrated that our model surpasses previous DMA-based approaches, achieving superior overall scores and performance.

Chapter 6: Geometrically Optimized Neural Fixed Beamformers

This chapter builds upon the manuscript titled "Neural Optimization of Fixed Beamformers with Flexible Geometric Constraints" and serves as an extension of the previous chapter. It establishes a unified neural network framework for fixed beamformers with arbitrary geometric configurations. Specifically, the chapter delves into three distinct geometric settings: linear, circular, and concentric circular arrays. The proposed neural network model leverages ResNets and incorporates augmented Lagrangian in the loss function, enabling geometry optimization beyond traditional linear arrays. Through experimental analysis, we demonstrate that our model constructs frequency-invariant fixed beamformers that significantly outperform previous DMA-based frequency-invariant counterparts. Notably, we uncover that a concentric circular array can achieve impressive performance even with a single ring. Lastly, we showcase how our model achieves global optima in a straightforward arbitrary discal geometric setting.

Chapter 7: Conclusions and Future Research

This concluding chapter provides a comprehensive summary of our research spanning from Chapter three to Chapter Six, encapsulating the key findings and contributions of this thesis. Additionally, we outline potential future research directions that stem from our research endeavors, offering valuable insights into areas for further exploration and advancement.

Chapter 2

Background

In this chapter, we present the essential background that underlies our research contributions in Chapters Three to Six. Specifically, we will discuss the independence criteria, artificial neural networks, and microphone array fixed beamforming, which are critical for understanding our work. Moreover, we provide mathematical derivations that are related to the context of our research at the end of this chapter.

2.1 Independence Criteria

The measurement of statistical dependence between random variables has played a pivotal role in the fields of statistics and machine learning. Independence criteria have diverse applications, including but not limited to hypothesis testing [55], feature extraction [33], blind source separation [172], disentanglement [22], fairness measurement [52], and backpropagation-free neural network training [109]. This section will provide an overview of several popular categories of independence criteria, along with their advantages and drawbacks. Specifically, we will discuss independence criteria based on maximal correlation, mutual information and integral probability metric.

2.1.1 Maximal Correlation

The Pearson correlation coefficient, introduced by Pearson in his paper titled "Contributions to the Mathematical Theory of Evolution" [132], is a statistical measure that quantifies the strength of the linear relationship between two random variables. It is calculated by dividing the covariance of the two variables by the product of their standard deviations, thus measuring the normalized covariance between the two variables. However, it is important to note that the Pearson correlation only captures linear relationships and cannot reflect more complex relationships between variables. Additionally, it is important to exercise caution in interpreting the results of Pearson correlations as correlation does not necessarily imply causation, and there may be other variables at play. The Pearson correlation coefficient ranges from -1 to 1, where -1 indicates a perfect negative correlation, 1 indicates a perfect positive correlation, and 0 indicates no linear correlation. Despite these limitations, the Pearson correlation has been widely used in many disciplines due to its simplicity and ease of interpretation.

The Hirschfeld-Gebelein-Rényi (HGR) maximum correlation coefficient, also known as the maximal correlation ρ_{\max} , was proposed to address the limitations of the Pearson correlation coefficient in capturing nonlinear relationships between variables [63, 44, 139]. The maximal correlation is one of the earliest criteria for independence and satisfies the seven postulates specified by Rényi [139]. The fourth postulate states that $\rho_{\max}[\alpha, \beta] = 0$ if and only if the tested random variables α and β are independent. By definition and the sixth postulate of Rényi, the maximal correlation is the supremum of the possible Pearson correlation coefficients between the mapped random variables, where the mapping functions are Borel-measurable and square-integrable. In other words, the maximal correlation measures the maximum possible correlation that can be achieved between the mapped random variables, where the mapping functions are

flexible and allow for nonlinear relationships. This is expressed as

$$\rho_{\max}[\alpha, \beta] = \rho_{\max}[f_1(\alpha), f_2(\beta)], \quad (2.1)$$

where f_1 and f_2 are the mapping functions.

In [14], the authors proposed the Alternating Conditional Expectations (ACE) algorithm as a non-parametric approach to estimate the maximal correlation between two variables. This algorithm assumes little about the data distribution and function space, and optimizes the mapping functions in an iterative manner. Another approach to estimating the maximal correlation is to use Reproducing Kernel Hilbert Space (RKHS) as the function space [3]. This method is related to the ACE algorithm in that both seek to compute the largest generalized eigenvalue. The RKHS approach uses kernel functions to map the input variables into a high-dimensional feature space, where the maximal correlation can be computed using matrix eigenvalue decomposition.

2.1.2 Mutual Information

Mutual information is a fundamental concept in information theory that quantifies the amount of uncertainty reduction of one random variable given the observation of the other random variable. It measures the mutual statistical dependence between two random variables. While mutual information does not satisfy all of the postulates specified by Renyi, it has become a popular independence criterion due to its appealing interpretability and strong theoretical foundation, resulting from its calculation in entropy. Additionally, mutual information can be defined as the Kullback-Leibler (KL) divergence between the joint distribution of two random variables and the product of their marginal distributions.

Conventionally, mutual information can be estimated by binning the data and construct histograms. However, binning is sensitive to the choice of origin and bin width, which can lead to poor performance. One way to

address the histogram sensitivity issue is by using Kernel Density Estimators (KDE) [119], which estimates probability densities in a non-parametric manner. Compared to the conventional binning approach, KDE offers three advantages. Firstly, KDE has a better rate of convergence to the underlying probability density. Secondly, KDE is not sensitive to the choice of origin. Lastly, KDE can apply non-rectangular windows. The estimated probability density of a random variable \mathbf{y} can be expressed as

$$\hat{p}(\mathbf{y}) = \frac{1}{n} \sum_{i=1}^n K(u), \quad (2.2)$$

where

$$u = \frac{(\mathbf{y} - \mathbf{y}_i)^T S^{-1} (\mathbf{y} - \mathbf{y}_i)}{h^2}, \quad (2.3)$$

$K(u)$ is the kernel function, \mathbf{y} has dimensionality d , n is the sample size, \mathbf{y}_i is an observation of \mathbf{y} , h is the kernel bandwidth and S is the covariance matrix of \mathbf{y}_i . In practice, $K(u)$ is the multivariate Gaussian kernel:

$$K(u) = \frac{1}{(2\pi)^{d/2} h^d \det(S)^{1/2}} \exp(-u/2). \quad (2.4)$$

The value of h is given by

$$h = \left\{ \frac{4}{d+2} \right\}^{1/(d+4)} n^{-1/(d+4)}. \quad (2.5)$$

Another estimator of mutual information is based on estimating entropy from k -nearest neighbour distances [97]. This method offers the advantages of being data efficient and adaptive. For one-dimensional variable X , the distance-based entropy estimator is given by:

$$H(X) \approx \frac{1}{N-1} \sum_{i=1}^{N-1} \log(x_{i+1} - x_i) + \psi(1) - \psi(N), \quad (2.6)$$

where $x_{i+1} \geq x_i$, N is the sample size and $\psi(x)$ is the digamma function defined as $\psi(x) = \Gamma(x)^{-1} d\Gamma(x)/dx$. For X with higher dimensions, the

entropy estimator is:

$$\hat{H}(X) = -\psi(k) + \psi(N) + \log c_d + \frac{d}{N} \sum_{i=1}^N \log \epsilon(i), \quad (2.7)$$

where d is the dimension of X , $c_d = \pi^{d/2}/\Gamma(1 + d/2)/2^d$ for L2 norm and $\epsilon(i)$ is twice the distance between x_i and its k th nearest neighbour.

The Maximal Information Coefficient (MIC) proposed in [140] is an extension to the vanilla mutual information. It searches for a grid-like partitioning between two random variables that yields the maximal possible mutual information, which is then normalized to have a range between 0 and 1. A characteristic matrix corresponding to the partitioned boxes is constructed, where each entry of the matrix is the maximal normalized mutual information of the respective box. The MIC is defined as the maximum entry in the characteristic matrix. This approach claims to have the best equitability among various independence criteria. An equitable independence criterion assigns similar scores to equally noisy datasets, regardless of underlying functional types. However, this definition of equitability has been questioned to be satisfied only by trivial dependence measures [91]. To address this concern, a new MIC estimator was proposed and the interpretation of equitability is clarified [141, 142].

Mutual information estimation in machine learning applications often employs total correlation, a measure that generalizes mutual information for more than two random variables [166]. In [87], total correlation is estimated using a discriminator on the basis of the density-ratio trick [125], while [22] estimates it directly from the sample entropy without an auxiliary neural network.

Estimating mutual information from a finite sample is a challenging task, as noted by previous research [3]. One prominent example is the ICA algorithm that relies on minimizing mutual information [5], which has been surpassed in performance by various other algorithms [55]. Given these limitations, in our work documented in [172], we chose not to compare our approach with mutual information-based methods.

2.1.3 Integral Probability Metric

Integral probability metric is a metric between two probability distributions \mathbb{P} and \mathbb{Q} . [122, 150]. It is mathematically defined as:

$$\gamma[\mathbb{P}, \mathbb{Q}] := \sup_{f \in \mathcal{F}} (\mathbf{E}_x[f(x)] - \mathbf{E}_y[f(y)]), \quad (2.8)$$

where x and y are two random variables with probability distributions \mathbb{P} and \mathbb{Q} respectively, \mathcal{F} is a class of real-valued bounded measurable functions. If $\gamma[\mathbb{P}, \mathbb{Q}] = 0$, \mathbb{P} and \mathbb{Q} are identical probability distributions.

Different choices of \mathcal{F} lead to different independence criteria. In [33], the authors select $\mathcal{F} = \{f : f(x, y) := e^{i(\alpha^T x + \beta^T y)}, i = \sqrt{-1}, (\alpha, \beta) \in \mathbb{R}^{d_x} \times \mathbb{R}^{d_y}\}$, where α and β are parameters of the joint characteristic function of x and y . This approach leverages the fact that characteristic functions can be interpreted as the Fourier transform of probability density functions, and so there exists a bijection between characteristic functions and probability density functions. Independence between x and y is indicated by the equivalence between the joint characteristic function of x and y and the product of their marginal characteristic functions.

Another popular option for \mathcal{F} is the unit ball in an RKHS [54]. The integral probability metric in this context is known as the Maximum Mean Discrepancy (MMD). The Hilbert-Schmidt Independence Criterion (HSIC) is formulated as $\text{HSIC}(x, y) = \text{MMD}(p_{xy}, p_x p_y)$ [55], where p_{xy} denotes the joint probability density function of x and y , while p_x and p_y represent their respective marginal probability density functions. Motivated by the observation that the witness function f ought to be sparse in terms of extracting features between x and y , the Sobolev Independence Criterion extends HSIC by imposing gradient penalties to ensure sparsity and stability [121]. In our work documented in [172], we compare our approach with two RKHS-based methods from [148] and [81].

2.2 Artificial Neural Network

Artificial Intelligence (AI) aims to empower machines with human-like thinking power and intelligent capacity. Recently, Artificial Neural Networks (ANNs) have become the predominant tools for building AI systems owing to the advancement of GPU power and data availability. ANNs are inspired by the biological structure and mechanism of human brains, and consist of layers of connected neurons [48]. In contrast to traditional approaches, ANNs can learn a myriad of parameters in a data-driven manner and generalize them to unseen scenarios. It is well known that ANNs exhibit the universal approximation property [32]. When the search space for globally optimal solutions is high-dimensional or non-analytic, ANNs can obtain competitive solutions that may be difficult or impossible to obtain through traditional numerical methods. They have demonstrated impressive performance in tasks such as speech separation and enhancement [164, 179]. This section provides an overview of ANNs, including their commonly used structures and training algorithms. It serves as a foundation for understanding the role of ANNs in modern AI systems and their potential in signal enhancement. Additionally, this section explores relevant examples of ANNs in the context of signal enhancement. Specifically, in Chapter 6 of our work, we apply ResNet. Furthermore, Neural Ordinary Differential Equations, Multichannel Variational Autoencoder (MVAE), Multi-Resolution Convolutional Auto-Encoder (MRCAE), beta VAE, and FactorVAE exhibit promising potential for utilization in signal enhancement tasks such as source separation and disentanglement. Chapter 7 will provide a more detailed discussion of future endeavors concerning multi-channel speech separation and disentanglement.

2.2.1 Common Structures of ANNs

An artificial neuron is an elementary structure of ANNs [113]. It mimics a brain neuron by multiplying the inputs with learnable weights. The multi-

plied results are summed up. Often a bias term is summed as an additional term. The weighted sum is sent to an activation function to generate the output. This process can be expressed as

$$Y = f_{NN}\left(\sum_i u_i \cdot w_i + b\right), \quad (2.9)$$

where Y is the output, f_{NN} is the activation function, u_i is one element of the inputs and w_i is the corresponding learnable weight, b is the learnable bias term.

A perceptron is a specific type of artificial neuron that performs binary classification [143]. Its activation function, a Heavyside step function, yields an output of 1 for positive arguments and 0 otherwise. The simplest type of feedforward neural network is a single-layer perceptron, where inputs propagate forward without loops or cycles. However, it is limited to learning linearly separable patterns [146]. In contrast, a Multi-Layer Perceptron (MLP) is capable of solving nonlinear problems by having at least one hidden layer between the input and output layers. While the term MLP can strictly refer to multiple layers of perceptrons for binary classification tasks, in this thesis, we adopt the loosely defined MLP to refer to any multi-layer feedforward ANNs. An illustration of an MLP is demonstrated in Fig. 2.1.

If inputs propagate in a circular manner, Recurrent Neural Networks (RNNs) are utilized [144]. RNNs exhibit time-dependent characteristics and can process variable-length inputs. The temporal dynamics of RNNs make them suitable for processing time series data or inputs with arbitrary lengths [116]. A powerful variant of RNNs is called Long Short Term Memory (LSTM) networks [64]. It adds self-loops to memory cells with gate units. This makes LSTMs capable of extracting long-term dependencies and mitigates the vanishing gradient problem [64].

Convolutional Neural Networks (CNNs) have gained popularity for their ability to process spatial patterns in data, making them particularly suitable for computer vision tasks [103]. This is achieved through the use

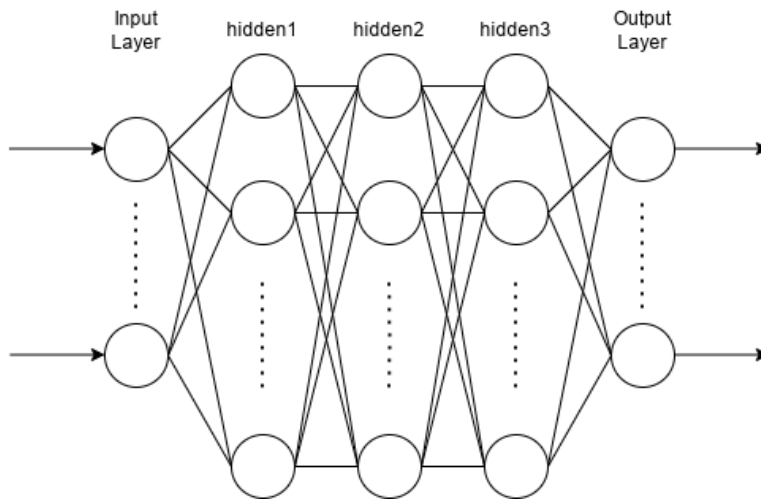


Figure 2.1: An illustration of an MLP with 3 hidden layers.

of convolutional kernels that are translation-equivariant. Each convolutional kernel functions as a learnable filter that convolves the input data by sliding along its dimensions. This approach allows for the parameters of the filter to be shared across different sliding locations, effectively reducing the number of parameters without compromising the performance of CNNs. The "convolution" operation in this context involves element-wise multiplication and addition. By utilizing multiple layers of convolutional kernels and pooling, features can be effectively extracted from low to high levels in the data.

Enumerating all the structures of ANNs would be an impossible mission due to the vast number of variations available. In addition to the structures discussed above, other commonly used ANN structures include Variational Autoencoders (VAEs) [90], Generative Adversarial Networks (GANs) [49], Diffusion networks [149], and many more. While these models are not directly related to the work presented in this thesis, interested readers are encouraged to refer to their original publications for further details.

2.2.2 ResNet

ResNets are a specific type of ANNs that excel in handling deep layers. Typically, deep neural networks can suffer from performance degradation. To address this issue, ResNets use shortcut connections between layers, which perform identity mapping and skip one or more layers. By establishing a direct path from the input to the output, gradients can flow from the last layer to the first layer without encountering any obstacles. This approach is motivated by the observation that deeper neural networks tend to have higher training error [153], indicating that they have difficulties approximating identity mappings. When identity mappings are near-optimal solutions, the explicitly added shortcut connections can simplify the learning tasks of deep neural networks.

Vanilla ResNets [59] allow shortcut connections to be applied to convolutional layers via element-wise addition between feature maps. When the dimensionality of the input and the output is not the same, a linear projection of the input through a 1×1 convolution is performed to match the dimensions. In addition, the authors of [59] propose the use of convolutional bottleneck blocks to increase computational efficiency. A bottleneck block comprises three layers: one 3×3 convolutional layer is sandwiched between two 1×1 convolutional layers.

2.2.3 Neural Ordinary Differential Equations

ResNet-like machine learning models [59] are structured as $\mathbf{h}_{t+1} = \mathbf{h}_t + f_\theta(\mathbf{h}_t)$, where \mathbf{h}_t and \mathbf{h}_{t+1} represent two consecutive hidden states, $t \in \mathbb{N}$ and f_θ denotes a neural network parameterized by θ . This structure can be viewed as a discrete approximation of the ordinary differential equation $\frac{d\mathbf{h}(t)}{dt} = f(\mathbf{h}(t))$.

Drawing inspiration from ResNet-like models, the pioneering work of [23] seamlessly integrated ordinary differential equations with neural networks. Neural Ordinary Differential Equations (Neural ODEs) are defined

as:

$$\mathbf{z}(t_1) = \mathbf{z}(t_0) + \int_{t_0}^{t_1} f_{\theta}(\mathbf{z}(t))dt, \quad (2.10)$$

where $\mathbf{z}(t_1)$ and $\mathbf{z}(t_0)$ are the final and initial hidden states, and t represents continuous time. Unlike the notation convention in [23], we find it more suitable to exclude t from the bracket of f_{θ} , as t is not actually involved in the computation of f_{θ} , but rather used only during the ODE solver’s integration process. It is worth noting that θ remains constant in vanilla Neural ODEs. In other words, θ does not change with respect to t . The invariance of θ with respect to t suggests that Neural ODEs can have a more efficient parameterization than conventional neural networks.

The continuous property of differential equations confers to Neural ODEs a greater degree of control than conventional neural networks [50]. Firstly, the number of outputs from Equation 2.10 is flexible and determined by the number of timestamps in t owing to the ODE solver. Because t can be arbitrary, the number of outputs can be altered without modifying the model architecture. Secondly, the outputs from Equation 2.10 can have varying degrees of resolution. As we have complete control over the resolution of timestamps in t , we also have complete control over the resolution of the outputs. We can access an output value at any desired timestamp. Lastly, by integrating backwards, we can obtain outputs prior to the initial states. This property of Neural ODEs allows us to ‘predict’ the past.

After θ has been learned, Neural ODEs are determined solely by the initial state, which means that they do not take full advantage of upcoming information. In contrast, Neural Controlled Differential Equations (Neural CDEs) can incorporate input data directly into the hidden dynamics by utilizing Riemann–Stieltjes integral [86]. Neural CDEs are defined by:

$$\mathbf{z}(t_1) = \mathbf{z}(t_0) + \int_{t_0}^{t_1} f_{\theta}(\mathbf{z}(t))dX_t, \quad (2.11)$$

where X can be a natural cubic spline that approximates the underlying process of input data.

2.2.4 Multichannel Variational Autoencoder (MVAE)

DNN based multi-channel audio source separation algorithms often estimate the source spectrograms with forward computations. They can take full advantage of the strong representation power of DNNs to model power spectra of source signals. The MVAE method proposed in [82] also guarantees the convergence of the source separation of the algorithm. It has a consistent objective for both VAE training and source separation.

The problem formulation of MVAE follows the line of determined BSS. It considers scenarios where the number of source signals and microphones are equal to I . Denote the Short Time Fourier Transform (STFT) coefficients of the signals of the i -th microphone and the j -th source signal as $x_i(f, n)$ and $s_j(f, n)$, where f and n are the frequency and time indices. Their vector forms are:

$$\mathbf{x}(f, n) = [x_1(f, n), \dots, x_I(f, n)]^T \in \mathbb{C}^I, \quad (2.12)$$

$$\mathbf{s}(f, n) = [s_1(f, n), \dots, s_I(f, n)]^T \in \mathbb{C}^I, \quad (2.13)$$

where $(\cdot)^T$ means transpose. A separation system can now be expressed as

$$\mathbf{s}(f, n) = \mathbf{W}^H(f)\mathbf{x}(f, n), \quad (2.14)$$

$$\mathbf{W}(f) = [\mathbf{w}_1(f), \dots, \mathbf{w}_I(f)], \quad (2.15)$$

where $\mathbf{W}^H(f)$ is the separation matrix and $(\cdot)^H$ is Hermitian transpose. The goal of BSS algorithms is to estimate the separation matrix merely from the observed $\mathbf{x}(f, n)$.

A Local Gaussian Model (LGM) is assumed for $s_j(f, n)$. It follows a zero-mean complex Gaussian distribution with variance $v_j(f, n) = \mathbf{E}[|s_j(f, n)|^2]$

$$s_j(f, n) \sim \mathcal{N}_{\mathbb{C}}(s_j(f, n)|0, v_j(f, n)). \quad (2.16)$$

Assume all source signals are independent, we have

$$\mathbf{s}(f, n) \sim \mathcal{N}_{\mathbb{C}}(\mathbf{s}(f, n)|\mathbf{0}, \mathbf{V}(f, n)), \quad (2.17)$$

where $\mathbf{V}(f, n)$ is a diagonal matrix with diagonal entries $v_1(f, n), \dots, v_I(f, n)$.

MVAE employs a Conditional VAE (CVAE) [89] as the neural network model. It takes an auxiliary variable c as an additional input. Define $\tilde{\mathbf{S}} = \{s(f, n)\}_{f,n}$ as the complex power spectra of a source signal and c as the class label. Define θ and ϕ as hyperparameters in the decoder and encoder. The objective function of MVAE is

$$\mathcal{J}(\phi, \theta) = \mathbf{E}_{(\tilde{\mathbf{s}}, c) \sim p_D(\tilde{\mathbf{s}}, c)} \left[\mathbf{E}_{\mathbf{z} \sim q(\mathbf{z}|\tilde{\mathbf{s}}, c)} [\log p(\tilde{\mathbf{S}}|\mathbf{z}, c)] - \text{KL}[q(\mathbf{z}|\tilde{\mathbf{S}}, c)||p(\mathbf{z})] \right], \quad (2.18)$$

where $\mathbf{E}_{(\tilde{\mathbf{s}}, c) \sim p_D(\tilde{\mathbf{s}}, c)}[\cdot]$ is the sample mean over the training data $\{\tilde{\mathbf{S}}_m, c_m\}_{m=1}^m$.

The MVAE model [82] is compared against a Independent Low-Rank Matrix Analysis [92] (ILRMA) model. The evaluation metrics are the signal-to-distortion ratio (SDR), signal-to-interference ratio (SIR) and signal-to-artifact ratio (SAR) [161]. The MVAE model significantly outperform the ILRMA model in these metrics.

It is noteworthy that the MVAE model does not perform well when there is long reverberation. This also suggests that there is a lot of room to improve before we can design a multi-channel audio source separation algorithm that is applicable in real life.

2.2.5 Multi-Resolution Convolutional Autoencoder (MR-CAE)

Unlike MVAE, the MRCAE model does not need spectrograms to perform multi-channel audio source separation [51]. To reconstruct time-domain signals from the spectrogram may not be a straightforward task. The neglect of phase information can often lead to poor perceptual quality of the reconstructed signals. MRCAE is an end-to-end model that takes raw time-domain signals as its input and automatically extracts suitable features.

MRCAE is a multi-resolution fully convolutional denoising auto-encoder neural network. The encoder part contains convolutional layers and the

decoder part consists of transpose convolutional layers [38]. This is because the encoder extracts multi-resolution acoustic features and the decoder estimates the original sources from these extracted features.

Each layer in MRCAE is composed of sets of filters. Filters in the same set have the same size. Filter size varies in different sets. Large filters capture global information, whereas small filters extract local information. Large filters are like calculating STFT over long windows, and small filters are like calculating STFT over short windows. Together in the same layer they produce features with different time-frequency resolutions.

The total number of filters in the output layer equals the number of target sources multiplied by the number of channels for each source. This guarantees that the output layer generates feature maps equal to the number of target sources, where each source has its multiple channel components.

Let $y(t, c)$ be the input signal for channel c and $s_l(t, c)$ be the target source l for channel c . Here t denotes time. The cost function for MRCAE is $D = \sum_{t,c,l} |z_l(t, c) - s_l(t, c)|$, where $z_l(t, c)$ is the actual output of the last layer of the MRCAE for source l and channel c . No pre-processing or post-processing is performed other than normalizing the input signals to have zero mean and unit variance. The experimental results show that MRCAE can do a promising job on multi-channel music source separation.

Since stereo-recorded music signals are not as complicated as real-life speech signals in reverberant and noisy environments, we need to investigate further to determine how much of the MRCAE technique can be transferred to multi-channel speech separation in a practical setting.

2.2.6 Beta VAE

β -VAE is a deep generative autoencoder model that can automatically discover disentangled representations in an unsupervised manner [62]. Its model is an augmentation of the original VAE framework [90]. Let x be

input signals and \mathbf{z} be generative latent factors. Let ϕ and θ be parameters defining the encoder and decoder part of the VAE framework. The Evidence Lower Bound (ELBO) is the maximization objective of the original VAE:

$$\mathcal{L}(\theta, \phi; \mathbf{x}, \mathbf{z}) = \mathbf{E}_{q_\phi(\mathbf{z}|\mathbf{x})}[\log p_\theta(\mathbf{x}|\mathbf{z})] - D_{KL}(q_\phi(\mathbf{z}|\mathbf{x})||p(\mathbf{z})), \quad (2.19)$$

where $q_\phi(\mathbf{z}|\mathbf{x})$ is the posterior distribution configured by the encoder, $p_\theta(\mathbf{x}|\mathbf{z})$ is the likelihood distribution configured by the decoder and $p(\mathbf{z})$ is the prior distribution of the latent factors. The expectation term in the ELBO can be intuitively considered as the reconstruction loss. It tries to make the decoded signals more correlated to the latent factors. The D_{KL} term denotes the Kullback–Leibler (KL) divergence between two distributions [100]. It can be interpreted as encouraging the posterior distribution to be close to the prior distribution.

β -VAE introduces a hyperparameter β to balance the independence constraints and the reconstruction accuracy. After applying KKT conditions [83, 99], the ELBO objective can be transformed into a Lagrangian and β plays the role of a Lagrange multiplier according to the complementary slackness KKT condition. The new objective function in β -VAE can be expressed as:

$$\mathcal{L}(\theta, \phi; \mathbf{x}, \mathbf{z}, \beta) = \mathbf{E}_{q_\phi(\mathbf{z}|\mathbf{x})}[\log p_\theta(\mathbf{x}|\mathbf{z})] - \beta D_{KL}(q_\phi(\mathbf{z}|\mathbf{x})||p(\mathbf{z})). \quad (2.20)$$

When $\beta = 1$, β -VAE becomes exactly the original VAE. The authors of β -VAE suggest that it is crucial to set $\beta > 1$ to put greater independence pressure on the learnt posterior. When the pressure is combined with maximizing the log likelihood of the input signal \mathbf{x} , the model is encouraged to learn the most efficient representation with a unit Gaussian prior. With the help of some ground truth factors as conditions, higher values of β leads to a disentangled representation in the latent space. However, a trade-off between reconstruction quality and disentanglement quality can occur. The right balance has to be controlled by β .

A new quantitative disentanglement metric is also proposed in β -VAE. By using some ground truth factors \mathbf{v} and labels $y \sim \text{Unif}[1\dots K]$, synthetic data can be simulated. A linear classifier with a low VC-dimension is trained to predict $p(y|\mathbf{z}_{\text{diff}})$, where \mathbf{z}_{diff} is the mean absolute pairwise difference between the averages of posterior distributions. The latent factors from posterior distributions are sampled by fixing one ground truth factor and vary other factors randomly. The index k of the fixed factor would correspond to the label y . A perfect disentanglement would yield zeros in the dimension of the fixed factor so that the linear classifier would match that dimension of zeros to the desired label y . The error rate of the classifier becomes the metric.

2.2.7 FactorVAE

One disadvantage of β -VAE is that it has to sacrifice reconstruction quality to achieve good disentanglement. To mitigate this issue, FactorVAE [87] augments the original VAE with a penalty term encouraging factorized distributions in the latent space. This penalty term is the KL divergence between the marginal posterior distribution $q_\phi(z)$ and the product of its underlying factors $q_\phi(z_j)$'s. The objective of FactorVAE can be thus expressed as:

$$\mathbf{E}_{q_\phi(\mathbf{z}|\mathbf{x})}[\log p_\theta(\mathbf{x}|\mathbf{z})] - D_{KL}(q_\phi(\mathbf{z}|\mathbf{x})||p(\mathbf{z})) - \gamma D_{KL}(q_\phi(z)||\bar{q}(z)), \quad (2.21)$$

where $\bar{q}(z) = \prod_{j=1}^d q_\phi(z_j)$. The new term $D_{KL}(q_\phi(z)||\bar{q}(z))$ is also known as Total Correlation (TC), which is a multi-variate dependence measurement [166]. By minimizing the TC between $q_\phi(z)$ and $\bar{q}(z)$, FactorVAE directly encourages independence in each dimension j of the latent distribution $q_\phi(z)$.

It may be observed that both $q_\phi(z)$ and $\bar{q}(z)$ are intractable as they consist of many component mixtures. An alternative is to sample $q_\phi(z)$ by sampling from $q_\phi(\mathbf{z}|\mathbf{x}^{(i)})$ with a randomly selected data batch $\mathbf{x}^{(i)}$. To sample $\bar{q}(z)$, we can first sample a batch from $q_\phi(z)$ and then perform an inde-

pendent random permutation across the batch in each dimension. This is a standard trick to make all dimensions independent [2].

The calculation of the TC term requires the density-ratio trick [125]. A discriminator D is trained to approximate the density ratio in the TC term. The output $D(z)$ of D is the probability that the input is from $q_\phi(z)$ rather than from $\bar{q}(z)$. We have the calculation as follows:

$$\begin{aligned}
 TC(z) &= D_{KL}(q_\phi(z) || \bar{q}(z)) \\
 &= \mathbf{E}_{q_\phi(z)} \left[\log \frac{q_\phi(z)}{\bar{q}(z)} \right] \\
 &\approx \mathbf{E}_{q_\phi(z)} \left[\log \frac{D(z)}{1 - D(z)} \right]. \tag{2.22}
 \end{aligned}$$

A new disentanglement metric is proposed in FactorVAE, which is the error rate of a majority-vote classifier. The data for the classifier is constructed as follows. Firstly, fixing one ground truth factor k . Latent representations are generated by varying other factors randomly. Take the empirical variance of the normalized latent representations in each dimension. The dimension with the lowest variance should correspond to the fixed factor k . For perfectly disentangled representations, the lowest variance should be 0. In the end, the classifier is used to predict the target fixed factor from given variances by selecting the dimension with the minimum variance. The classifier necessitates no hyperparameters and it does not have a failure mode.

2.2.8 Training of ANNs

ANNs are trained by adjusting the learnable weights of neurons. The training process is categorized into three major paradigms: supervised, unsupervised, and reinforcement learning. In supervised learning, ANNs are iteratively trained to minimize the loss function, which measures the discrepancy between predicted outputs and their corresponding labeled

outputs. On the other hand, unsupervised learning trains ANNs without any labeled data, by using a loss function that guides the network to discover the underlying structure in the input data. Reinforcement learning trains ANNs to learn how to take actions in an environment that maximizes the reward, by adjusting the weights of the network based on the feedback signals received from the environment. These three categories of training paradigms provide a comprehensive framework for training ANNs to perform a wide range of tasks in various domains.

In all three major training paradigms of ANNs, the most commonly used training algorithm is backpropagation, first introduced by Rumelhart et al. in 1986 [144]. Backpropagation consists of two phases: the forward phase and the backward phase. During the forward phase, input data is propagated through the ANNs to generate outputs, which are then evaluated according to the loss function. In the backward phase, the gradients of the loss function with respect to the learnable weights of the ANNs are computed. By utilizing the chain rule of differentiation, the error is propagated from the last layer to the first layer. To adjust the learnable weights, Stochastic Gradient Descent (SGD) [144] is often utilized. However, variants of SGD such as Adam [88] and RMSprop [53] are also commonly utilized to circumvent the problem of local optima and speed up the convergence rate. These optimization algorithms have been shown to be highly effective in training ANNs for a wide range of applications.

While other training algorithms of ANNs, such as those taking advantage of the information bottleneck principle [109] or the forward gradients [138] to become more biologically plausible, also exist, they are outside the scope of this thesis.

Regularization techniques are essential in the training of ANNs to prevent overfitting, where ANNs may fit noise rather than underlying data patterns. These techniques are generally applied by reducing the number of parameters or imposing constraints on the parameters. For example, dropout [152] randomly drops some of the neurons in ANNs during

training, forcing the remaining neurons to be more robust and representative. In each iteration of training, a different subset of neurons is dropped, which effectively alleviates overfitting. Another example of regularization is L2 regularization [98], which adds a penalty term proportional to the L2-norm of the learnable weights in the loss function. By encouraging weights with smaller L2 norms, overfitting is less likely to happen. Different regularization techniques can be combined to accommodate specific ANNs.

2.3 Microphone Array Fixed Beamforming

Beamforming is a spatial filtering technique commonly used in sensor arrays [160]. As the name suggests, beamforming forms a main beam in the target direction to enhance signals of interest while attenuating interfering and noisy signals from other directions. Beamforming has a wide range of applications in fields such as radar, sonar, and speech processing [10]. By selectively focusing on the desired signal source, beamforming can improve the signal-to-noise ratio and enhance the overall signal quality. With its versatility and effectiveness, beamforming continues to be an active area of research and development in various fields.

Fixed beamforming is a type of beamforming that utilizes spatial filters that are fixed and independent of the input data, making no assumption of the source and noise signals [8]. Fixed beamformers are not affected by changes in the acoustic environment around them, making them a popular choice in speech processing applications when the environment is stationary. Combined with microphone arrays, fixed beamformers can enhance the desired speech signals while suppressing interfering noise and reverberation. This section provides an overview of different fixed beamforming techniques, including delay-and-sum, maximum directivity, and differential beamforming. Each of these techniques has its own strengths and weaknesses, and the choice of technique depends on the specific applica-

tion and the desired performance criteria. By gaining an understanding of the advantages and limitations associated with these fixed beamforming techniques, readers will be better equipped to comprehend our work in Chapters four to six.

2.3.1 Notations

The examples illustrated in this section are based on uniform linear arrays unless specified otherwise. Let δ be the distance between two adjacent microphones. θ_d denotes the angle between the source signal and the array. The steering vector is defined as

$$\mathbf{d}(f, \cos \theta_d) = [1, e^{-j2\pi f\tau_0 \cos \theta_d}, \dots, e^{-j(M-1)2\pi f\tau_0 \cos \theta_d}], \quad (2.23)$$

where $j = \sqrt{-1}$ is the imaginary unit, f is the temporal frequency, c is the speed of sound in the air, $\tau_0 = \delta/c$ is the delay between two successive microphones at angle 0.

$\mathbf{h}(f)$ denotes the complex beamforming weight vector. We can further define the White Noise Gain (WNG), which measures the robustness of a microphone array:

$$\mathcal{W}[\mathbf{h}(f)] = \frac{|\mathbf{h}^H(f)\mathbf{d}(f, \cos \theta_d)|^2}{\mathbf{h}^H(f)\mathbf{h}(f)}. \quad (2.24)$$

Directivity Factor (DF) is a metric measuring the directional enhancement capacity of a microphone array, which is defined as:

$$\mathcal{D}[\mathbf{h}(f)] = \frac{|\mathbf{h}^H(f)\mathbf{d}(f, \cos \theta_d)|^2}{\mathbf{h}^H(f)\Gamma_{0,\pi}(f)\mathbf{h}(f)}, \quad (2.25)$$

where $\Gamma_{0,\pi}(f) = \frac{1}{2} \int_0^\pi \mathbf{d}(f, \cos \theta_d)\mathbf{d}^H(f, \cos \theta_d) \sin \theta d\theta$, $[\Gamma_{0,\pi}(f)]_{ij} = \text{sinc}[2\pi f(j-i)\tau_0]$ and $[\Gamma_{0,\pi}(f)]_{mm} = 1$, $m = 1, 2, \dots, M$ where there are M microphones in the array.

The theoretical maximum WNG can be derived. By using the Cauchy-Schwarz inequality, we obtain

$$|\mathbf{h}^H(f)\mathbf{d}(f, \theta_d)|^2 \leq \mathbf{h}^H(f)\mathbf{h}(f) \times \mathbf{d}^H(f, \theta_d)\mathbf{d}(f, \theta_d) = M\mathbf{h}^H(f)\mathbf{h}(f). \quad (2.26)$$

This means that $\mathcal{W}_{\max}(f, \cos \theta_d) = M$.

The theoretical maximum DF can also be derived by using the Cauchy-Schwarz inequality, and is

$$\begin{aligned}
& |\mathbf{h}^H(f) \mathbf{d}(f, \cos \theta_d)|^2 \\
&= |\mathbf{h}^H(f) \Gamma_{0,\pi}^{1/2}(f) \Gamma_{0,\pi}^{-1/2}(f) \mathbf{d}(f, \cos \theta_d)|^2 \\
&\leq \mathbf{h}^H(f) \Gamma_{0,\pi}^{1/2}(f) \Gamma_{0,\pi}^{1/2}(f) \mathbf{h}(f) \times \mathbf{d}^H(f, \cos \theta_d) \Gamma_{0,\pi}^{-1/2}(f) \Gamma_{0,\pi}^{-1/2}(f) \mathbf{d}(f, \cos \theta_d) \\
&= \mathbf{h}^H(f) \Gamma_{0,\pi}(f) \mathbf{h}(f) \times \mathbf{d}^H(f, \cos \theta_d) \Gamma_{0,\pi}^{-1}(f) \mathbf{d}(f, \cos \theta_d). \tag{2.27}
\end{aligned}$$

This suggests

$$\mathcal{D}_{\max}(f, \cos \theta_d) = \mathbf{d}^H(f, \cos \theta_d) \Gamma_{0,\pi}^{-1}(f) \mathbf{d}(f, \cos \theta_d) \tag{2.28}$$

$$= \text{tr}[\Gamma_{0,\pi}^{-1}(f) \mathbf{d}(f, \cos \theta_d) \mathbf{d}^H(f, \cos \theta_d)] \tag{2.29}$$

$$\leq M \text{tr}[\Gamma_{0,\pi}^{-1}(f)]. \tag{2.30}$$

2.3.2 Delay-and-Sum

The Delay-and-Sum (DS) beamformer is the most popular fixed beamformer [10]. It delays the output from each microphone by a proper amount of time to achieve signal synchronization from the desired look direction. The delayed outputs are weighted and summed to generate the final output. Mathematically, the DS beamformer is derived by maximizing WNG:

$$\begin{aligned}
& \min_{\mathbf{h}(f)} \mathbf{h}^H(f) \mathbf{h}(f) \\
& \text{s.t. } \mathbf{h}^H(f) \mathbf{d}(f, \cos \theta_d) = 1. \tag{2.31}
\end{aligned}$$

Thus, the optimal filter \mathbf{h}_{DS} for the DS beamformer can be obtained:

$$\begin{aligned}
\mathbf{h}_{DS}(f, \cos \theta_d) &= \frac{\mathbf{d}(f, \cos \theta_d)}{\mathbf{d}^H(f, \cos \theta_d) \mathbf{d}(f, \cos \theta_d)} \\
&= \frac{\mathbf{d}(f, \cos \theta_d)}{M}. \tag{2.32}
\end{aligned}$$

We can calculate the cosine of the angle between the steering vector and the optimal WNG filter:

$$\begin{aligned}
\cos[\mathbf{d}(f, \cos \theta_d), \mathbf{h}_{DS}(f)] &= \frac{\mathbf{d}^H(f, \cos \theta_d) \mathbf{h}_{DS}(f) + \mathbf{h}_{DS}^H(f) \mathbf{d}(f, \cos \theta_d)}{2 \|\mathbf{d}(f, \cos \theta_d)\|_2 \|\mathbf{h}_{DS}(f)\|_2} \\
&= \frac{1 + 1}{2\sqrt{M} \sqrt{\frac{1}{M}}} \\
&= 1.
\end{aligned} \tag{2.33}$$

The DF value of the DS beamformer can be analytically obtained by using $\mathcal{D}_{\max}(f, \cos \theta_d)$:

$$\begin{aligned}
&\mathcal{D}[\mathbf{h}_{DS}(f, \cos \theta_d)] \\
&= \mathcal{D}_{\max}(f, \cos \theta_d) \times \cos^2[\Gamma_{0,\pi}^{1/2}(f) \mathbf{d}(f, \cos \theta_d), \Gamma_{0,\pi}^{-1/2}(f) \mathbf{d}(f, \cos \theta_d)] \\
&= \mathcal{D}_{\max}(f, \cos \theta_d) \times \frac{(\mathbf{d}^H(f, \cos \theta_d) \mathbf{d}(f, \cos \theta_d))^2}{\mathbf{d}^H(f, \cos \theta_d) \Gamma_{0,\pi}(f) \mathbf{d}(f, \cos \theta_d) \mathbf{d}^H(f, \cos \theta_d) \Gamma_{0,\pi}^{-1}(f) \mathbf{d}(f, \cos \theta_d)} \\
&= \mathbf{d}^H(f, \cos \theta_d) \Gamma_{0,\pi}^{-1}(f) \mathbf{d}(f, \cos \theta_d) \times \frac{M^2}{\mathbf{d}^H(f, \cos \theta_d) \Gamma_{0,\pi}(f) \mathbf{d}(f, \cos \theta_d) \mathbf{d}^H(f, \cos \theta_d) \Gamma_{0,\pi}^{-1}(f) \mathbf{d}(f, \cos \theta_d)} \\
&= \frac{M^2}{\mathbf{d}^H(f, \cos \theta_d) \Gamma_{0,\pi}(f) \mathbf{d}(f, \cos \theta_d)}.
\end{aligned} \tag{2.34}$$

The value of $\cos^2[\Gamma_{0,\pi}^{1/2}(f)\mathbf{d}(f, \cos \theta_d), \Gamma_{0,\pi}^{-1/2}(f)\mathbf{d}(f, \cos \theta_d)]$ has a lower bound:

$$\begin{aligned}
& \cos^2[\Gamma_{0,\pi}^{1/2}(f)\mathbf{d}(f, \cos \theta_d), \Gamma_{0,\pi}^{-1/2}(f)\mathbf{d}(f, \cos \theta_d)] \\
&= \frac{(\mathbf{d}^H(f, \cos \theta_d)\mathbf{d}(f, \cos \theta_d))^2}{\mathbf{d}^H(f, \cos \theta_d)\Gamma_{0,\pi}(f)\mathbf{d}(f, \cos \theta_d)\mathbf{d}^H(f, \cos \theta_d)\Gamma_{0,\pi}^{-1}(f)\mathbf{d}(f, \cos \theta_d)} \\
&= \frac{M^2}{\text{tr}[\Gamma_{0,\pi}(f)\mathbf{d}(f, \cos \theta_d)\mathbf{d}^H(f, \cos \theta_d)]\text{tr}[\Gamma_{0,\pi}^{-1}(f)\mathbf{d}(f, \cos \theta_d)\mathbf{d}^H(f, \cos \theta_d)]} \\
&\geq \frac{M^2}{\lambda_1(\Gamma_{0,\pi}(f))\text{tr}[\mathbf{d}(f, \cos \theta_d)\mathbf{d}^H(f, \cos \theta_d)]\lambda_1(\Gamma_{0,\pi}^{-1}(f))\text{tr}[\mathbf{d}(f, \cos \theta_d)\mathbf{d}^H(f, \cos \theta_d)]} \\
&= \frac{M^2}{\lambda_1(\Gamma_{0,\pi}(f)) \cdot M \cdot \lambda_1(\Gamma_{0,\pi}^{-1}(f)) \cdot M} \\
&= \frac{1}{\lambda_1(\Gamma_{0,\pi}(f))\frac{1}{\lambda_M(\Gamma_{0,\pi}(f))}} \\
&= \frac{\lambda_M(\Gamma_{0,\pi}(f))}{\lambda_1(\Gamma_{0,\pi}(f))}, \tag{2.35}
\end{aligned}$$

where $\lambda_1(\Gamma_{0,\pi}(f))$ and $\lambda_M(\Gamma_{0,\pi}(f))$ are the largest and smallest eigenvalue of $\Gamma_{0,\pi}(f)$. The beampattern of this DS beamformer is

$$\begin{aligned}
& |\mathcal{B}[\mathbf{h}_{DS}(f, \cos \theta_d), \cos \theta]|^2 \\
&= \frac{1}{M^2} |\mathbf{d}^H(f, \cos \theta)\mathbf{d}(f, \cos \theta_d)|^2 \\
&= \frac{1}{M^2} (\|\mathbf{d}(f, \cos \theta)\|_2^2 \|\mathbf{d}(f, \cos \theta_d)\|_2^2 \cos^2[\mathbf{d}(f, \cos \theta), \mathbf{d}(f, \cos \theta_d)]) \\
&= \cos^2[\mathbf{d}(f, \cos \theta), \mathbf{d}(f, \cos \theta_d)]. \tag{2.36}
\end{aligned}$$

The Kantorovich inequality implies that if A is an $n \times n$ positive definite matrix, then the cosine of the angle θ between $n \times 1$ real vectors x and Ax has a minimum value. Let λ_1 and λ_n be the smallest and largest eigenvalue of A , the minimum value of $\cos \theta$ is $\frac{2\sqrt{\lambda_1\lambda_n}}{\lambda_1+\lambda_n}$. In the DS beamformer, we can set $x = \Gamma_{0,\pi}^{-1/2}(f)\mathbf{d}(f, \cos \theta_d)$ and $A = \Gamma_{0,\pi}(f)$.

DS beamformers have two major drawbacks that limit their effectiveness. Firstly, their beampattern is not frequency-invariant and the beamwidth is inversely proportional to the frequency. This leads to non-uniform attenuation of noise, resulting in disturbing artifacts in the output signal.

Secondly, the directivity factors of DS beamformers are low at low frequencies, making them less effective in suppressing noise and interference at these frequencies. These limitations can significantly impact the quality of the output signal, especially in environments with significant low-frequency noise and interference. Thus, while DS beamformers are a simple and widely-used fixed beamforming technique, they may not be suitable for all applications, and alternative techniques should be considered for improved performance in challenging environments.

2.3.3 Maximum Directivity Factor

In contrast to the DS beamformer, we can derive fixed beamformers that maximize directivity factor with the formulation:

$$\begin{aligned} \min_{\mathbf{h}(f)} \quad & \mathbf{h}^H(f)\Gamma_{0,\pi}(f)\mathbf{h}(f) \\ \text{s.t.} \quad & \mathbf{h}^H(f)\mathbf{d}(f, \cos \theta) = 1. \end{aligned} \quad (2.37)$$

The Lagrangian of Equation 2.37 is

$$\mathcal{L}(\mathbf{h}(f), \nu) = \mathbf{h}^H(f)\Gamma_{0,\pi}(f)\mathbf{h}(f) + \nu(\mathbf{h}^H(f)\mathbf{d}(f, \cos \theta) - 1). \quad (2.38)$$

The derivative of this Lagrangian regarding $\mathbf{h}(f)$ is

$$\nabla_{\mathbf{h}(f)}\mathcal{L}(\mathbf{h}(f), \nu) = 2\Gamma_{0,\pi}(f)\mathbf{h}(f) + \nu\mathbf{d}(f, \cos \theta). \quad (2.39)$$

Set this to 0, we get

$$\mathbf{h}(f) = -\frac{1}{2}\nu\Gamma_{0,\pi}^{-1}(f)\mathbf{d}(f, \cos \theta). \quad (2.40)$$

Substituting (2.40) into (2.38), we get the Lagrange dual

$$g(\nu) = \inf_{\mathbf{h}(f)} \mathcal{L}(\mathbf{h}(f), \nu) = -\frac{1}{4}\nu^2\mathbf{d}^H(f, \cos \theta)\Gamma_{0,\pi}^{-1}(f)\mathbf{d}(f, \cos \theta) - \nu. \quad (2.41)$$

The maximum of $g(\nu)$ is achieved when

$$\nu = \frac{-2}{\mathbf{d}^H(f, \cos \theta)\Gamma_{0,\pi}^{-1}(f)\mathbf{d}(f, \cos \theta)}. \quad (2.42)$$

Substituting (2.42) back to (2.40), we get

$$\mathbf{h}_{\text{mDF}}(f) = \frac{\Gamma_{0,\pi}^{-1}(f)\mathbf{d}(f, \cos \theta)}{\mathbf{d}^H(f, \cos \theta)\Gamma_{0,\pi}^{-1}(f)\mathbf{d}(f, \cos \theta)}. \quad (2.43)$$

To make maximum DF beamforming more robust, we can maximize DF with a constraint on WNG [10]. This translates to the problem

$$\begin{aligned} \min_{\mathbf{h}(f)} \quad & \mathbf{h}^H(f)[\Gamma_{0,\pi}(f) + \epsilon I_M]\mathbf{h}(f) \\ \text{s.t.} \quad & \mathbf{h}^H(f)\mathbf{d}(f, \cos \theta) = 1. \end{aligned} \quad (2.44)$$

Solving this problem is similar to solving (2.37). We have

$$\mathbf{h}^*(f) = \frac{[\Gamma_{0,\pi}^{-1}(f) + \epsilon I_M]\mathbf{d}(f, \cos \theta)}{\mathbf{d}^H(f, \cos \theta)[\Gamma_{0,\pi}^{-1}(f) + \epsilon I_M]\mathbf{d}(f, \cos \theta)}. \quad (2.45)$$

We can rewrite (2.45) as

$$\mathbf{h}_{\text{R},\alpha}(f) = \frac{\Gamma_{\alpha}^{-1}(f)\mathbf{d}(f, \cos \theta)}{\mathbf{d}^H(f, \cos \theta)\Gamma_{\alpha}^{-1}(f)\mathbf{d}(f, \cos \theta)}, \quad (2.46)$$

where

$$\Gamma_{\alpha}(f) = [1 - \alpha(f)]\Gamma_{0,\pi}(f) + \alpha(f)I_M, \quad (2.47)$$

with $\alpha(f)$ being a real number and $0 \leq \alpha(f) \leq 1$. The inverse approximation [133] is

$$(A + \epsilon B)^{-1} \approx A^{-1} - \epsilon A^{-1}BA^{-1}, \quad (2.48)$$

where ϵ is small compared to A and B . Applying (2.48) to (2.47), we get

$$\begin{aligned} \Gamma_{\alpha}^{-1}(f) & \approx [(1 - \alpha(f))\Gamma_{0,\pi}(f)]^{-1} - \epsilon[(1 - \alpha(f))\Gamma_{0,\pi}(f)]^{-1}I_M[(1 - \alpha(f))\Gamma_{0,\pi}(f)]^{-1} \\ & = (1 - \alpha(f))^{-2}\Gamma_{0,\pi}^{-1}(f)[(1 - \alpha(f))\Gamma_{0,\pi}(f) - \alpha(f)I_M]\Gamma_{0,\pi}^{-1}(f) \\ & = (1 - \alpha(f))^{-2}\Gamma_{0,\pi}^{-1}(f)\Gamma_{\alpha}^{-1}(f)\Gamma_{0,\pi}^{-1}(f), \end{aligned} \quad (2.49)$$

for $0 \leq \alpha(f) \leq 0.5$, and

$$\begin{aligned}
\Gamma_{\alpha}^{-1}(f) &\approx (\alpha(f)I_M)^{-1} - (1 - \alpha(f))(\alpha(f)I_M)^{-1}\Gamma_{0,\pi}(f)(\alpha(f)I_M)^{-1} \\
&= -\alpha(f)^{-2}[(1 - \alpha(f))\Gamma_{0,\pi}(f) - \alpha(f)I_M] \\
&= -\alpha(f)^{-2}\Gamma_{\alpha^-}(f),
\end{aligned} \tag{2.50}$$

for $0.5 < \alpha(f) \leq 1$, where

$$\Gamma_{\alpha^-}(f) = (1 - \alpha(f))\Gamma_{0,\pi}(f) - \alpha(f)I_M. \tag{2.51}$$

The superdirective beamformer is a special case of the maximum DF beamformer where the look direction is $\theta_d = 0$. The spatial filter for the superdirective beamformer is:

$$\mathbf{h}_{\text{SD}}(f) = \frac{\Gamma_{0,\pi}^{-1}(f)\mathbf{d}(f, \cos \theta_d)}{\mathbf{d}^H(f, \cos \theta_d)\Gamma_{0,\pi}^{-1}(f)\mathbf{d}(f, \cos \theta)}. \tag{2.52}$$

The WNG of a superdirective (SD) beamformer can be expressed as

$$\mathcal{W}[\mathbf{h}_{\text{SD}}(f, \cos \theta_d)] = \mathcal{W}_{\max} \cos^2[\mathbf{d}(f, \cos \theta_d), \Gamma_{0,\pi}^{-1}(f)\mathbf{d}(f, \cos \theta_d)], \tag{2.53}$$

where

$$\begin{aligned}
&\cos^2[\mathbf{d}(f, \cos \theta_d), \Gamma_{0,\pi}^{-1}(f)\mathbf{d}(f, \cos \theta_d)] \\
&= \frac{\mathbf{d}^H(f, \cos \theta_d)\Gamma_{0,\pi}^{-1}(f)\mathbf{d}(f, \cos \theta_d)\mathbf{d}^H(f, \cos \theta_d)\Gamma_{0,\pi}^{-1}(f)\mathbf{d}(f, \cos \theta_d)}{\mathbf{d}^H(f, \cos \theta_d)\mathbf{d}(f, \cos \theta_d)\mathbf{d}^H(f, \cos \theta_d)\Gamma_{0,\pi}^{-2}(f)\mathbf{d}(f, \cos \theta_d)} = T.
\end{aligned} \tag{2.54}$$

One upper bound of $\cos^2[\mathbf{d}(f, \cos \theta_d), \Gamma_{0,\pi}^{-1}(f)\mathbf{d}(f, \cos \theta_d)]$ can be calculated

as

$$T = \frac{\text{tr}[\Gamma_{0,\pi}^{-1}(f)\mathbf{d}(f, \cos \theta_d)\mathbf{d}^H(f, \cos \theta_d)]\text{tr}[\Gamma_{0,\pi}^{-1}(f)\mathbf{d}(f, \cos \theta_d)\mathbf{d}^H(f, \cos \theta_d)]}{M\text{tr}[\Gamma_{0,\pi}^{-2}(f)\mathbf{d}(f, \cos \theta_d)\mathbf{d}^H(f, \cos \theta_d)]} \quad (2.55)$$

$$\leq \frac{\text{tr}[\Gamma_{0,\pi}^{-1}(f)]M\text{tr}[\Gamma_{0,\pi}^{-1}(f)]M}{M\text{tr}[\Gamma_{0,\pi}^{-2}(f)\mathbf{d}(f, \cos \theta_d)\mathbf{d}^H(f, \cos \theta_d)]} \quad (2.56)$$

$$= \frac{M[\text{tr}[\Gamma_{0,\pi}^{-1}(f)]]^2}{\text{tr}[\Gamma_{0,\pi}^{-2}(f)\mathbf{d}(f, \cos \theta_d)\mathbf{d}^H(f, \cos \theta_d)]} \quad (2.57)$$

$$\leq \frac{M[\text{tr}[\Gamma_{0,\pi}^{-1}(f)]]^2}{\lambda_M[\Gamma_{0,\pi}^{-2}(f)]\text{tr}[\mathbf{d}(f, \cos \theta_d)\mathbf{d}^H(f, \cos \theta_d)]} \quad (2.58)$$

$$= \frac{[\text{tr}[\Gamma_{0,\pi}^{-1}(f)]]^2}{\lambda_M[\Gamma_{0,\pi}^{-2}(f)]} \quad (2.59)$$

$$= \frac{[\text{tr}[\Gamma_{0,\pi}^{-1}(f)]]^2}{[\lambda_M[\Gamma_{0,\pi}^{-1}(f)]]^2}, \quad (2.60)$$

Alternatively, another upper bound can be derived from (2.55).

$$T \leq \frac{\lambda_1[\Gamma_{0,\pi}^{-1}(f)]M\lambda_1[\Gamma_{0,\pi}^{-1}(f)]M}{M\text{tr}[\Gamma_{0,\pi}^{-2}(f)\mathbf{d}(f, \cos \theta_d)\mathbf{d}^H(f, \cos \theta_d)]} \quad (2.61)$$

$$= \frac{[\lambda_1[\Gamma_{0,\pi}^{-1}(f)]]^2}{[\lambda_M[\Gamma_{0,\pi}^{-1}(f)]]^2}. \quad (2.62)$$

Similarly, a lower bound can also be derived from (2.55).

$$T \geq \frac{\lambda_M[\Gamma_{0,\pi}^{-1}(f)]M\lambda_M[\Gamma_{0,\pi}^{-1}(f)]M}{M\text{tr}[\Gamma_{0,\pi}^{-2}(f)\mathbf{d}(f, \cos \theta_d)\mathbf{d}^H(f, \cos \theta_d)]} \quad (2.63)$$

$$\geq \frac{M[\lambda_M[\Gamma_{0,\pi}^{-1}(f)]]^2}{[\lambda_1[\Gamma_{0,\pi}^{-1}(f)]]^2\text{tr}[\mathbf{d}(f, \cos \theta_d)\mathbf{d}^H(f, \cos \theta_d)]} \quad (2.64)$$

$$= \frac{[\lambda_M[\Gamma_{0,\pi}^{-1}(f)]]^2}{[\lambda_1[\Gamma_{0,\pi}^{-1}(f)]]^2}. \quad (2.65)$$

2.3.4 Differential Beamforming

Differential beamforming is a fixed beamforming technique that uses differential microphone arrays with small spacing between successive micro-

phones to measure the differential acoustic pressure field of different orders. This approach has become increasingly popular in fixed beamforming because it can form frequency-invariant beam patterns and achieve large directional gains with small apertures. In practice, the n th-order acoustic pressure differential can be approximated by a polynomial of degree n . Define $\omega = 2\pi f$. The beampattern of an N th-order DMA at angle θ is:

$$\mathcal{B}[\mathbf{h}(\omega), \theta] = \sum_{m=1}^M H_m(\omega) e^{j(m-1)\omega\tau_0 \cos \theta} \quad (2.66)$$

$$\approx \sum_{m=1}^M H_m(\omega) \sum_{n=0}^N \frac{1}{n!} [j(m-1)\omega\tau_0 \cos \theta]^n \quad (2.67)$$

$$\approx \sum_{n=0}^N \cos^n \theta \left[\frac{(j\omega\tau_0)^n}{n!} \sum_{m=1}^M (m-1)^n H_m(\omega) \right] \quad (2.68)$$

$$\approx \sum_{n=0}^N a_{N,n} \cos^n \theta = \mathcal{B}_N(\theta), \quad (2.69)$$

where $H_m(\omega)$ represents the complex weight of the m th microphone, $a_{N,n}$ is the coefficient of $\cos^n \theta$.

The differential beamforming filters approximated by series expansion can suffer from deep null problems [71]. To mitigate this issue, an alternative approach for constructing Differential Microphone Arrays (DMAs) is by using null-constraints [10]. In the simplest case, a linear array with two microphones are employed to construct a first-order DMA [10]. The two constraints are

$$d^H(f, 1)h(f) = 1 \quad (2.70)$$

$$d^H(f, \alpha_{1,1})h(f) = 0, \quad (2.71)$$

where $\alpha_{1,1} = \cos \theta_{1,1}$ is given by design (a null at the angle $\theta_{1,1}$) with $-1 \leq \alpha_{1,1} \leq 1$. Equations (2.70) and (2.71) can be rewritten as

$$\begin{bmatrix} 1 & e^{j2\pi f\tau_0} \\ 1 & e^{j2\pi f\tau_0\alpha_{1,1}} \end{bmatrix} h(f) = \begin{bmatrix} 1 \\ 0 \end{bmatrix}. \quad (2.72)$$

By solving this equation, we can get

$$h(f) = \begin{bmatrix} 1 & e^{j2\pi f\tau_0} \\ 1 & e^{j2\pi f\tau_0\alpha_{1,1}} \end{bmatrix}^{-1} \begin{bmatrix} 1 \\ 0 \end{bmatrix} \quad (2.73)$$

$$= \frac{1}{e^{j2\pi f\tau_0\alpha_{1,1}} - e^{j2\pi f\tau_0}} \begin{bmatrix} e^{j2\pi f\tau_0\alpha_{1,1}} & -e^{j2\pi f\tau_0} \\ -1 & 1 \end{bmatrix} \begin{bmatrix} 1 \\ 0 \end{bmatrix} \quad (2.74)$$

$$= \frac{1}{e^{j2\pi f\tau_0\alpha_{1,1}} - e^{j2\pi f\tau_0}} \begin{bmatrix} e^{j2\pi f\tau_0\alpha_{1,1}} \\ -1 \end{bmatrix} \quad (2.75)$$

$$= \frac{e^{-j2\pi f\tau_0\alpha_{1,1}}}{1 - e^{j2\pi f\tau_0(1-\alpha_{1,1})}} \begin{bmatrix} e^{j2\pi f\tau_0\alpha_{1,1}} \\ -1 \end{bmatrix} \quad (2.76)$$

$$= \frac{1}{1 - e^{j2\pi f\tau_0(1-\alpha_{1,1})}} \begin{bmatrix} 1 \\ -e^{-j2\pi f\tau_0\alpha_{1,1}} \end{bmatrix} \quad (2.77)$$

The WNG value is

$$\mathcal{W}[h(f)] = \frac{1}{h(f)^H h(f)} \quad (2.78)$$

$$= \frac{1}{2} |1 - e^{j2\pi f\tau_0(1-\alpha_{1,1})}|^2 \quad (2.79)$$

$$= \frac{1}{2} |1 - \cos(2\pi f\tau_0(1 - \alpha_{1,1})) - j \sin(2\pi f\tau_0(1 - \alpha_{1,1}))|^2 \quad (2.80)$$

$$= \frac{1}{2} [(1 - \cos(2\pi f\tau_0(1 - \alpha_{1,1})))^2 + \sin^2(2\pi f\tau_0(1 - \alpha_{1,1}))] \quad (2.81)$$

$$= \frac{1}{2} [2 - 2 \cos(2\pi f\tau_0(1 - \alpha_{1,1}))] \quad (2.82)$$

$$= 1 - \cos(2\pi f\tau_0(1 - \alpha_{1,1})). \quad (2.83)$$

Since $-1 \leq \alpha_{1,1} \leq 1$, we can observe that the maximum WNG is achieved

when $\alpha_{1,1}$ is furthest from 1, which is -1 . The DF value is

$$\mathcal{D}[h(f)] = \frac{1}{h(f)^H \Gamma(f) h(f)} \quad (2.84)$$

$$= \frac{|1 - e^{j2\pi f \tau_0(1-\alpha_{1,1})}|^2}{1 - \text{sinc}(2\pi f \tau_0) e^{j2\pi f \tau_0 \alpha_{1,1}} - \text{sinc}(2\pi f \tau_0) e^{-j2\pi f \tau_0 \alpha_{1,1}} + 1} \quad (2.85)$$

$$= \frac{\frac{1}{2}|1 - e^{j2\pi f \tau_0(1-\alpha_{1,1})}|^2}{1 - \text{sinc}(2\pi f \tau_0) \cos(2\pi f \tau_0 \alpha_{1,1})} \quad (2.86)$$

$$= \frac{1 - \cos(2\pi f \tau_0(1 - \alpha_{1,1}))}{1 - \text{sinc}(2\pi f \tau_0) \cos(2\pi f \tau_0 \alpha_{1,1})}. \quad (2.87)$$

To design a second-order uniform linear DMA [10], define

$$V(f) = \begin{bmatrix} d^H(f, 1) \\ d^H(f, \alpha_{2,1}) \\ d^H(f, \alpha_{2,2}) \end{bmatrix} \quad (2.88)$$

$$= \begin{bmatrix} 1 & v_1(f) & v_1^2(f) \\ 1 & v_2(f) & v_2^2(f) \\ 1 & v_3(f) & v_3^2(f) \end{bmatrix}. \quad (2.89)$$

$V(f)$ is a Vandermonde matrix where $v_1(f) = e^{j2\pi f \tau_0}$, $v_2(f) = e^{j2\pi f \tau_0 \alpha_{2,1}}$, $v_3(f) = e^{j2\pi f \tau_0 \alpha_{2,2}}$. $V^{-1}(f)$ can be decomposed into $U(f)L(f)$, where

$$U(f) = \begin{bmatrix} 1 & -v_1(f) & v_1(f)v_2(f) \\ 0 & 1 & -[v_1(f) + v_2(f)] \\ 0 & 0 & 1 \end{bmatrix} \quad (2.90)$$

and

$$L(f) = \begin{bmatrix} 1 & 0 & 0 \\ \frac{1}{v_1 - v_2} & \frac{1}{v_2 - v_1} & 0 \\ \frac{1}{(v_1 - v_2)(v_1 - v_3)} & \frac{1}{(v_2 - v_1)(v_2 - v_3)} & \frac{1}{(v_3 - v_1)(v_3 - v_2)} \end{bmatrix}. \quad (2.91)$$

The general second-order design can be written as

$$V(f)h(f) = \begin{bmatrix} 1 \\ \beta_{2,1} \\ \beta_{2,2} \end{bmatrix}. \quad (2.92)$$

Therefore, the solution is

$$h(f) = V^{-1}(f) \begin{bmatrix} 1 \\ \beta_{2,1} \\ \beta_{2,2} \end{bmatrix}. \quad (2.93)$$

For a third-order uniform linear DMA with three distinct nulls [10], the formula is

$$V(f)h(f) = \begin{bmatrix} 1 \\ 0 \\ 0 \\ 0 \end{bmatrix}, \quad (2.94)$$

where $V(f)$ is 4×4 . It is obvious that by knowing the first column of $V^{-1}(f)$, we can solve $h(f)$. The elements l_{ij} of $L(f)$ are

$$l_{ij} = \begin{cases} 0, & i < j \\ 1, & i = j = 1 \\ \prod_{p=1, p \neq j}^i \frac{1}{v_j - v_p}, & \text{otherwise} \end{cases}. \quad (2.95)$$

Hence, the first column of $L(f)$ is $\begin{bmatrix} 1 \\ \frac{1}{v_1 - v_2} \\ \frac{1}{(v_1 - v_2)(v_1 - v_3)} \\ \frac{1}{(v_1 - v_2)(v_1 - v_3)(v_1 - v_4)} \end{bmatrix}$. The elements u_{ij}

of $U(f)$ are

$$u_{ij} = \begin{cases} 1, & j = i \\ 0, & j = 1 \\ u_{i-1, j-1} - u_{i, j-1}v_{j-1}, & \text{otherwise} \end{cases}, \quad (2.96)$$

where $u_{0j} = 0$. Hence, we have

$$U(f) = \begin{bmatrix} 1 & -v_1 & v_1v_2 & -v_1v_2v_3 \\ 0 & 1 & -(v_1 + v_2) & v_1v_2 + v_1v_3 + v_2v_3 \\ 0 & 0 & 1 & -(v_1 + v_2 + v_3) \\ 0 & 0 & 0 & 1 \end{bmatrix}. \quad (2.97)$$

By knowing $U(f)$ and the first column of $L(f)$, we get

$$V^{-1}(f)[:, 1] = \begin{bmatrix} \frac{v_2 v_3 v_4}{(v_2 - v_1)(v_3 - v_1)(v_4 - v_1)} \\ -\frac{v_2 v_3 + v_3 v_4 + v_2 v_4}{(v_2 - v_1)(v_3 - v_1)(v_4 - v_1)} \\ \frac{v_2 + v_3 + v_4}{(v_2 - v_1)(v_3 - v_1)(v_4 - v_1)} \\ -\frac{1}{(v_2 - v_1)(v_3 - v_1)(v_4 - v_1)} \end{bmatrix} \quad (2.98)$$

The null-constrained approach can also be applied to a Concentric Circular Microphone Array (CCMA) composed of P rings[165]. The p th ring has a radius of r_p and consists of M_p omnidirectional microphones. The angular position of the m th array element on the p th ring is

$$\psi_{p,m} = \psi_{p,1} + \frac{2\pi(m-1)}{M_p}. \quad (2.99)$$

The p th ring's steering vector is

$$\mathbf{d}_p(\omega, \theta) = [e^{j\bar{\omega}_p \cos(\theta - \psi_{p,1})} \dots e^{j\bar{\omega}_p \cos(\theta - \psi_{p,M_p})}]^T, \quad (2.100)$$

with $\bar{\omega}_p = \omega r_p / c$. The steering vector of the whole microphone array is of length \underline{M} , where $\underline{M} = \sum_{p=1}^P M_p$. It is represented by

$$\underline{\mathbf{d}}(\omega, \theta) = [\mathbf{d}_1^T(\omega, \theta) \mathbf{d}_2^T(\omega, \theta) \dots \mathbf{d}_p^T(\omega, \theta)]^T. \quad (2.101)$$

Assume that the N th-order differential beamformer with the main beam pointing to θ_s has N distinct nulls: $\theta_s < \theta_1 < \dots < \theta_N \leq \theta_s + \pi$. We can now define

$$\underline{\mathbf{D}}(\omega) = \begin{bmatrix} \underline{\mathbf{d}}^H(\omega, \theta_s) \\ \underline{\mathbf{d}}^H(\omega, \theta_s + \Delta\theta_1) \\ \underline{\mathbf{d}}^H(\omega, \theta_s - \Delta\theta_1) \\ \vdots \\ \underline{\mathbf{d}}^H(\omega, \theta_s + \Delta\theta_N) \\ \underline{\mathbf{d}}^H(\omega, \theta_s - \Delta\theta_N) \end{bmatrix} \quad (2.102)$$

We use i_{2N+1} to denote a vector of length $(2N+1)$, whose first element is 1 and all other components are 0. The general solution for the Maximum White Noise Gain (MWNG) CCMA differential beamformer is:

$$\underline{\mathbf{h}}_{\text{MWNG}}(\omega) = \underline{\mathbf{D}}^H(\omega) [\underline{\mathbf{D}}(\omega) \underline{\mathbf{D}}^H(\omega)]^{-1} i_{2N+1}. \quad (2.103)$$

2.4 Mathematical Derivations

In this section, I provide detailed mathematical derivations. These derivations serve to elucidate commonly encountered terms in the literature on signal enhancement.

2.4.1 Minimum Norm Solution

Problem formulation:

$$\min \mathbf{x}^T \mathbf{x} \quad (2.104)$$

$$\text{s.t. } A\mathbf{x} = \mathbf{b} \quad (2.105)$$

Perpendicularity Perspective

Define $S = \{\mathbf{x} \in \mathbb{R}^N : A\mathbf{x} = \mathbf{b}\}$ and $S' = \{\mathbf{y} \in \mathbb{R}^N : A\mathbf{y} = \mathbf{0}\}$. Let $\mathbf{x}^{(0)}$ be an arbitrary element of S , which satisfies $A\mathbf{x}^{(0)} = \mathbf{b}$ and $S = S' + \mathbf{x}^{(0)}$. The minimum norm optimization can be interpreted as "finding the element of S closest to $\mathbf{0}$ " or "finding the element of S' closest to $-\mathbf{x}^{(0)}$ ". This can be illustrated in the Figure 2.2 below. We can observe that the vector from $\mathbf{0}$ to the optimal element \mathbf{x}^* is perpendicular to S' , i.e., $\mathbf{x}^* \cdot \mathbf{y} = \mathbf{0}$.

Since $A\mathbf{y} = \mathbf{0}$, \mathbf{y} belongs to the null space of A . Then $\mathbf{x}^* \cdot \mathbf{y} = \mathbf{0}$ implies that \mathbf{x}^* is orthogonal to the null space of A . It is known that the null space and the row space of a matrix are orthogonal complements. Therefore, \mathbf{x}^* must belong to the row space of A . We can set $\mathbf{x}^* = A^T \mathbf{w}$ for some \mathbf{w} . Substituting this into $A\mathbf{x} = \mathbf{b}$, we get $AA^T \mathbf{w} = \mathbf{b}$. Solving for \mathbf{w} , we get $\mathbf{w} = (AA^T)^{-1} \mathbf{b}$. Thus, $\mathbf{x}^* = A^T \mathbf{w} = A^T (AA^T)^{-1} \mathbf{b}$.

When we look at S instead of S' , we can see that another perpendicular relationship happens between \mathbf{x}^* and $\mathbf{x} - \mathbf{x}^*$. We have

$$\|\mathbf{x}^2\| = \|\mathbf{x}^* + \mathbf{x} - \mathbf{x}^*\|^2 = \|\mathbf{x}^*\|^2 + \|\mathbf{x} - \mathbf{x}^*\|^2 \geq \|\mathbf{x}^*\|^2. \quad (2.106)$$

This equation proves that \mathbf{x}^* gives the minimum norm.

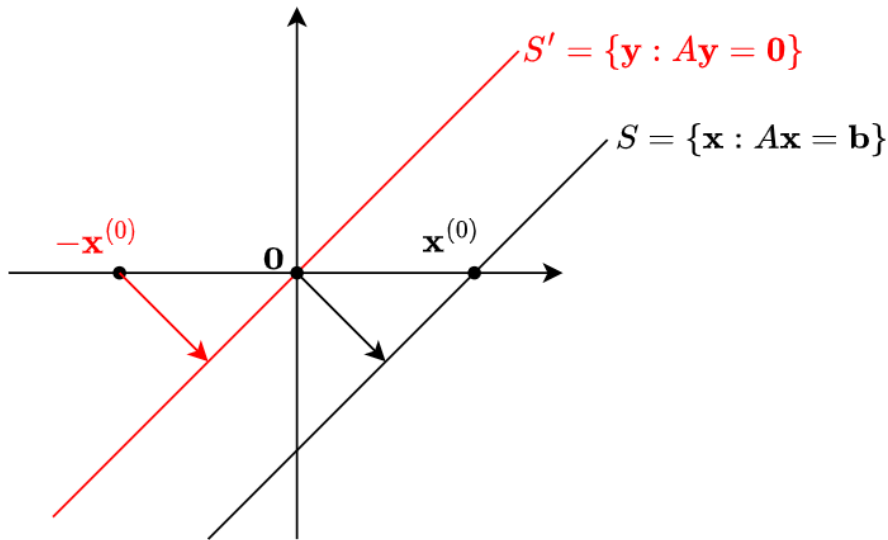


Figure 2.2: Two interpretations of the minimum norm problem

Convex Optimization Perspective

The Lagrangian of the minimum norm problem is

$$L(\mathbf{x}, \nu) = \mathbf{x}^T \mathbf{x} + \nu^T (A\mathbf{x} - \mathbf{b}). \quad (2.107)$$

Since $\nabla_{\mathbf{x}} L(\mathbf{x}, \nu) = 2\mathbf{x} + A^T \nu$, we get $\mathbf{x}^* = -(1/2)A^T \nu$ when $\nabla_{\mathbf{x}} L(\mathbf{x}, \nu) = 0$. The Lagrange dual is

$$g(\nu) = \inf_x L(\mathbf{x}, \nu) = -(1/4)\nu^T A A^T \nu - \mathbf{b}^T \nu. \quad (2.108)$$

The maximum of $g(\nu)$ is achieved when $\nu^* = -2(AA^T)^{-1}\mathbf{b}$. Substituting this back into $\mathbf{x}^* = -(1/2)A^T \nu$, we get $\mathbf{x}^* = A^T (AA^T)^{-1}\mathbf{b}$.

2.4.2 Verify Positive Semidefinite Matrix

A matrix A is positive semidefinite if and only if it can be written as $A = R^T R$ for some possibly rectangular matrix R .

Proof.

$$\mathbf{x}^T A \mathbf{x} = \mathbf{x}^T R^T R \mathbf{x} = (R \mathbf{x})^T (R \mathbf{x}) = \|R \mathbf{x}\|^2 \quad (2.109)$$

□

If columns of R are independent, then A is positive definite.

2.4.3 Trace of Matrix Product

For positive semidefinite matrices A, B , $\text{tr}(AB) \leq \text{tr}(A)\text{tr}(B)$.

Proof.

$$\begin{aligned} \text{tr}(AB) &= \text{tr}(A^{1/2} B^{1/2} B^{1/2} A^{1/2}) \\ &= \|A^{1/2} B^{1/2}\|_F^2 \\ &\leq \|A^{1/2}\|_F^2 \|B^{1/2}\|_F^2 \\ &= \text{tr}(A)\text{tr}(B) \end{aligned} \quad (2.110)$$

□

2.4.4 Trace Inequality

Let K and S be $n \times n$ matrices. If K is positive semidefinite and S is symmetric, then

$$\lambda_{\min}(S)\text{tr}(K) \leq \text{tr}(KS) \leq \lambda_{\max}(S)\text{tr}(K). \quad (2.111)$$

Proof. Let $D = U'SU$, where D is a diagonal matrix formed by the eigenvalues of S and U is an orthogonal matrix whose columns are normalized eigenvectors. We have

$$U'KSU = (U'KU)(U'SU). \quad (2.112)$$

Then

$$\text{tr}(KS) = \text{tr}(U'KSU) = \text{tr}(U'KUD). \quad (2.113)$$

Since $U'KU \geq 0$ and D is diagonal formed by eigenvalues of S , it follows that

$$\lambda_{\min}(S)\text{tr}(U'KU) \leq \text{tr}(KS) \leq \lambda_{\max}(S)\text{tr}(U'KU), \quad (2.114)$$

$$\lambda_{\min}(S)\text{tr}(K) \leq \text{tr}(KS) \leq \lambda_{\max}(S)\text{tr}(K) \quad (2.115)$$

□

2.4.5 Condition Number for Inversion

The norm of a matrix measures the maximum stretching a matrix does to any vector in a given vector norm. It is defined by

$$\|A\| = \max_{x \neq 0} \frac{\|Ax\|}{\|x\|}. \quad (2.116)$$

The matrix norm corresponding to vector 1-norm is maximum absolute column sum

$$\|A\|_1 = \max_j \sum_{i=1}^n |a_{ij}|. \quad (2.117)$$

The matrix norm corresponding to vector ∞ -norm is maximum absolute row sum

$$\|A\|_\infty = \max_i \sum_{j=1}^n |a_{ij}|. \quad (2.118)$$

The condition number of a matrix A is defined by

$$\text{cond}(A) = \|A\| \cdot \|A^{-1}\|. \quad (2.119)$$

If $\text{cond}(A)$ is infinity, then A is singular. If $\text{cond}(A)$ is a finite large number, then A is close to singular. The condition number can be interpreted as the ratio of the maximum relative stretching to the maximum relative shrinking that matrix does to any non zero vectors. When A is positive definite and symmetric, the condition number with 2-norm can be simplified to the ratio of the largest eigenvalue of A to the smallest eigenvalue of A .

Chapter 3

Linear Time Finite Basis Independence Criterion

Detection of statistical dependence between random variables is an essential component in many machine learning algorithms. We propose a novel independence criterion for two random variables with linear-time complexity. We establish that our independence criterion is an upper bound of the Hirschfeld-Gebelein-Rényi maximum correlation coefficient between tested variables. A finite set of basis functions is employed to approximate the mapping functions that can achieve the maximal correlation. Using classic benchmark experiments based on independent component analysis, we demonstrate that our independence criterion performs comparably with the state-of-the-art quadratic-time kernel dependence measures like the Hilbert-Schmidt Independence Criterion, while being more efficient in computation. The experimental results also show that our independence criterion outperforms another contemporary linear-time kernel dependence measure, the Finite Set Independence Criterion. The potential application of our criterion in deep neural networks is validated experimentally.

3.1 Introduction

Measures of dependence between random variables have been extensively studied in statistics and in science. Statistical quantities such as non-Gaussianity, cross-cumulants and mutual information have been used for dependence detection in Independent Component Analysis (ICA) [75, 5, 18]. Among them, mutual information is the most popular dependence measure. It measures the Kullback-Leibler divergence between the joint probability distribution of two random variables and the product of their marginal distributions.

Mutual information can be difficult to measure and optimize with a finite sample [3]. Alternative measurements in a Reproducing Kernel Hilbert Space (RKHS) have shown superior performance in detecting statistical dependence [3, 55, 57]. [3] developed a kernel method to search for mapping functions in an RKHS that can achieve the maximal correlation, also known as the Hirschfeld-Gebelein-Rényi (HGR) maximum correlation coefficient [63, 44, 139], between observed signals. This Kernel ICA approach is robust to near-Gaussianity and outliers. The Hilbert Schmidt Independence Criterion (HSIC) proposed by [55] exhibits the best performance to date. It searches for RKHS functions that can maximize the norm of the cross-covariance operator. It is robust under challenging environments and alert to small deviations from independence.

The advantage of HSIC comes at a price. Its quadratic computational time slows down the calculation. Additionally, for input signals with a large sample size, it is infeasible to use HSIC to compute the statistical independence [81]. This disadvantage cannot be overlooked in an era of big data. It is also observed that the stability of HSIC is not guaranteed as it is sensitive to the initial conditions. In ICA experiments, when the initial demixing matrix is not properly guessed, HSIC can suffer from local optima and perform poorly [148].

To address the high computational expense of HSIC, the Finite Set In-

dependence Criterion (FSIC) was developed [81]. Instead of constructing a Gram matrix that requires a computation between every single pair of signal observations, FSIC selects a finite set of test locations to be compared with input signals. Empirically it has been shown that a small set of test locations is sufficient to provide test power [81]. This makes FSIC a linear-time algorithm. By focusing on the key regions captured by test locations that signify differences between two input signals, the estimation of the covariance matrix can be made more efficient and accurate.

In order to search for key regions and tune parameters for kernels, FSIC splits the data into training and test sets. Only the training set is exploited for the parameter tuning to avoid overfitting. The test set alone is used for independence measurement. This approach has two problems. Firstly, the training stage prevents FSIC from being an online algorithm. Secondly, the data splitting can be problematic. For example, if the data distribution is not stationary, it is quite likely that the training set will not reflect the true properties of the test set. These disadvantages make it cumbersome to integrate FSIC effectively into machine learning algorithms like ICA.

Comparing different dependence measures in a fair manner is not a trivial task. Given a finite sample, no test of independence is reliable [57]. The universal limit on dependence tests affirms that the lower Type I error a dependence test has, the higher Type II error it can suffer from [57]. In practical applications, one good benchmark to evaluate dependence measures is linear instantaneous ICA [55]. In linear ICA, the aim is to extract original independent source signals when the only available information is a set of linearly mixed signal mixtures [111]. Performing the signal separation in ICA algorithms depends on good measurement of dependence. The linear instantaneous mixing creates a signal mixture that can be demixed up to an indeterminacy of scale and permutation [29]. Thus, evaluating the estimated demixing matrix from the ICA algorithm against the ground truth mixing matrix can indicate the optimization efficacy of the dependence measure employed. The ICA benchmark experiments put

forward by [3] have become a standard practice for evaluating many dependence measures [75, 18, 5, 102, 19, 3, 56, 148, 134].

We propose a new dependence measure called the Finite Basis Independence Criterion (FBIC). It is a linear-time independence measure derived from the fact that the mapping functions attaining the maximal correlation can be approximated in a subspace built by finite basis functions. It follows the spirit of the HGR maximum correlation coefficient. Our experimental results have shown that FBIC can perform similarly to HSIC and FSIC on various data distributions. FBIC is a direct application of Property (F) in [139]: the maximal correlation between two random variables is invariant with respect to all one-to-one Borel measurable transformations.

Recently, [120] suggested that the strong one-to-one invariance assumption of dependence measures should be replaced by similarity invariance and weak continuity. This relaxation of invariance is claimed to be instrumental for distribution robustness [120]. They have shown that certain pathological random variables artificially constructed may confuse the maximal correlation measurement. However, detailed examination of pros and cons between different invariance assumptions of dependence measures has not been tested experimentally, and is outside of the scope of this chapter.

Our contributions include:

- We develop a new framework for an upper bound of independence criterion on the basis of the HGR maximum correlation coefficient.
- We establish the effectiveness of four sets of basis functions, including three sets of RBFs and one set of polynomial functions, both theoretically and experimentally.
- We demonstrate the superior performance of FBIC on dependence detection in a comprehensive ICA benchmark, which shows the validity of applying FBIC in machine learning loss functions through

gradient descent.

The remainder of the chapter is organized as follows. Section 3.2 introduces an evolution from HSIC to FSIC. Section 3.3 describes the details of the proposed FBIC algorithm. Section 3.4 explains the experiment design. Section 3.5 provides the conclusion and outlines future work.

3.2 Background

3.2.1 RKHS-based Independence Measures

A Hilbert space \mathcal{H} is a complete inner product space. An RKHS is a Hilbert space where point evaluation is a continuous linear functional. Thus, by the Riesz representation theorem [115] which states that any functional mapping \mathcal{H} into \mathbb{R} can be represented by an inner product, an RKHS has the Reproducing Property that $f(x) = \langle f, \phi(x) \rangle_{\mathcal{H}}$, where $f : \mathcal{X} \rightarrow \mathbb{R}$ is a functional in the RKHS, x belongs to \mathcal{X} and $\phi(x)$ is a feature map from \mathcal{X} to \mathcal{H} . The feature map takes the canonical form $\phi(x) = k(x, \cdot)$, where $k(x_1, x_2) : \mathcal{X} \times \mathcal{X} \rightarrow \mathbb{R}$ is a positive definite kernel. In other words, the inner product of two feature map can be evaluated by a kernel: $\langle \phi(x), \phi(y) \rangle_{\mathcal{H}} = k(x, y)$.

Let x and y be random variables defined on a topological space \mathcal{X} , with respective Borel probability measures p and q . Let \mathcal{T} be a class of functions $f : \mathcal{X} \rightarrow \mathbb{R}$. The Maximum Mean Discrepancy (MMD) is defined as [54]:

$$\text{MMD}(\mathcal{T}, p, q) := \sup_{f \in \mathcal{T}} (\mathbf{E}_x[f(x)] - \mathbf{E}_y[f(y)]), \quad (3.1)$$

where $\mathbf{E}_x[f(x)]$ and $\mathbf{E}_y[f(y)]$ denote expectations with respect to p and q .

The MMD can be considered as an integral probability metric [122]. Let (\mathcal{X}, d) be a metric space. We have $p = q$ if and only if $\mathbf{E}_x[f(x)] = \mathbf{E}_y[f(y)]$ for all $f \in C(\mathcal{X})$, where $C(\mathcal{X})$ is the space of bounded continuous functions on \mathcal{X} .

In real life, it is not practical to work with a rich function class like $C(\mathcal{X})$. The MMD requires a function class that is rich enough to identify $p = q$ uniquely, yet restrictive enough so that the MMD can be estimated by finite samples. It turns out that the unit ball in an RKHS \mathcal{H} can satisfy both conditions.

Define the mean embedding of p in an RKHS as $\mu_p \in \mathcal{H}$ such that $\mathbf{E}_x f = \langle f, \mu_p \rangle_{\mathcal{H}}$. The formula for the MMD in Equation 3.1 can be rewritten as:

$$\begin{aligned} \text{MMD}^2(\mathcal{T}, p, q) &= \left[\sup_{\|f\|_{\mathcal{H}} \leq 1} (\mathbf{E}_x[f(x)] - \mathbf{E}_y[f(y)]) \right]^2 \end{aligned} \quad (3.2)$$

$$= \left[\sup_{\|f\|_{\mathcal{H}} \leq 1} \langle \mu_p - \mu_q, f \rangle_{\mathcal{H}} \right]^2 \quad (3.3)$$

$$= \|\mu_p - \mu_q\|_{\mathcal{H}}^2 \quad (3.4)$$

$$= \langle \mu_p, \mu_p \rangle_{\mathcal{H}} + \langle \mu_q, \mu_q \rangle_{\mathcal{H}} - 2\langle \mu_p, \mu_q \rangle_{\mathcal{H}} \quad (3.5)$$

$$\begin{aligned} &= \mathbf{E}_{x,x'} \langle \phi(x), \phi(x') \rangle_{\mathcal{H}} + \mathbf{E}_{y,y'} \langle \phi(y), \phi(y') \rangle_{\mathcal{H}} \\ &\quad - 2\mathbf{E}_{x,y} \langle \phi(x), \phi(y) \rangle_{\mathcal{H}}. \end{aligned} \quad (3.6)$$

Let $X := \{x_1, \dots, x_m\}$ and $Y := \{y_1, \dots, y_n\}$ be observations independently and identically drawn from p and q . By using the empirical estimates of the feature space based on X and Y , we obtain

$$\text{MMD}^2(\mathcal{T}, X, Y) = \left[\frac{1}{m^2} \sum_{i,j=1}^m k(x_i, x_j) - \frac{2}{mn} \sum_{i,j=1}^{m,n} k(x_i, y_j) + \frac{1}{n^2} \sum_{i,j=1}^n k(y_i, y_j) \right]. \quad (3.7)$$

Empirical HSIC

Let $Z \subseteq \mathcal{X} \times \mathcal{Y}$ be samples independently drawn from P_{xy} . Let us use shorthand notations $k_{ij} = k(x_i, x_j)$ and $l_{ij} = l(y_i, y_j)$. Gram matrices K

and L can be defined by $K_{ij} = k_{ij}$ and $L_{ij} = l_{ij}$. The empirical HSIC is given by:

$$\begin{aligned}
& \widehat{\text{HSIC}}(Z, \mathcal{F}, \mathcal{G}) \\
& := \frac{1}{n^2} \sum_{i=1}^n \sum_{j=1}^n k_{ij} l_{ij} + \frac{1}{n^4} \left(\sum_{i=1}^n \sum_{j=1}^n k_{ij} \right) \left(\sum_{i=1}^n \sum_{j=1}^n l_{ij} \right) \\
& \quad - \frac{2}{n^3} \sum_{i=1}^n \sum_{j=1}^n \sum_{q=1}^n k_{ij} l_{iq} \\
& = \frac{1}{n^2} \text{tr}(KL) + \frac{1}{n^4} (1_n^T K 1_n) (1_n^T L 1_n) - \frac{2}{n^3} 1_n^T K L 1_n \\
& = \frac{1}{n^2} \text{tr}(KHLH), \tag{3.8}
\end{aligned}$$

where 1_n is an $n \times n$ matrix of ones and $H := I - \frac{1}{n} 1_n 1_n^T$.

3.2.2 From HSIC to FSIC

Due to their high performance, kernel-based independence measurements like HSIC and FSIC have been studied extensively in recent years [3, 55, 57, 81, 148]. They satisfy the framework introduced by [139], stating that the maximal correlation (or cross-covariance) results from sufficiently rich function classes is zero if and only if the random variables tested are independent. These methods are related to a test statistic comparing distributions called Maximum Mean Discrepancy (MMD) [54]. By using the unit ball of an RKHS, the MMD between distributions can be detected.

HSIC is a robust kernel-based independence measurement as it utilizes the sum of the squared singular values in the cross-covariance operator instead of only the largest singular value like the Constrained Covariance (COCO) approach [57]. The summed up quantity is called the squared Hilbert-Schmidt norm, which is the RKHS counterpart of the squared Frobenius norm.

Let \mathcal{F} and \mathcal{G} be two RKHSs with corresponding positive definite kernels $k : \mathcal{X} \times \mathcal{X} \rightarrow \mathbb{R}$ and $l : \mathcal{Y} \times \mathcal{Y} \rightarrow \mathbb{R}$, respectively. For all $x \in \mathcal{X}$

and $y \in \mathcal{Y}$, the Reproducing Property gives us $k(x, x') = \langle \phi(x), \phi(x') \rangle$ and $l(y, y') = \langle \psi(y), \psi(y') \rangle$, where $\phi : \mathcal{X} \rightarrow \mathcal{F}$ and $\psi : \mathcal{Y} \rightarrow \mathcal{G}$ are feature maps. The mean embeddings of the probability distributions of x in \mathcal{F} and of y in \mathcal{G} are defined as μ_x and μ_y respectively:

$$\begin{aligned}\langle \mu_x, f \rangle_{\mathcal{F}} &:= \mathbf{E}_x[\langle \phi(x), f \rangle_{\mathcal{F}}] = \mathbf{E}_x[f(x)], \\ \langle \mu_y, g \rangle_{\mathcal{G}} &:= \mathbf{E}_y[\langle \psi(y), g \rangle_{\mathcal{G}}] = \mathbf{E}_y[g(y)],\end{aligned}\tag{3.9}$$

where $f \in \mathcal{F}$ and $g \in \mathcal{G}$. Given $a \in \mathcal{F}$ and $b \in \mathcal{G}$, the tensor product operator $a \otimes b : \mathcal{G} \rightarrow \mathcal{F}$ is defined as

$$(a \otimes b)g := a \langle b, g \rangle_{\mathcal{G}} \text{ for all } g \in \mathcal{G}.\tag{3.10}$$

Note that this reduces to $a \otimes b = ab^T$ for finite-dimensional vector spaces. It follows that the cross-covariance operator $C_{xy} : \mathcal{G} \rightarrow \mathcal{F}$ is defined as

$$\begin{aligned}C_{xy} &:= \mathbf{E}_{x,y}[(\phi(x) - \mu_x) \otimes (\psi(y) - \mu_y)] \\ &= \mathbf{E}_{x,y}[\phi(x) \otimes \psi(y)] - \mu_x \otimes \mu_y.\end{aligned}\tag{3.11}$$

The derivation of the cross-covariance operator C_{xy} can be further explained in the following:

$$\langle f, C_{xy}g \rangle_{\mathcal{F}} = \langle C_{xy}, f \otimes g \rangle_{\text{HS}}\tag{3.12}$$

$$= \mathbf{E}_{x,y} \langle (\phi(x) - \mu_x) \otimes (\psi(y) - \mu_y), f \otimes g \rangle_{\text{HS}}\tag{3.13}$$

$$\begin{aligned}&= \mathbf{E}_{x,y}[\langle f, \phi(x) - \mu_x \rangle \langle g, \psi(y) - \mu_y \rangle] \\ &= \mathbf{E}_{x,y}[(\langle f, \phi(x) \rangle - \langle f, \mu_x \rangle)(\langle g, \psi(y) \rangle - \langle g, \mu_y \rangle)]\end{aligned}$$

$$\begin{aligned}&= \mathbf{E}_{x,y}[(f(x) - \mathbf{E}_x[f(x)])(g(y) - \mathbf{E}_y[g(y)])] \\ &= \mathbf{E}_{x,y}[f(x)g(y)] - \mathbf{E}_x[f(x)]\mathbf{E}_y[g(y)] \\ &= \mathbf{E}_{x,y} \langle \phi(x) \otimes \psi(y), f \otimes g \rangle - \langle \mu_x \otimes \mu_y, f \otimes g \rangle\end{aligned}\tag{3.14}$$

$$\begin{aligned}&= \mathbf{E}_{x,y} \langle \phi(x) \otimes \psi(y), f \otimes g \rangle - \mathbf{E}_{x,y} \langle \mu_x \otimes \mu_y, f \otimes g \rangle \\ &= \mathbf{E}_{x,y} \langle \phi(x) \otimes \psi(y) - \mu_x \otimes \mu_y, f \otimes g \rangle,\end{aligned}\tag{3.15}$$

where (3.12) follows Equation (3) in [55], (3.13) and (3.14) follows Lemma 7 in [17]. The rest of the steps can be obtained from algebraic manipulations.

Denote $\mathbf{E}_{x,y}[\phi(x) \otimes \psi(y)]$ by \tilde{C}_{xy} and the joint distribution over $\mathcal{X} \times \mathcal{Y}$ by P_{xy} . Let $C : \mathcal{G} \rightarrow \mathcal{F}$ be a linear operator. The Hilbert-Schmidt norm of C is defined as:

$$\|C\|_{\text{HS}} := \sqrt{\sum_{i,j} \langle Cv_j, u_i \rangle_{\mathcal{H}}^2}, \quad (3.16)$$

where u_i and v_j are orthonormal bases of \mathcal{F} and \mathcal{G} respectively.

A linear operator $C : \mathcal{G} \rightarrow \mathcal{F}$ is called a Hilbert-Schmidt operator if its Hilbert-Schmidt norm exists. The set of Hilbert-Schmidt operators is a separable Hilbert space with inner product

$$\langle C, D \rangle_{\text{HS}} = \sum_{i,j} \langle Cv_j, u_i \rangle_{\mathcal{H}} \langle Dv_j, u_i \rangle_{\mathcal{H}}. \quad (3.17)$$

We can now define HSIC as the squared Hilbert-Schmidt norm of the associated cross-covariance operator C_{xy} :

$$\begin{aligned} \text{HSIC}(P_{xy}, \mathcal{F}, \mathcal{G}) &:= \|C_{xy}\|_{\text{HS}}^2 \\ &= \left\| \tilde{C}_{xy} - \mu_x \otimes \mu_y \right\|_{\text{HS}}^2 \\ &= \langle \tilde{C}_{xy}, \tilde{C}_{xy} \rangle_{\text{HS}} + \langle \mu_x \otimes \mu_y, \mu_x \otimes \mu_y \rangle_{\text{HS}} - 2\langle \tilde{C}_{xy}, \mu_x \otimes \mu_y \rangle_{\text{HS}} \\ &= \mathbf{E}_{x,y} \mathbf{E}_{x',y'} [k(x, x')l(y, y')] + \mathbf{E}_x \mathbf{E}_y \mathbf{E}_{x'} \mathbf{E}_{y'} [k(x, x')l(y, y')] \\ &\quad - 2\mathbf{E}_{x,y} \mathbf{E}_{x'} \mathbf{E}_{y'} [k(x, x')l(y, y')]. \end{aligned} \quad (3.18)$$

Denote the marginal distributions over \mathcal{X} and \mathcal{Y} by P_x and P_y respectively. Let \mathcal{T} be the unit ball in an RKHS associated with a kernel $v : \mathcal{F} \times \mathcal{G} \rightarrow \mathbb{R}$. HSIC associated with C_{xy} is equivalent to the squared MMD between the joint distribution P_{xy} and the product of its marginal distributions $P_x P_y$ [17]:

$$\text{MMD}^2(\mathcal{T}, P_{xy}, P_x P_y) = \text{HSIC}(P_{xy}, \mathcal{F}, \mathcal{G}). \quad (3.19)$$

The equivalence between MMD and HSIC can be shown below from the derivations adapted from Lemma 9 in [17]. Define a kernel v in the tensor product space $\mathcal{F} \times \mathcal{G}$ as $v((x, y)(x', y')) = k(x, x')l(y, y')$. The RKHS associated with v is \mathcal{H}_v . We have:

$$\begin{aligned}
\text{MMD}^2(\mathcal{T}, P_{xy}, P_x P_y) &= \|\mu P_{xy} - \mu P_x P_y\|_{\mathcal{H}_v}^2 \\
&= \|\mathbf{E}_{x,y} v((x, y), \cdot) - \mathbf{E}_x \mathbf{E}_y v((x, y), \cdot)\|_{\mathcal{H}_v}^2 \\
&= \|\mathbf{E}_{x,y} k(x, \cdot) l(y, \cdot) - \mathbf{E}_x \mathbf{E}_y k(x, \cdot) l(y, \cdot)\|_{\mathcal{H}_v}^2 \\
&= \|\mathbf{E}_{x,y} k(x, \cdot) l(y, \cdot) - \mathbf{E}_x k(x, \cdot) \mathbf{E}_y l(y, \cdot)\|_{\mathcal{H}_v}^2 \\
&= \langle \mathbf{E}_{x,y} k(x, \cdot) l(y, \cdot), \mathbf{E}_{x',y'} k(x', \cdot) l(y', \cdot) \rangle_{\mathcal{H}_v} \\
&\quad + \langle \mathbf{E}_x k(x, \cdot) \mathbf{E}_y l(y, \cdot), \mathbf{E}_{x'} k(x', \cdot) \mathbf{E}_{y'} l(y', \cdot) \rangle_{\mathcal{H}_v} \\
&\quad - 2 \langle \mathbf{E}_{x,y} k(x, \cdot) l(y, \cdot), \mathbf{E}_{x'} k(x', \cdot) \mathbf{E}_{y'} l(y', \cdot) \rangle_{\mathcal{H}_v} \\
&= \mathbf{E}_{x,y} \mathbf{E}_{x',y'} [k(x, x') l(y, y')] + \mathbf{E}_x \mathbf{E}_y \mathbf{E}_{x'} \mathbf{E}_{y'} [k(x, x') l(y, y')] \\
&\quad - 2 \mathbf{E}_{x,y} \mathbf{E}_{x'} \mathbf{E}_{y'} [k(x, x') l(y, y')] \\
&= \text{HSIC}(P_{xy}, \mathcal{F}, \mathcal{G}).
\end{aligned}$$

FSIC is related to MMD in the sense that it also measures a difference between mean embeddings in RKHSs. However, the maximum distance aspect is not required in FSIC. Define the empirical measure $\nu := \frac{1}{J} \sum_{i=1}^J \delta_{(v_i, w_i)}$ over J test locations $V_J := \{(v_i, w_i)\}_{i=1}^J \subset \mathcal{X} \times \mathcal{Y}$, where δ_t denotes the Dirac measure centered on t . Let μ_{xy} , μ_x and μ_y represent mean embeddings of P_{xy} , P_x and P_y . Define random variables $X \in \mathcal{X}$ and $Y \in \mathcal{Y}$. Using $L^2(\mathcal{X} \times \mathcal{Y}, \nu)$ to measure the distance between μ_{xy} and $\mu_x \mu_y$, FSIC is defined by:

$$\text{FSIC}^2[X, Y] := \|\mu_{xy} - \mu_x \mu_y\|_{L^2(\mathcal{X} \times \mathcal{Y}, \nu)}^2 \quad (3.20)$$

$$= \int_{\mathcal{X}} \int_{\mathcal{Y}} (\mu_{xy}(x, y) - \mu_x(x) \mu_y(y))^2 d\nu(x, y) \quad (3.21)$$

$$= \frac{1}{J} \sum_{i=1}^J u(v_i, w_i)^2, \text{ where} \quad (3.22)$$

$$u(v, w) := \mu_{xy}(v, w) - \mu_x(v)\mu_y(w) \quad (3.23)$$

$$= \mathbf{E}_{x,y}[k(x, v)l(y, w)] - \mathbf{E}_x[k(x, v)]\mathbf{E}_y[l(y, w)] \quad (3.24)$$

$$= \mathbf{cov}_{xy}[k(x, v), l(y, w)]. \quad (3.25)$$

FSIC is a good measure for independence testing purpose, but it is not easy to employ it in machine learning algorithms like ICA due to the training data requirement for the test location optimization.

Assumptions of FSIC

A positive definite kernel $k : \mathcal{X} \times \mathcal{X} \rightarrow \mathbb{R}$ is said to be analytic on its domain $\mathcal{X} \times \mathcal{X}$ if for all $\mathbf{v} \in \mathcal{X}$, $f(\mathbf{x}) := k(\mathbf{x}, \mathbf{v})$ is an analytic function on \mathcal{X} [28]. \mathcal{P} denotes the set of all Borel probability measures on a topological space (M, \mathcal{A}) . For a set $\mathcal{L} \subset \mathcal{P}$, $\gamma(\mathbb{P}, \mathbb{Q})$ is a metric for any $\mathbb{P}, \mathbb{Q} \in \mathcal{L}$. A bounded measurable positive definite kernel k is defined as *characteristic* if $\gamma(\mathbb{P}, \mathbb{Q}) = 0 \Leftrightarrow \mathbb{P} = \mathbb{Q}$ [151].

FSIC is a novel approach to measure independence in a linear time manner. It evaluates a random metric between two probability distributions at a finite number of points [81, 28]. This is possible when FSIC satisfies the assumption that the kernels $k : \mathcal{X} \times \mathcal{X} \rightarrow \mathbb{R}$ and $l : \mathcal{Y} \times \mathcal{Y} \rightarrow \mathbb{R}$ are bounded by B_k and B_l respectively, and the product kernel $g((\mathbf{x}, \mathbf{y}), (\mathbf{x}', \mathbf{y}')) := k(\mathbf{x}, \mathbf{x}')l(\mathbf{y}, \mathbf{y}')$ is characteristic and analytic on $(\mathcal{X} \times \mathcal{Y}) \times (\mathcal{X} \times \mathcal{Y})$ [151].

Empirical FSIC

Let $X := \{x_1, \dots, x_n\}$ and $Y := \{y_1, \dots, y_n\}$ be observations independently and identically drawn from P_x and P_y . The empirical estimate of FSIC can be written as:

$$\widehat{\text{FSIC}}^2(X, Y) = \frac{1}{J} \sum_{i=1}^J \hat{u}(v_i, w_i)^2, \text{ where} \quad (3.26)$$

$$\hat{u}(v, w) := \hat{\mu}_{xy}(v, w) - \widehat{\mu_x \mu_y}(v, w) \quad (3.27)$$

$$= \frac{1}{n} \sum_{i=1}^n k(x_i, v) l(y_i, w) - \frac{1}{n^2} \sum_{i=1}^n k(x_i, v) \sum_{j=1}^n l(y_j, w). \quad (3.28)$$

3.3 FBIC

Define nondegenerate univariate random variables X and Y whose observations $x = (x_1, \dots, x_m)^T$ and $y = (y_1, \dots, y_m)^T$ can represent signals of interest. Without loss of generality, we can scale observed signals x and y such that they are within the closed domain interval $[0, 1]$. Let $L^2[0, 1]$ be the square-integrable function space such that for $f(t) \in L^2[0, 1]$

$$\|f(t)\|_2 = \left(\int_0^1 |f(t)|^2 dt \right)^{1/2} < \infty, \quad (3.29)$$

where t is a real value defined on the closed domain interval $[0, 1]$. Let $C[0, 1]$ be the function space of real-valued continuous functions defined on the closed interval $[0, 1]$. We now define a function space $T = L^2[0, 1] \cap C[0, 1]$, which is an equivalence class of functions that are both square-integrable and continuous almost everywhere on the closed domain interval $[0, 1]$. A finite dimensional subspace $V \subseteq T$ can be built upon a set of basis functions $\mathcal{B} = \{p_i : [0, 1] \rightarrow \mathbb{R}\}$, where $i \in \{1, 2, \dots, N\}$ and N is a finite positive integer.

It has been shown in [3] that the maximal correlation can be used to measure independence between tested variables. The maximal correlation between x and y is:

$$\rho_{\max}[x, y] = \sup_{f_1, f_2 \in T} \left(\rho[f_1(x), f_2(y)] \right) = \sup_{f_1, f_2 \in T} \frac{\text{cov}(f_1(x), f_2(y))}{\sigma(f_1(x))\sigma(f_2(y))}, \quad (3.30)$$

where $\rho[\cdot, \cdot]$ denotes the Pearson Correlation, and $\sigma(\cdot)$ denotes the standard deviation.

We use the function space T for possible mapping functions employed in the maximal correlation. This is because the Pearson Correlation re-

quires the chosen functions to be square-integrable. The continuous property implies that the chosen functions are Borel-measurable. Define f_1^* and f_2^* such that $\rho_{\max}[x, y] = \rho[f_1^*(x), f_2^*(y)]$. We want to use the best approximations q_1 and q_2 of f_1^* and f_2^* in V that minimize the difference between $\rho[f_1^*(x), f_2^*(y)]$ and $\rho[q_1(x), q_2(y)]$. From the definition of V , we can write $q_1(x) = \sum_{i=1}^N a_i p_i(x)$ and $q_2(y) = \sum_{j=1}^N b_j p_j(y)$. The standard deviation can be scaled by a multiplication factor and it will be divided for normalization in Pearson Correlation in the end. To simplify the notation and leave out the standard deviation, we can rescale all mapping functions in T to have unit standard deviation when applied to test variables.

3.3.1 Definition of FBIC

We propose that the Finite Basis Independence Criterion (FBIC) can imply independence by measuring the pair-wise correlations between the basis function mappings from tested variables. This can be expressed with a set of basis functions $\{p_i\}$ from \mathcal{B} :

$$\begin{aligned} \text{FBIC}(\mathcal{B}, X, Y) &= \sum_{i=1}^N \sum_{j=1}^N \left| \rho_{ij}[x, y] \right| \\ &= \sum_{i=1}^N \sum_{j=1}^N \left| \mathbf{E}[(p_i(x) - \mathbf{E}[p_i(x)])(p_j(y) - \mathbf{E}[p_j(y)])] \right|. \end{aligned} \quad (3.31)$$

Let Q_x and Q_y be the probability density functions of x and y respectively. Let $X := \{x_1, \dots, x_m\}$ and $Y := \{y_1, \dots, y_m\}$ be observations independently and identically drawn from Q_x and Q_y . The empirical FBIC is:

$$\begin{aligned} \widehat{\text{FBIC}}(\mathcal{B}, X, Y) &= \sum_{i=1}^N \sum_{j=1}^N \left| \frac{1}{m} \sum_{k=1}^m [(p_i(x_k) \right. \\ &\quad \left. - \frac{1}{m} \sum_{s=1}^m p_i(x_s))(p_j(y_k) - \frac{1}{m} \sum_{t=1}^m p_j(y_t))] \right|. \end{aligned} \quad (3.32)$$

3.3.2 Basis Functions in FBIC

The choice of basis function sets is crucial for the good performance of the FBIC. Our first category of basis functions are inspired by the RBF neural networks, which have the universal approximation capacity [168]. A RBF $K(\cdot)$ is a radially symmetric function such that $\|x\|_p = \|y\|_p$ implies $K(x) = K(y)$ [130]. Here we use a general norm notation $\|\cdot\|_p$ to include more than the Euclidean norm for the construction of RBFs.

A finite set of RBFs can approximate any function in T arbitrarily well. This can be corroborated by the Theorem 1 of [130], which states that for functions that are integrable, bounded, continuous almost everywhere and has non-zero integral, a finite sum of these functions with coefficients is dense in p -integrable function spaces for every $p \in [1, \infty)$. RBFs that we choose should satisfy these properties and are, hence dense in T , a subset of the square-integrable function space.

Three sets of RBFs are tested in this chapter. They are Gaussian RBFs, Laplacian RBFs and Inverse Multiquadratic RBFs. They are listed below:

$$\left\{ \begin{array}{ll} \text{Gaussian:} & K(x) = e^{-\epsilon(x-c)^2} \\ \text{Laplacian:} & K(x) = e^{-\epsilon|x-c|} \\ \text{Inverse Multiquadratic:} & K(x) = \frac{1}{\sqrt{1+\epsilon(x-c)^2}}. \end{array} \right. \quad (3.33)$$

We define $\epsilon \in (0, \infty)$ as the shape parameter and $c \in [0, 1]$ as the displacement parameter for the RBFs in Equation 3.33. The smaller the ϵ , the flatter the shape of RBFs [118]. RBFs of the same category share the same shape parameter. The displacement parameters are equally distanced grid points. For example, when there are 10 RBFs in a set, $c = \{0, 0.1, 0.2, \dots, 0.9\}$.

Another category of basis functions is the Shifted Legendre Polynomials. They are orthogonal polynomials that can play the role of orthogonal basis functions. This is a natural choice for a finite set of basis functions as orthogonality is numerically effective for function approximation [136].

Let $P_n(x)$ be a polynomial of degree n . Legendre Polynomials satisfy

the condition that

$$\int_{-1}^1 P_m(x)P_n(x)dx = 0, \text{ if } n \neq m. \quad (3.34)$$

$P_0(x)$ is generally set to 1 for standardization. Shifted Legendre Polynomials are defined as $\tilde{P}_n(x) = P_n(2x - 1)$. They satisfy the condition that

$$\int_0^1 \tilde{P}_m(x)\tilde{P}_n(x)dx = 0, \text{ if } n \neq m. \quad (3.35)$$

Shifted Legendre Polynomials are preferred as they are orthogonal on the interval $[0, 1]$, which corresponds to our function space T . For one set of Shifted Legendre Polynomial basis functions, they are distinguished by different polynomial degrees n .

The Weierstrass's theorem states that a continuous function on a closed interval can be approximated arbitrarily well by polynomials [77]. Therefore, Shifted Legendre Polynomials can be regarded as the orthogonal basis for the construction of any continuous function on a closed interval [94]. Since any polynomial can be decomposed into Shifted Legendre Polynomials and there exists some good polynomial approximation for any function in T , this suggests that Shifted Legendre Polynomials can approximate any function in T arbitrarily well given a sufficient number of degrees.

3.3.3 Justifications for FBIC

Theorem 1. *Given a sufficient set of basis functions, FBIC gives an upper bound to the maximal correlation between tested variables with an arbitrarily small positive error bound Δ .*

Proof. Define $\gamma_{ij} = \hat{a}_i\hat{b}_j$. Let \hat{a}_i and \hat{b}_j be scaled coefficients a_i and b_j from the definitions of q_1 and q_2 . \hat{a}_i and \hat{b}_j are within $[-1, 1]$. The coefficients can be scaled as the Pearson Correlation is scale invariant. From the definition

of FBIC in Equation 3.31, we can derive an inequality as follows:

$$\begin{aligned}
\text{FBIC}[\mathcal{B}, X, Y] &= \sum_{i=1}^N \sum_{j=1}^N \left| \mathbf{E}[(p_i(x) - \mathbf{E}[p_i(x)])(p_j(y) - \mathbf{E}[p_j(y)])] \right| \\
&= \sum_{i=1}^N \sum_{j=1}^N \left| \mathbf{E}[p_i(x)p_j(y)] - \mathbf{E}[p_i(x)]\mathbf{E}[p_j(y)] \right| \\
&\geq \sum_{i=1}^N \sum_{j=1}^N |\gamma_{ij}| \left| \mathbf{E}[p_i(x)p_j(y)] - \mathbf{E}[p_i(x)]\mathbf{E}[p_j(y)] \right| \tag{3.36}
\end{aligned}$$

$$\geq \left| \sum_{i=1}^N \sum_{j=1}^N \gamma_{ij} (\mathbf{E}[p_i(x)p_j(y)] - \mathbf{E}[p_i(x)]\mathbf{E}[p_j(y)]) \right| \tag{3.37}$$

$$= \left| \rho[q_1(x), q_2(y)] \right|. \tag{3.38}$$

Equation 3.36 is obtained by multiplying each term with $|\gamma_{ij}|$. Equation 3.38 follows from definitions of q_1 , q_2 and the Pearson Correlation. The sufficiency of the set of basis functions is indicated by $|\rho[q_1(x), q_2(y)] - \rho[f_1^*(x), f_2^*(y)]| = \Delta$, where Δ is arbitrarily close to zero. This shows $\text{FBIC}[\mathcal{B}, X, Y] + \Delta \geq \rho_{\max}[x, y]$. By the universal approximation property of RBFs and polynomials, we can obtain a sufficient set of basis functions by increasing the number of basis functions. □

Theorem 2. *Given a sufficient set of basis functions, FBIC between tested variables is arbitrarily close to zero if and only if $X \perp\!\!\!\perp Y$.*

Proof. The sufficient condition of this theorem is trivial as independent variables always have 0 correlation no matter what basis functions are used for mapping. The positive error bound Δ reaches zero for independent variables. The necessary condition can be proved by using the upper bound property in Theorem 1. Since the maximal correlation is non-negative, it is arbitrarily close to zero if its upper bound is arbitrarily close to 0. □

Additionally, we can use properties of the Laplace transform to prove the validity of FBIC with Gaussian RBFs. Define a Borel probability measure $\mu : X \times Y \rightarrow \mathbb{R}^+$, where $\iint \mu(x, y) dx dy = 1$. We use $K(x) = e^{-\epsilon(x-c)^2}$ for the Gaussian RBFs. Define $K_s(x) = e^{-\epsilon(x-s)^2} = e^{-\epsilon(x^2-2xs+s^2)}$ and $K_t(y) = e^{-\epsilon(y-t)^2} = e^{-\epsilon(y^2-2yt+t^2)}$, where s and t are displacement parameters and $s, t \in [0, 1]$. Now we can establish a theorem that FBIC with Gaussian RBFs will equate the Borel probability measure of the joint probability distribution of x and y to the product of the marginal probability distributions of x and y if and only if x and y are independent.

Theorem 3. $\forall s, t \iint K_s(x)K_t(y)\mu(x, y) dx dy = \iint K_s(x)\mu(x, y) dx dy \iint K_t(y)\mu(x, y) dx dy$, if and only if $\mu(x, y) = \int \mu(x, s) ds \int \mu(y, t) dt$.

Proof. Let $\eta(x, y) = \mu(x, y) - \int \mu(x, s) ds \int \mu(y, t) dt$. We need to show $\forall s, t \iint K_s(x)K_t(y)\eta(x, y) dx dy = 0 \iff x \perp\!\!\!\perp y$. The necessary condition is trivial to prove as independent variables have the property that $\mu(x, y) = \int \mu(x, s) ds \int \mu(y, t) dt$. The sufficient condition is proved as follows. Assume $\forall s, t \iint K_s(x)K_t(y)\eta(x, y) dx dy = 0$. We have $\forall s, t \iint e^{\epsilon(2xs+2yt)} e^{-\epsilon(x^2+y^2)} \eta(x, y) dx dy = 0$. Let $\eta_1(x, y) = e^{-\epsilon(x^2+y^2)} \eta(x, y)$. This gives us $\forall s, t \iint e^{\epsilon(2xs+2yt)} \eta_1(x, y) dx dy = 0$. We can observe that this is exactly the Laplace transform of $\eta_1(x, y)$ so that it satisfies the condition that $\forall s, t [\mathcal{L}(\eta_1)](-2\epsilon s, -2\epsilon t) = 0 \iff \eta_1(x, y) = 0$. \square

3.3.4 Computational Complexity

The computational complexity of FBIC is linear with respect to the number of data points. The computation of the Pearson Correlation is $O(n)$, where n is the sample size. The dimensionality of tested variables is 2. Let the number of basis functions be k . We can express the computational complexity of FBIC as:

$$O(\mathbf{FBIC}) = O(k^2 n) \approx O(n). \quad (3.39)$$

3.3.5 FBIC vs FSIC

FBIC and FSIC differ in some significant aspects:

- FBIC is inspired by the HGR maximum correlation coefficient, whereas FSIC takes advantage of constrained covariance on the basis of MMD.
- FBIC can use many different RBFs and even orthogonal polynomials, whereas FSIC depends on characteristic kernels [151] like Gaussian kernels.
- FBIC has evenly spaced RBFs, whereas FSIC employs randomly spaced kernels.

Yet FBIC and FSIC are related when we examine their mathematical foundations. The HGR maximum correlation coefficient and the MMD criterion have possibly different function classes, optimize for different directions (one for maximal similarity, the other for maximal difference) and measure different statistical quantities. Nonetheless, the functions utilized in the MMD criterion are Borel-measurable with constrained variance in the Reproducing Kernel Hilbert Spaces. This implies that the class of functions for the MMD criterion is a subset of Borel-measurable functions that can be used for the HGR maximum correlation coefficient. Different optimization directions are more like a difference of optimization flavours leading to the same result: yielding zero if and only if the tested variables are independent. Both criteria measure covariance, though one is normalized (i.e., correlation) and the other is not normalized in the RKHSs.

Neither the HGR maximum correlation coefficient nor the MMD criterion is superior to the other in theory. Different independence criteria are preferable under different circumstances. In circumstances where training before using is not feasible, FBIC is preferable to FSIC. We will show how FBIC compares with FSIC in Section 3.4.

3.4 Experimental Studies

We use the classic ICA benchmark experiments put forward by [3]. The perfect demixing matrix V is known in advance and the optimized demixing matrix W can be evaluated by the Amari distance [1]:

$$d(V, W) = \frac{1}{2m(m-1)} \sum_{i=1}^m \left(\frac{\sum_{j=1}^m |a_{ij}|}{\max_j |a_{ij}|} - 1 \right) + \frac{1}{2m(m-1)} \sum_{j=1}^m \left(\frac{\sum_{i=1}^m |a_{ij}|}{\max_i |a_{ij}|} - 1 \right), \quad (3.40)$$

where $a_{ij} = (V^{-1}W)_{ij}$. This distance is ranged between 0 and 1. It is invariant to permutation and scaling. When $V = W$, the Amari distance between them is zero. In our experiments, the smaller the distance, the better the result.

We submitted our experiments to a grid computing computer cluster controlled by Sun Grid Engine [45] to run them in parallel. The CPU model was Intel(R) Core(TM) i7-8700 with 3.20GHz. There were 6 cores on each computer.

3.4.1 Simulated Data

To test the applicability of FBIC in different scenarios, source signals generated from a comprehensive set of probability density functions were used for ICA experiments. Both supergaussian and subgaussian distributions were covered. Mode and symmetry variation were also considered. All probability density functions had zero mean and unit variance. The details of each probability density function are demonstrated in Table 3.3.

In our experiment, two probability density functions were randomly chosen from the set. Signal samples $\mathbf{S} \in \mathbb{R}^{J \times M}$ were generated according to their probability density functions independently, where J is the number of sources and M is the sample length. They were then mixed by a

random mixing matrix $\mathbf{A} \in \mathbb{R}^{J \times J}$ with a bounded condition number between 1 and 2, which gave the observed signals $\mathbf{X} = \mathbf{A}\mathbf{S}$. The goal of the ICA experiment is to estimate the demixing matrix \mathbf{W} while only knowing that the original unmixed signals are statistically independent and they are linearly mixed.

As the source signals were generated randomly from random distributions, it was a difficult task to perform ICA algorithms on these signals. Unlike experiments on speech or image processing, we cannot take advantage of extra pattern information to separate the mixture of random signals. The successful performance of ICA algorithms in this dataset relied heavily on the performance measure used, which made this benchmark dataset desirable for evaluating different dependence measures.

Since the aim of our ICA experiments is to compare different independence criteria, it is unnecessary to test the robustness of different ICA algorithms when outliers are present in the observed mixture. In scenarios where noisy outliers occur, it is more appropriate to apply an outlier removal process before applying independence criterion. We evaluate different independence criteria through their performance on dependence detection only.

3.4.2 Preprocessing

We firstly prewhitened the observed signals to reduce the search space of the optimization process. Prewhitening is a popular BSS technique that eliminates the linear dependency between tested signals. It transformed the observed signals \mathbf{X} to have unit covariance matrix. By multiplying a whitening matrix \mathbf{Z} , we obtained the transformed signals $\tilde{\mathbf{X}} = \mathbf{Z}\mathbf{X}$ such that $\tilde{\mathbf{X}}\tilde{\mathbf{X}}^T = \mathbf{I}$. The whitening matrix \mathbf{Z} can be obtained by first performing a singular value decomposition to the mixing matrix and get $\mathbf{A} = \mathbf{U}\mathbf{D}\mathbf{Q}^T$ [47]. \mathbf{U} and \mathbf{Q} are orthonormal matrices and \mathbf{D} is a diagonal matrix containing singular values. The whitening matrix can be thus defined as

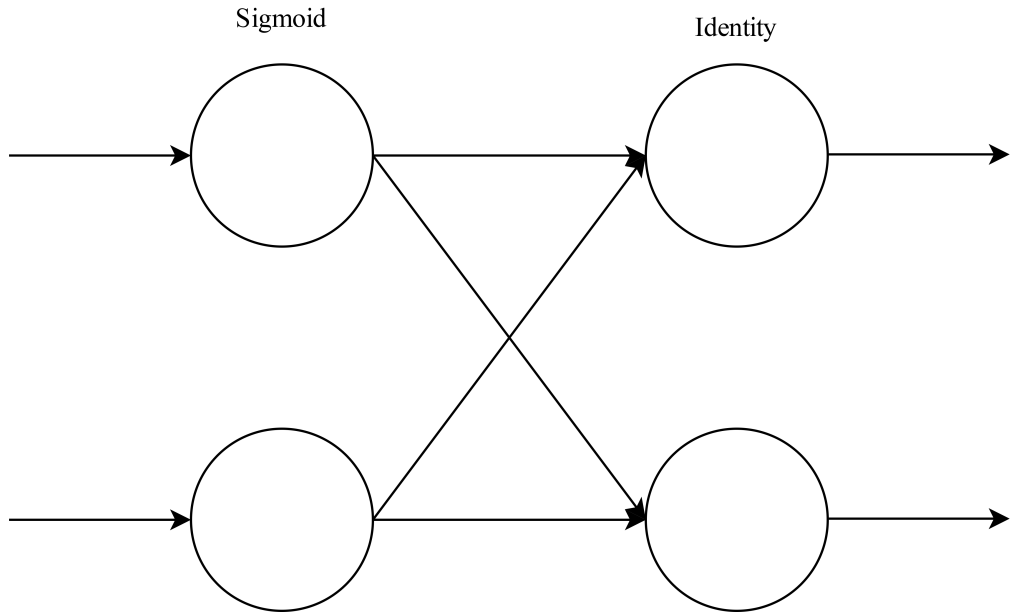


Figure 3.1: The two-layer neural network utilized for FBIC-based ICA tasks. The input layer has sigmoid activation. The output layer has identity activation.

$$\mathbf{Z} = \mathbf{D}^{-1/2}\mathbf{U}^T.$$

To make a fair comparison with the HSIC-based ICA experiments, we used the Jade algorithm [18] to initialize the first guess of the demixing matrix. This was also the initialization set up in the HSIC-based ICA algorithm [148].

3.4.3 Neural Network settings

A simple neural network as shown in Fig. 3.1 was utilized to optimize the demixing matrix. It consisted of two layers only: one input layer and one output layer. In practice, each neuron in the input layer was activated by a standard sigmoid function $\mathcal{S}(x) = \frac{1}{1+\exp(-x)}$, where x is the input signal for the neuron. The output layer had the identity activation function.

The number of neurons in the input layer and output layer was equal

to the number of original sources. The input signals were observed mixed signals. The output signals were supposed to be demixed signals without considering the scale or order. The weight matrix connecting the two layers thus played the role of the demixing matrix.

The cost function was $\mathcal{L} = \mathcal{F} + \mathcal{O}$, which was the sum of FBIC measurement between output signals and the orthogonality regularizer of the demixing matrix. The orthogonality regularizer was calculated by $\mathcal{O} = \text{sum}(|\mathbf{A}^T \mathbf{A}|) - \text{trace}(\mathbf{A}^T \mathbf{A})$, where $\text{sum}(\cdot)$ returned the total of all the entries in the matrix given. The role of \mathcal{O} was to ensure the demixing matrix would not introduce any linear dependency after prewhitening. An additional Pearson Correlation between tested variables x and y after sigmoid activation, $\rho[\mathcal{S}(x), \mathcal{S}(y)]$, was added to the cost function to aid the optimization.

The Adam optimizer was used to perform the gradient descent. The learning rate was set to 0.0001. The maximum epoch was 100000. If the training loss did not decrease after 1000 epochs, the training of the neural network would have an early stopping.

3.4.4 Parameter Choices for RBFs

The parameters of FBIC RBFs were selected by grid search. They were fixed regardless of the number of channels or the length of samples. For Gaussian RBFs, we used shape parameter 200 and the step parameter was increased by 0.1 stepwise from 0 to 0.9. For Laplace RBFs, we used shape parameter 20 and the step parameter was increased by 0.05 stepwise from 0 to 0.95. For Inverse Multiquadratic RBFs, we used shape parameter 900 and the step parameter was increased by 0.1 stepwise from 0 to 0.9. The results from the search of step size parameter is illustrated in Table 3.1. The results from the search of shape parameter is reported in Table 3.2.

The Shifted Legendre Polynomials did not require shape or step parameters. We used polynomial degrees from 2 to 20. Degree 0 and 1 were

Table 3.1: Average Amari distances of FBIC with different step parameters for RBFs. The tested data has 2 sources. The sample length is 250. The shape parameters are 200, 20, and 900 for Gaussian, Laplacian and IMQ RBFs respectively.

Basis \ Step	Gaussian	Laplacian	IMQ
0.1	6.15	7.28	7.20
0.05	8.30	6.43	9.68

Table 3.2: Average Amari distances of FBIC with different shape parameters for RBFs. The step parameter is 0.1. The tested data has 2 sources. The sample length is 250. Flat shape parameter is 1 for all basis functions. Sharp shape parameters are 200, 20, and 900 for Gaussian, Laplacian and IMQ RBFs respectively.

Basis \ Shape	Gaussian	Laplacian	IMQ
1	16.10	9.88	15.68
200;20;900	6.15	7.28	7.20

not chosen because they were either constant or identity mapping, which would not contribute much to reveal the nonlinear correlation between tested variables.

In FBIC, the quality of approximation does not always scale positively with the number of basis functions. [81] observed a similar phenomenon in FSIC as well. When there are not enough basis functions, increasing the number of basis functions will naturally improve the quality of approximation. However, too many redundant basis functions do not contribute to a better quality of approximation. It makes the upper bound of the maximal correlation coefficient from FBIC unnecessarily high. The experimental details are provided below.

Probability Density Functions for Signal Generation

Table 3.3: The probability density functions used for signal generation. The kurtosis of each probability density function is also presented. Degree of Freedom is denoted by DOF.

Probability Density Function	Kurtosis
Student, 3 DOF	∞
Double exponential	3.00
Uniform	-1.20
Student, 5 DOF	6.00
Exponential	6.00
2 double exponential	1.11
Symmetric 2 Gaussians, multimodal	-1.68
Symmetric 2 Gaussians, transmodal	-0.74
Symmetric 2 Gaussians, unimodal	-0.50
Asymmetric 2 Gaussians, multimodal	-0.53
Asymmetric 2 Gaussians, transmodal	-0.67
Asymmetric 2 Gaussians, unimodal	-0.47
Symmetric 4 Gaussians, multimodal	-0.82
Symmetric 4 Gaussians, transmodal	-0.62
Symmetric 4 Gaussians, unimodal	-0.80
Asymmetric 4 Gaussians, multimodal	-0.77
Asymmetric 4 Gaussians, transmodal	-0.29
Asymmetric 4 Gaussians, unimodal	-0.67

Number of Basis Functions

To illustrate how the number of basis functions can affect the quality of approximation, 100 experiments were performed on two-channel mixtures

Table 3.4: Average Amari distances (mean) and standard deviation (std) of FBIC with different number of Gaussian RBFs. The tested data has 2 sources. The sample length is 250. The shape parameter is 200.

Statistics \ Number of Basis	5	10	15	20
mean	8.76	6.15	6.15	8.30
std	10.42	7.31	6.04	7.22

of randomly selected distributions. Mixtures had length 250. We fixed Gaussian RBFs with shape parameter 200 and varied the number of basis functions only. We set the number of basis functions to be 5, 10, 15 and 20. The Amari distances resulting from the selected number of basis functions were 8.77, 6.20, 5.92 and 8.34 respectively. When the number of basis functions increased from 5 to 10 then to 15, the quality of approximation indicated by the Amari distance improved alongside. However, when the number of basis functions further increased to 20, the quality of approximation started to degrade. The results are reported in Table 3.4.

RBFs vs Shifted Legendre Polynomial Basis Functions

Legendre polynomials have a fixed region of support whereas RBFs utilized in FBIC have infinite support. Initially we thought that the approximation quality of Legendre polynomials would be better than those of RBFs when applied to variables with finite support. However, the experimental results for data generated from uniform distributions favored RBFs. Therefore, pinpointing the scenario in which Legendre polynomials in FBIC can work best remains an open problem.

3.4.5 Multi-Channel Extension of FBIC

By the definition of the maximal correlation, it is natural to apply FBIC to two random variables. For dependence detection amongst multiple random variables, a simple extension of FBIC is to calculate all the pairwise FBIC scores between variables and sum them up. Although limiting FBIC to pairwise correlation is suboptimal as multivariate dependence may not be detected, we still found favorable results for multi-channel ICA experiments as is shown in Table 3.5.

3.4.6 Results and Discussions

Table 3.5: The Amari distance of demixed signals from n sources based on different independence measures. The sample length is m . Rep. represents the number of experiment replications. The Gaussian RBFs in FBIC are denoted by g. The Laplace RBFs in FBIC are denoted by l. The Inverse Multiquadratic RBFs are denoted by imq. The Shifted Legendre Polynomials are denoted by lp.

n	m	Rep.	FBIC _g	FBIC _l	FBIC _{imq}	FBIC _{lp}	FKICA	NFSIC	FICA	Jade
2	250	1000	5.8	5.7	6.4	6.6	6.3	6.5	12.3	9.1
2	1000	1000	2.4	2.1	2.7	2.5	2.8	2.5	6.2	4.3
4	1000	100	3.4	3.1	3.7	3.8	3.3	3.5	6.7	5.1
4	4000	100	1.7	1.5	1.8	1.8	1.5	4.6	3.2	2.7

As HSIC exhibited superior performance over other dependence measures in the classic ICA benchmark dataset [55, 148], we compared the performance of FBIC mainly with FastKICA [148], a fast HSIC-based Kernel ICA based on the incomplete Cholesky decomposition. Its kernel width was set to 0.5 as suggested by the original authors. Its maximum iteration number was set to 20 and the convergence threshold was set to 1e-6. Results from FastICA [75] and Jade [18] algorithms were also included.

In Table 3.5, we use FKICA to denote FastKICA and FICA to denote FastICA. To compare FBIC and FSIC directly, we implemented a novel ICA algorithm based on Normalized FSIC, which is denoted NFSIC in the table.

NFSIC is a novel FSIC-based ICA algorithm implemented to compare with its FBIC counterpart. The neural network used for the demixing matrix estimation shared the same architecture with that of the FBIC-based algorithm. The difference was that the neural network cost function was replaced with the $\widehat{\text{NFSIC}}^2$ statistic proposed in [81]. As there was no training stage in our ICA experiments, test locations for NFSIC were randomly chosen from Gaussian distributions with mean and variance corresponding to the signal samples. The number of test locations were set to 10, 50 or 100. For 2-channel signal mixtures with sample length 250, the best results were achieved when there were 50 test locations. For 2-channel signal mixtures with sample length 1000 and 4-channel signal mixtures with sample length 1000, the best results were achieved when there were 100 test locations. For 4-channel signal mixtures with sample length 4000, the best results were achieved when there were 10 test locations.

From Table 3.5 we can observe that FBIC with Laplacian RBFs performed the best in all the experiments. This is consistent with the finding that the Laplacian kernel in HSIC performed better than the Gaussian kernel [55]. FBIC with other basis functions was also better than FKICA in two-channel experiments. For four-channel experiments, the performance of FBIC with Laplace RBFs was no worse than FKICA, while the performance of FBIC with other basis functions were acceptable. FBIC with Inverse Multiquadratic RBFs and Shifted Legendre Polynomials performed less well than Laplace and Gaussian RBFs. In all experiments, the performance of both FBIC-based and HSIC-based algorithms surpass those of FICA and Jade by a large margin. The FSIC-based algorithm performed well in all but the four-channel experiments with long sequences. This can be explained by the absence of optimization of test locations. The devia-

tion between random and optimal test locations becomes larger when the signals are longer.

A smaller step parameter increment was beneficial for FBIC with Laplacian RBFs, but FBIC with other RBFs did not benefit from this. One explanation is that the shape parameter we selected for other RBFs may not be well suited to more fine-grained approximation. Another possibility is that the sharp peak of Laplace RBFs makes them more suited to a smaller step size. More experiments may shed light on the relationship between the targeted distributions and the best FBIC parameter settings.

We also discovered that all the shape parameters selected for the three sets of RBFs were relatively large. This indicates that sharper RBFs are more suitable for approximating best mapping functions $f_1^*(\cdot)$ and $f_2^*(\cdot)$ of the HGR maximum correlation coefficient. The justification is that $f_1^*(\cdot)$ and $f_2^*(\cdot)$ tend to be functions that magnify areas where two probability density functions of the tested variables differ the most. The magnification can be accomplished by assigning a sharp peak to the mapping function around the area to be magnified. The sharper RBFs therefore are better candidates for $f_1^*(\cdot)$ and $f_2^*(\cdot)$ approximation.

Parameter selection has always been a challenge for using RBFs or kernels. In HSIC, scale parameters for kernels have to be decided. In FSIC, scale parameters as well as test locations require careful tuning. Regarding FBIC, it is also vital to select the right shape parameters for RBFs. Since FBIC with Shifted Legendre Polynomials could perform well without tuning parameters, it can be used as a FBIC baseline. The FBIC algorithms using RBFs should perform at least as well as the FBIC baseline.

To ascertain the complexity advantage of FBIC, we undertook a comparative analysis of the computational efficiency between FBIC and HSICICA. Our approach involved configuring HSICICA with identical neural network settings as FBIC, with the sole distinction being the substitution of the loss function with the HSIC value. This alignment ensured that both algorithms operated within the same neural network framework, utilizing

an identical gradient descent optimization mechanism, thereby promoting a fair comparison of computational times. Simulations were executed on signal mixtures of length 1000, originating from two random sources. Each algorithm underwent 100 trials, conducted on a Linux workstation equipped with 20-core CPUs featuring a 12th Gen Intel(R) Core(TM) i7-12700 model. The recorded wall time for FBIC was 7621 seconds, while HSICICA registered a significantly higher wall time of 84559 seconds. Notably, the wall time of HSICICA exceeded that of FBIC by more than 10 times in the context of identical ICA tasks. This contrast underscores the pronounced advantage of the linear computational complexity exhibited by FBIC.

3.5 Conclusions

In this chapter, we address the signal separation aspect of signal enhancement by investigating independence criterion. We have proposed the Finite Basis Independence Criterion, a linear-time independence measurement that can be optimized through gradient descent. By approximating the best mapping function with a finite set of basis functions, FBIC establishes an upper bound to the Hirschfeld-Gebelein-Rényi maximum correlation coefficient. The ICA algorithm based on FBIC outperforms the analogous ICA algorithm based on the state-of-the-art kernel independence measurements HSIC and FSIC in two-channel experiments. For four-channel experiments, FBIC-based ICA can still perform competitively against FKICA when the Laplace RBFs are utilized, though only pairwise correlations are calculated.

Acknowledgments

We thank Hung Pham and Richard Arnold for help with proofs. We thank Yuan Yao for helpful discussions.

Chapter 4

Robustness Analysis of First-Order Linear Differential Microphone Arrays

In the previous chapter, we focus on signal enhancement tasks involving signal separation. In transition, the present chapter redirects our attention towards another pivotal avenue of signal enhancement: fixed beamforming. Our exploration commences with an in-depth analysis of the robustness of first-order microphone arrays in the context of fixed beamforming. First-order Linear Differential Microphone Arrays (LDMAs) are sensitive to sensor imperfections such as phase errors. This chapter analyses the impacts of both bounded and unbounded phase errors on first-order LD-MAs. We propose a tolerance threshold that allows bounded phase errors to take various values. Moreover, White Noise Gain (WNG) thresholds for preventing mainlobe misorientation are obtained. Our work provides guidance for the design of robust first-order LD-MAs.

4.1 Introduction

Microphone arrays are indispensable components of many hands-free communication systems and speech recognition systems in adverse environments [39, 61, 129, 101, 80]. Recently, LDMAAs have attracted a significant amount of interest, since they possess several advantages over traditional methods. Firstly, they can construct relatively frequency-invariant beam-patterns, and hence are appropriate for speech signal processing. Secondly, they facilitate large Directivity Factors (DFs) with small and compact apertures [6, 9].

It is well known that LDMAAs, especially those of high order, suffer from white noise amplification and struggle to have high WNG values [34, 177]. As a result, LDMAAs are sensitive to sensor imperfections that degrade robustness and reduce WNG values [37, 16]. First-order LDMAAs are commonly used to mitigate the influence of sensor imperfections.

Many works have investigated how sensor imperfections affect first-order LDMAAs [157, 156, 24]. In [157], DF and Front-to-Back Ratio (FBR) lower bounds are optimised with respect to sensor imperfections, but WNG optimisation is lacking. Recent works [156, 24] show that sensor phase errors have a critical influence on the mainlobe orientation of first-order LDMAAs pointing towards the endfire direction. However, the tolerance of phase errors claimed in [156, 24] does not reflect practical scenarios by assuming that all microphones have nearly identical values of bounded phase errors, which are close to 0. Moreover, there is a necessity to investigate unbounded phase errors, i.e., errors that can be arbitrarily large. Although they have been overlooked so far, unbounded phase errors naturally arise in scenarios like wireless acoustic sensor networks where device synchronisation is challenging [4, 42, 27, 43].

In this work, we propose a tolerance threshold for bounded phase errors without the assumption that microphones should have similar phase errors. We also derive WNG thresholds for preventing mainlobe misori-

entation due to bounded and unbounded phase errors.

4.2 Background

4.2.1 Signal Model

Consider a uniform linear array of M omnidirectional microphones with inter-microphone spacing δ . The steering vector of this array is defined as [160]

$$\mathbf{d}(\omega, \cos \theta) = [1 \ e^{-j\omega\tau_0 \cos \theta} \ \dots \ e^{-j(M-1)\omega\tau_0 \cos \theta}]^T, \quad (4.1)$$

where $\omega = 2\pi f$ is the angular frequency and f is the temporal frequency, θ is the direction of arrival of the source signal from the array axis, j is $\sqrt{-1}$, c is the speed of sound in air and $\tau_0 = \delta/c$.

Beampattern characterizes the input-output behaviour of microphone arrays in beamforming [8]. It is defined as

$$\mathcal{B}_M(\omega, \theta) = [\mathbf{d}(\omega, \cos \theta)]^H \mathbf{h}(\omega) \quad (4.2)$$

$$= \sum_{m=1}^M H_m(\omega) e^{j(m-1)\omega\tau_0 \cos \theta} \quad (4.3)$$

where $\mathbf{h}(\omega) = [H_1(\omega), H_2(\omega), \dots, H_M(\omega)]^T$ is composed of the filter coefficients. With distortionless constraint, $\mathcal{B}_M[\omega, \theta]$ has the property that

$$\mathcal{B}_M(\omega, \theta) \begin{cases} = 1, & \theta = \theta_d \\ < 1, & \theta \neq \theta_d \end{cases}, \quad (4.4)$$

where θ_d is the desired look direction of the beamformer.

4.2.2 Metrics of First-Order LDMA

By approximating the exponential term in (4.3) with Taylor series, we obtain $\mathcal{B}_{M,1}(\theta)$, the beampattern of the first-order LDMA with angle θ :

$$\mathcal{B}_{M,1}(\theta) \approx \sum_{m=1}^M H_m(\omega) \sum_{n=0}^1 \frac{1}{n!} [j(m-1)\omega\tau_0 \cos \theta]^n \quad (4.5)$$

$$= \sum_{m=1}^M H_m(\omega) + j\omega\tau_0 \cos \theta \sum_{m=1}^M (m-1)H_m(\omega) \quad (4.6)$$

$$= a_{1,0} + a_{1,1} \cos \theta. \quad (4.7)$$

where $a_{1,0}$ and $a_{1,1}$ are the real coefficients of $\mathcal{B}_{M,1}(\theta)$.

From (4.6) and (4.7), we can obtain the values for $H_m(\omega)$ by following the least-norm principle described in section 2.4.1:

$$H_m(\omega) = \frac{6(m-1)a_{1,1}}{j\omega\tau_0 M(M-1)(2M-1)}, \quad m = 2, 3, \dots, M, \quad (4.8)$$

and

$$H_1(\omega) = a_{1,0} - \sum_{m=2}^M H_m(\omega) = a_{1,0} - \frac{3a_{1,1}}{j\omega\tau_0(2M-1)}. \quad (4.9)$$

The mainlobe orientation θ_{main} is defined as

$$|\mathcal{B}_{M,1}(\theta_{\text{main}})|^2 = \max_{\theta} |\mathcal{B}_{M,1}(\theta)|^2. \quad (4.10)$$

Generally, $\theta_{\text{main}} = \theta_d$ and $|\mathcal{B}_{M,1}(\theta_{\text{main}})|^2 = 1$.

One common metric to measure the robustness of microphone arrays is by using WNG [46], which is defined as

$$\text{WNG}[\mathbf{h}(\omega)] = \frac{|\mathcal{B}_{M,1}(\theta_d)|^2}{[\mathbf{h}(\omega)]^H \mathbf{h}(\omega)}. \quad (4.11)$$

Another commonly used metric is DF:

$$\text{DF}[\mathbf{h}(\omega)] = \frac{|\mathcal{B}_{M,1}(\theta_d)|^2}{\frac{1}{2} \int_0^\pi |\mathcal{B}_{M,1}(\theta)|^2 \sin \theta d\theta}. \quad (4.12)$$

We assume that the source signal is from the endfire direction, i.e., $\theta_d = 0^\circ$. This implies that (4.7) can be rewritten as $a_{1,0} + a_{1,1} = 1$. We also assume $\delta \ll \lambda$, which means the spacing between microphones should be much smaller than the wavelength. We consider the source signal to be far-field. Reverberation is not included in this work.

4.3 Analysis of Gain Errors

In this section, we investigate whether gain errors have impacts on the mainlobe orientation of first-order LDMA. The steering vector with gain errors can be expressed as

$$\mathbf{d}^{(g)}(\omega, \cos \theta) = [\eta_1(\omega) \ \eta_2(\omega)e^{-j\omega\tau_0 \cos \theta} \ \dots \ \eta_M(\omega)e^{-j(M-1)\omega\tau_0 \cos \theta}]^T, \quad (4.13)$$

where $\eta_m(\omega)$ is the actual gain applied to the m th microphone at the frequency of ω . If the m th microphone has no gain error at the frequency of ω , $\eta_m(\omega) = 1$. We assume $|\eta_m(\omega) - 1| \leq \epsilon_g$, where ϵ_g is the non-negative gain error bound.

From (4.13), we can derive the beampattern of the first-order LDMA with gain errors as

$$\mathcal{B}_{M,1}^{(g)}(\theta) = [\mathbf{d}^{(g)}(\omega, \cos \theta)]^H \mathbf{h}(\omega) \quad (4.14)$$

$$= \eta_1(\omega)H_1(\omega) + \sum_{m=2}^M \eta_m(\omega)H_m(\omega)e^{j(m-1)\omega\tau_0 \cos \theta} \quad (4.15)$$

$$\approx a_{1,0}\eta_1(\omega) + \frac{6a_{1,1} \cos \theta \sum_{m=2}^M (m-1)^2 \eta_m(\omega)}{M(M-1)(2M-1)} - \frac{3a_{1,1}}{j\omega\tau_0(2M-1)} \left[\eta_1(\omega) - \frac{2 \sum_{m=2}^M (m-1)\eta_m(\omega)}{M(M-1)} \right] \quad (4.16)$$

The beampattern coefficients distorted by phase errors can be derived

from (4.16), and are

$$a_{1,0}^{(g)} = a_{1,0}\eta_1(\omega) - \frac{3a_{1,1}}{j\omega\tau_0(2M-1)} \left[\eta_1(\omega) - \frac{2\sum_{m=2}^M(m-1)\eta_m(\omega)}{M(M-1)} \right], \quad (4.17)$$

and

$$a_{1,1}^{(g)} = \frac{6a_{1,1}\sum_{m=2}^M(m-1)^2\eta_m(\omega)}{M(M-1)(2M-1)}. \quad (4.18)$$

By taking the derivative of $|\mathcal{B}_{M,1}^{(g)}(\theta)|^2$ with respect to θ , we obtain

$$\frac{d|\mathcal{B}_{M,1}^{(g)}(\theta)|^2}{d\theta} = 2\mathcal{B}_{M,1}^{(g)}(\theta) \left[\frac{d\mathcal{B}_{M,1}^{(g)}(\theta)}{d\theta} \right]^H \quad (4.19)$$

$$= -2\sin\theta a_{1,1}^{(g)} \mathcal{B}_{M,1}^{(g)}(\theta). \quad (4.20)$$

(4.20) shows that $\frac{d|\mathcal{B}_{M,1}^{(g)}(\theta)|^2}{d\theta}$ has extrema when $\sin\theta = 0$ or when $\mathcal{B}_{M,1}^{(g)}(\theta) = 0$. It is obvious that $\mathcal{B}_{M,1}^{(g)}(\theta) = 0$ implies minima. Since θ_{main} is related to the maxima, we only need to consider $\sin\theta = 0$ for mainlobe misorientation. In other words, if $|\mathcal{B}_{M,1}^{(g)}(0^\circ)|^2 \geq |\mathcal{B}_{M,1}^{(g)}(180^\circ)|^2$, the mainlobe misorientation is avoided. We have

$$\begin{aligned} & |\mathcal{B}_{M,1}^{(g)}(0^\circ)|^2 - |\mathcal{B}_{M,1}^{(g)}(180^\circ)|^2 \\ &= 2(a_{1,0}^{(g)}[a_{1,1}^{(g)}]^H + a_{1,1}^{(g)}[a_{1,0}^{(g)}]^H) \end{aligned} \quad (4.21)$$

$$= \frac{24a_{1,0}a_{1,1}\eta_1(\omega)}{M(M-1)(2M-1)} \sum_{m=2}^M (m-1)^2 \eta_m(\omega). \quad (4.22)$$

As (4.22) is always non-negative, gain errors will not cause mainlobe misorientation in first-order LDMA with designed endfire mainlobe. This conclusion is not affected by the array aperture, number of microphones or the beampattern coefficients of LDMA.

4.4 Analysis of Phase Errors

The steering vector with phase errors can be expressed as

$$\mathbf{d}^{(p)}(\omega, \cos \theta) = [e^{-j\psi_1(\omega)} e^{-j\omega\tau_0 \cos \theta - j\psi_2(\omega)} \dots e^{-j(M-1)\omega\tau_0 \cos \theta - j\psi_M(\omega)}]^T, \quad (4.23)$$

where $\psi_m(\omega)$ is the phase error of the m th microphone at the frequency of ω .

Bounded phase errors generally appear in Analogue-to-Digital Converters (ADCs) used for microphone arrays. They are analysed in detail in Section 4.4.1. Large phase errors that are unbounded do occur in scenarios like wireless acoustic sensor networks. They are discussed in Section 4.4.2.

4.4.1 Analysis of Bounded Phase Errors

We assume $|\psi_m(\omega)| \leq \epsilon_p$, where ϵ_p is the non-negative phase error bound close to 0. From (4.23), we can utilize Taylor approximation to derive the beampattern of the first-order LDMA with phase errors as

$$\mathcal{B}_{M,1}^{(p)}(\theta) = [\mathbf{d}^{(p)}(\omega, \cos \theta)]^H \mathbf{h}(\omega) \quad (4.24)$$

$$= H_1(\omega) e^{j\psi_1(\omega)} + \sum_{m=2}^M H_m(\omega) e^{j(m-1)\omega\tau_0 \cos \theta + j\psi_m(\omega)} \quad (4.25)$$

$$\approx H_1(\omega)(1 + j\psi_1(\omega)) + \sum_{m=2}^M H_m(\omega)(1 + j(m-1)\omega\tau_0 \cos \theta + j\psi_m(\omega)) \quad (4.26)$$

$$\approx a_{1,0} + a_{1,1} \cos \theta + ja_{1,0}\psi_1(\omega) - \frac{3a_{1,1}}{\omega\tau_0(2M-1)} \times \left[\psi_1(\omega) - \frac{2 \sum_{m=2}^M (m-1)\psi_m(\omega)}{M(M-1)} \right]. \quad (4.27)$$

From (4.27), the beampattern coefficients distorted by phase errors are

$$a_{1,0}^{(p)} = a_{1,0} + ja_{1,0}\psi_1(\omega) - \frac{3a_{1,1}}{\omega\tau_0(2M-1)} \times \left[\psi_1(\omega) - \frac{2\sum_{m=2}^M(m-1)\psi_m(\omega)}{M(M-1)} \right], \quad (4.28)$$

and $a_{1,1}^{(p)} = a_{1,1}$. To investigate whether phase errors will affect θ_{main} , we take the derivative of $|\mathcal{B}_{M,1}^{(p)}(\theta)|^2$ with respect to θ :

$$\frac{d|\mathcal{B}_{M,1}^{(p)}(\theta)|^2}{d\theta} = -2a_{1,1}^{(p)} \sin\theta \mathcal{B}_{M,1}^{(p)}(\theta). \quad (4.29)$$

This shows that $\frac{d|\mathcal{B}_{M,1}^{(p)}(\theta)|^2}{d\theta}$ has extrema when $\sin\theta = 0$ or $\mathcal{B}_{M,1}^{(p)}(\theta) = 0$. It is obvious that $\mathcal{B}_{M,1}^{(p)}(\theta) = 0$ implies minima. Since θ_{main} is related to the maxima, we only need to consider $\sin\theta = 0$, where $\theta = 0^\circ$ or 180° . If $\theta_{\text{main}} = 0^\circ$, phase errors have no effect on θ_{main} . Otherwise, mainlobe misorientation happens, i.e., $\theta_{\text{main}} \neq \theta_d$.

Mainlobe misorientation can severely degrade the performance of LD-MAs [24]. By definition, the condition to avoid mainlobe misorientation caused by phase errors is $|\mathcal{B}_{M,1}^{(p)}(0^\circ)|^2 \geq |\mathcal{B}_{M,1}^{(p)}(180^\circ)|^2$. We first examine

$$\begin{aligned} & |\mathcal{B}_{M,1}^{(p)}(0^\circ)|^2 - |\mathcal{B}_{M,1}^{(p)}(180^\circ)|^2 \\ &= 4a_{1,1} \left(a_{1,0} + \frac{-6\Phi_T}{\omega\tau_0 M(M-1)(2M-1)} a_{1,1} \right), \end{aligned} \quad (4.30)$$

where

$$\Phi_T = \sum_{m=2}^M (m-1)(\psi_1(\omega) - \psi_m(\omega)). \quad (4.31)$$

To satisfy $|\mathcal{B}_{M,1}^{(p)}(0^\circ)|^2 - |\mathcal{B}_{M,1}^{(p)}(180^\circ)|^2 \geq 0$, we get $\Phi_T \leq \zeta$, where ζ is the tolerance threshold for phase errors:

$$\zeta = \frac{M(M-1)(2M-1)\omega\tau_0 a_{1,0}}{6(1-a_{1,0})}. \quad (4.32)$$

(4.32) clearly shows that phase errors can cause mainlobe misorientation when $\Phi_T > \zeta$. To keep the mainlobe orientation at 0° , Φ_T should be no larger than ζ . By examining the numerator elements of ζ , we can find four robustness boosting factors. Firstly, M suggests that more microphones can boost the robustness of first-order LDMA. Secondly, $\omega = 2\pi f$ suggests that first-order LDMA are more robust at higher frequency bands. Thirdly, $\tau_0 = \delta/c_0$ suggests that larger microphone spacing helps with array robustness. Lastly, $a_{1,0}$ suggests the choice of beampattern coefficients plays a role in array robustness.

In particular, we can observe from (4.32) that the larger $a_{1,0}$ is, the larger ζ is. As $a_{1,0}$ is the largest in cardioid amongst all classical designs, it implies that cardioid is the most robust design of first-order LDMA.

Because $|\psi_m(\omega)| \leq \epsilon_p$, the maximum of $(\psi_1(\omega) - \psi_m(\omega))$ is $2\epsilon_p$. Substituting $(\psi_1(\omega) - \psi_m(\omega)) = 2\epsilon_p$ into (4.31), we derive $\Phi_{Tmax} = M(M-1)\epsilon_p$. To have $\Phi_{Tmax} \leq \zeta$, we derive

$$\epsilon_p \leq \frac{(2M-1)\omega\tau_0 a_{1,0}}{6(1-a_{1,0})}. \quad (4.33)$$

(4.31) suggests that the phase delay of the first microphone, i.e., the microphone closest to the source signal, plays a crucial role in determining the value of Φ_T .

Based on (4.11), we can further derive the WNG formula with the presence of phase errors as

$$\text{WNG}[\mathbf{h}(\omega)] = \frac{|\mathcal{B}_{M,1}^{(p)}(\theta_d)|^2}{[\mathbf{h}(\omega)]^H \mathbf{h}(\omega)}. \quad (4.34)$$

The value of $|\mathcal{B}_{M,1}^{(p)}(\theta_d)|^2$, from (4.27) and (4.31), is:

$$|\mathcal{B}_{M,1}^{(p)}(\theta_d)|^2 = \left[a_{1,0} + a_{1,1} \cos \theta_d - \frac{a_{1,1}}{\omega\tau_0} \times \frac{6\Phi_T}{M(M-1)(2M-1)} \right]^2 + [a_{1,0}\psi_1(\omega)]^2. \quad (4.35)$$

Applying $\Phi_T \leq \zeta$ and $\theta_d = 0^\circ$ from (4.34), we obtain

$$\text{WNG}[\mathbf{h}(\omega)] \geq \frac{a_{1,1}^2 + a_{1,0}^2 \psi_1(\omega)^2}{[\mathbf{h}(\omega)]^H \mathbf{h}(\omega)}. \quad (4.36)$$

By letting $\psi_1(\omega) = \epsilon_p$, we can get

$$\text{WNG}_T[\mathbf{h}(\omega)] = \frac{a_{1,1}^2 + a_{1,0}^2 \epsilon_p^2}{[\mathbf{h}(\omega)]^H \mathbf{h}(\omega)}. \quad (4.37)$$

(4.37) offers a practical robustness threshold of first-order LDMA. As long as the tested WNG value of a first-order LDMA is higher than $\text{WNG}_T[\mathbf{h}(\omega)]$, it will not suffer from mainlobe misorientation in the presence of ϵ_p -bounded phase errors.

4.4.2 Analysis of Unbounded Phase Errors

For unbounded phase errors p' , we can rewrite (4.24) without approximating phase delay terms, which becomes

$$\begin{aligned} & \mathcal{B}_{M,1}^{(p')}(\theta) \\ &= (a_{1,0} - \frac{3a_{1,1}}{j\omega\tau_0(2M-1)})e^{j\psi_1} + \frac{\sum_{m=2}^M 6(m-1)a_{1,1}}{j\omega\tau_0 M(M-1)(2M-1)} \\ & \times [1 + j(m-1)\omega\tau_0 \cos \theta]e^{j\psi_m} \end{aligned} \quad (4.38)$$

$$\begin{aligned} &= a_{1,0}e^{j\psi_1} - \frac{3a_{1,1}e^{j\psi_1}}{j\omega\tau_0(2M-1)} + \frac{3a_{1,1}}{\omega\tau_0(2M-1)} \left[\frac{2\sum_{m=2}^M (m-1)e^{j\psi_m}}{jM(M-1)} + \right. \\ & \left. \frac{2\sum_{m=2}^M (m-1)^2\omega\tau_0 \cos \theta e^{j\psi_m}}{M(M-1)} \right] \end{aligned} \quad (4.39)$$

$$\begin{aligned} &= a_{1,0}e^{j\psi_1} + \frac{3a_{1,1}}{\omega\tau_0(2M-1)} \left[\frac{2\sum_{m=2}^M (m-1)e^{j\psi_m}}{jM(M-1)} + je^{j\psi_1} \right] \\ &+ \frac{6a_{1,1}\sum_{m=2}^M (m-1)^2 e^{j\psi_m} \cos \theta}{M(M-1)(2M-1)} \end{aligned} \quad (4.40)$$

$$\begin{aligned} &= a_{1,0} \cos \psi_1 + \frac{3a_{1,1}}{\omega\tau_0(2M-1)} \left[\frac{2\sum_{m=2}^M (m-1) \sin \psi_m}{M(M-1)} - \sin \psi_1 \right] \\ &+ \frac{6a_{1,1}\sum_{m=2}^M (m-1)^2 \cos \psi_m \cos \theta}{M(M-1)(2M-1)} + ja_{1,0} \sin \psi_1 \\ &+ \frac{3a_{1,1}}{\omega\tau_0(2M-1)} \left[\frac{2\sum_{m=2}^M (m-1) \cos \psi_m}{jM(M-1)} + j \cos \psi_1 \right] \\ &+ \frac{j6a_{1,1}\sum_{m=2}^M (m-1)^2 \sin \psi_m \cos \theta}{M(M-1)(2M-1)}. \end{aligned} \quad (4.41)$$

By combining (4.29) and (4.40), we obtain the derivative of $|\mathcal{B}_{M,1}^{(p')}(\theta)|^2$ with respect to θ :

$$\frac{d|\mathcal{B}_{M,1}^{(p')}(\theta)|^2}{d\theta} = \frac{-12a_{1,1}\sum_{m=2}^M (m-1)^2 e^{j\psi_m}}{M(M-1)(2M-1)} \mathcal{B}_{M,1}^{(p')}(\theta) \sin \theta. \quad (4.42)$$

Similar to the analysis of (4.29), from (4.42) we observe that we only need to consider $|\mathcal{B}_{M,1}^{(p')}(0^\circ)|^2 \geq |\mathcal{B}_{M,1}^{(p')}(180^\circ)|^2$ to avoid mainlobe misorientation.

The difference $\mathcal{D} = |\mathcal{B}_{M,1}^{(p')}(0^\circ)|^2 - |\mathcal{B}_{M,1}^{(p')}(180^\circ)|^2$ can be derived from (4.40):

$$\begin{aligned} \mathcal{D} &= \frac{24a_{1,0}a_{1,1} \sum_{m=2}^M (m-1)^2 \cos(\psi_1 - \psi_m)}{M(M-1)(2M-1)} - \\ &\frac{72a_{1,1}^2 \sum_{m=2}^M (m-1)^2 \sin(\psi_1 - \psi_m)}{\omega\tau_0 M(M-1)(2M-1)^2} - \\ &\frac{144a_{1,1}^2 \sum_{m_1=2}^M \sum_{m_2=2}^M (m_1-1)(m_2-1)^2 \sin(\psi_{m_2} - \psi_{m_1})}{\omega\tau_0 M^2(M-1)^2(2M-1)^2}. \end{aligned} \quad (4.43)$$

Unbounded phase errors can also cause mainlobe misorientation if $\mathcal{D} < 0$. We can expand $|\mathcal{B}_{M,1}^{(p')}(0^\circ)|^2$, which is

$$\begin{aligned} &|\mathcal{B}_{M,1}^{(p')}(0^\circ)|^2 \\ &= \text{Re}\{\mathcal{B}_{M,1}^{(p')}(0^\circ)\}^2 + \text{Im}\{\mathcal{B}_{M,1}^{(p')}(0^\circ)\}^2 \\ &= a_{1,0}^2 + \frac{9a_{1,1}^2}{\omega^2\tau_0^2(2M-1)^2} + \frac{12a_{1,0}a_{1,1} \sum_{m=2}^M (m-1) \sin(\psi_m - \psi_1)}{\omega\tau_0 M(M-1)(2M-1)} \\ &+ \frac{36a_{1,1}^2 \sum_{m_1=2}^M \sum_{m_2=2}^M (m_1-1)(m_2-1) \cos(\psi_{m_1} - \psi_{m_2})}{\omega^2\tau_0^2 M^2(M-1)^2(2M-1)^2} \\ &- \frac{36a_{1,1}^2 \sum_{m=2}^M (m-1) \cos(\psi_m - \psi_1)}{\omega^2\tau_0^2 M(M-1)(2M-1)^2} \\ &+ \frac{36a_{1,1}^2 \sum_{m_1=2}^M \sum_{m_2=2}^M (m_1-1)^2(m_2-1)^2 \cos(\psi_{m_1} - \psi_{m_2})}{M^2(M-1)^2(2M-1)^2} \\ &+ \frac{1}{2}(|\mathcal{B}_{M,1}^{(p')}(0^\circ)|^2 - |\mathcal{B}_{M,1}^{(p')}(180^\circ)|^2). \end{aligned} \quad (4.44)$$

In (4.44), phase delays are not bounded by ϵ_p . We assume that phase delays can take extremely large values equivalent to hundreds of milliseconds. This happens when the time clocks are not synchronized.

Denote $|\mathcal{B}_{M,1}^{(p')}(0^\circ)|_{\max}^2$ as the maximal value of $|\mathcal{B}_{M,1}^{(p')}(0^\circ)|^2$ when ψ_m varies. Define $\psi_T = \psi_{m'} - \psi_1$ to be the theoretical phase difference that yields $|\mathcal{B}_{M,1}^{(p')}(0^\circ)|_{\max}^2$, where $m' = 2, 3, \dots, M$. To obtain $|\mathcal{B}_{M,1}^{(p')}(0^\circ)|_{\max}^2$, we can assume that $\psi_{m_1} = \psi_{m_2}$ as the maximum value of a cosine function is reached

at value 0. Next, we can derive the maximum value of

$$\frac{12a_{1,0}a_{1,1} \sum_{m=2}^M (m-1) \sin(\psi_m - \psi_1)}{\omega\tau_0 M(M-1)(2M-1)} - \frac{36a_{1,1}^2 \sum_{m=2}^M (m-1) \cos(\psi_m - \psi_1)}{\omega^2\tau_0^2 M(M-1)(2M-1)^2}, \quad (4.45)$$

with respect to $(\psi_m - \psi_1)$.

By differentiating (4.45) with respect to $(\psi_m - \psi_1)$, we derive

$$\psi_T = n\pi - \tan^{-1} \left[\frac{a_{1,0}\omega\tau_0(2M-1)}{3a_{1,1}} \right]. \quad (4.46)$$

It follows that $|\mathcal{B}_{M,1}^{(p')}(0^\circ)|_{\max}^2$ is deduced as

$$\begin{aligned} & |\mathcal{B}_{M,1}^{(p')}(0^\circ)|_{\max}^2 \\ &= a_{1,0}^2 + \frac{18a_{1,1}^2}{\omega^2\tau_0^2(2M-1)^2} + \frac{6a_{1,0}a_{1,1} \sin(\psi_T)}{\omega\tau_0(2M-1)} \\ &\quad - \frac{18a_{1,1}^2 \cos(\psi_T)}{\omega^2\tau_0^2(2M-1)^2} + a_{1,1}^2 + \frac{1}{2}\mathcal{D} \end{aligned} \quad (4.47)$$

$$\begin{aligned} &\geq a_{1,0}^2 + \frac{18a_{1,1}^2(1 - \cos(\psi_T))}{\omega^2\tau_0^2(2M-1)^2} + \frac{6a_{1,0}a_{1,1} \sin(\psi_T)}{\omega\tau_0(2M-1)} \\ &\quad + a_{1,1}^2 = |\mathcal{B}_{M,1}^{(p')}(0^\circ)|_{T'}^2, \end{aligned} \quad (4.48)$$

where (4.48) is obtained by applying $\mathcal{D} \geq 0$ to (4.47). Consequently, the maximal WNG threshold for unbounded phase errors is

$$\text{WNG}_{T'}[\mathbf{h}(\omega)] = \frac{|\mathcal{B}_{M,1}^{(p')}(0^\circ)|_{T'}^2}{[\mathbf{h}(\omega)]^H \mathbf{h}(\omega)}. \quad (4.49)$$

With unbounded phase errors, (4.48) and (4.49) indicate that more microphones enhance the robustness of LDMA.

4.5 Experimental Results

Without loss of generality, we use the first microphone in LDMA as the reference for phase errors. Therefore, ψ_1 is 0 throughout our experiments.

We configure a baseline setup of first-order LDMA, which sets $f = 1$ kHz, $M = 3$ and $\delta = 0.01$ m.

The beam patterns with and without bounded phase errors for the baseline settings are demonstrated in Fig. 4.1. The blue solid lines represent beam patterns without phase errors. The Φ_T values adopted are listed in Table 4.1, where 'C', 'H' and 'S' represent cardioid, hypercardioid and supercardioid respectively. In Fig. 4.2, vertical lines are ζ values computed by using (4.32). Φ_T values on the left of corresponding ζ lines do not cause mainlobe misorientation. From Fig. 4.1 and 4.2, we can observe that whenever $\Phi_T < \zeta$, the mainlobe orientation stays at 0° .

From Fig. 4.2, we can also observe that cardioid has the largest tolerance threshold ζ and its WNG values are always larger than the other two beam patterns given the same Φ_T values. Negative Φ_T values indicate that the phase differences between microphones have not disturbed the original order of microphones for receiving signals. In other words, the effect of having negative Φ_T values is equivalent to enlarging the inter-microphone spacing. Therefore, the WNG values increase when the Φ_T values become more negative. It is interesting to note that the DF values of cardioid and supercardioid increase slightly for small positive Φ_T values. This can be corroborated by the beam pattern shapes in Fig. 4.1(i) and 4.1(iii). We can see that the beam patterns drawn in green dash-dotted lines have narrower mainlobes than the beam patterns drawn in blue solid lines. The DF rebound in Fig. 4.2(ii) can be also explained by the corresponding beam patterns in Fig. 4.1(ii). The beam pattern drawn in a green dash-dotted line has more directivity than the beam pattern drawn in a pink dotted line at 180° . This suggests that the beam pattern drawn in a green dash-dotted line has less directivity than the beam pattern drawn in a pink dotted line at 0° .

Fig. 4.3 shows that unbounded phase errors can also cause mainlobe misorientation. Deploying more microphones can increase the WNG threshold $\text{WNG}_{T'}$, which enhances the robustness of first-order LDMA. No-

tably, the phase error bound $\Delta\psi$ in [24] is 0.154 for cardioid, which can be refuted by ψ_r and ψ_g in Fig. 4.3. This demonstrates mainlobe misorientation can be avoided even when some phase errors are larger than $\Delta\psi$.

Table 4.1: Φ_T values used in Fig. 4.1.

	Red Dashed Line	Green Dash- dotted Line	Pink Dot- ted Line
C	-0.5	0.5	1.5
H	-0.5	1.2	1.5
S	-0.5	0.3	1.5

4.6 Conclusion

Within the context of fixed beamforming, this chapter examined the effects of phase errors on first-order LDMA. We derived the tolerance threshold of bounded phase errors and WNG thresholds of both bounded and unbounded phase errors. In practice, the mainlobe misorientation due to bounded phase errors can be detected by using the tolerance threshold. When the tolerance threshold is exceeded, we know that mainlobe misorientation happens. Our WNG thresholds of both bounded and unbounded phase errors can serve as design criteria for the robustness of first-order LDMA. If the WNG values are above the WNG thresholds, mainlobe misorientation of first-order LDMA is guaranteed not to happen.

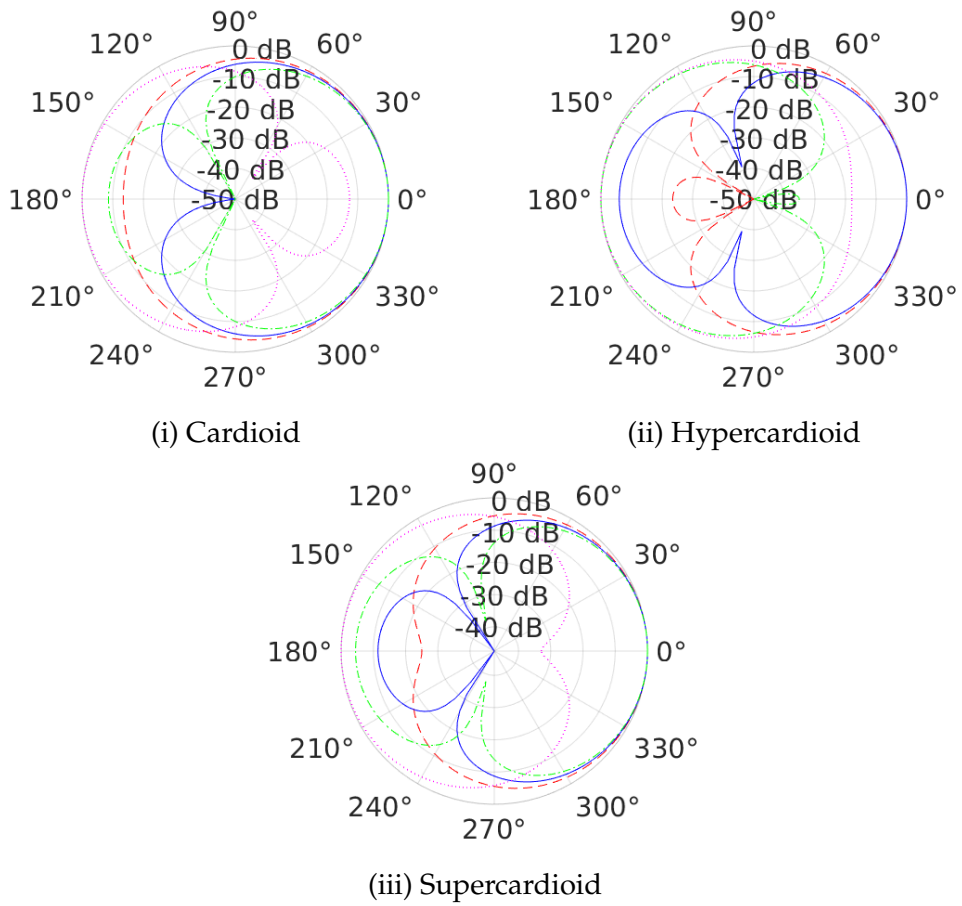


Figure 4.1: Beampatterns of baseline settings with bounded phase errors. Φ_T values used in the figure can be found in Table 4.1.

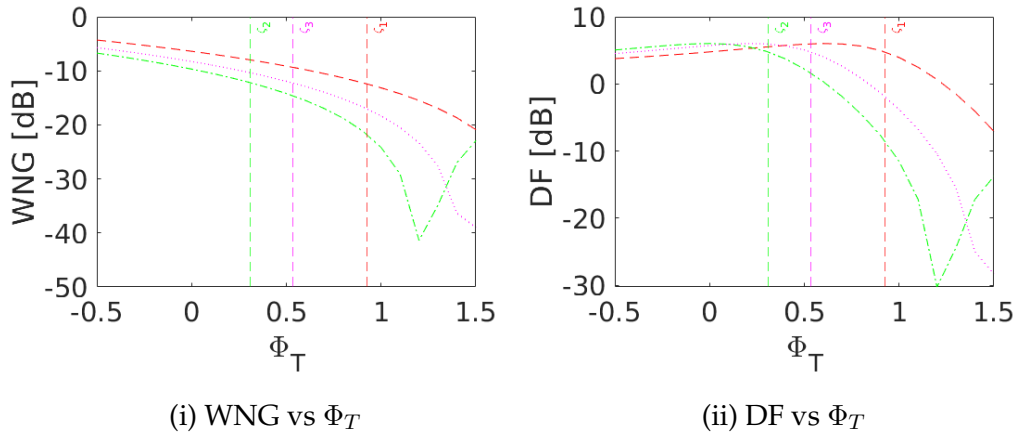


Figure 4.2: WNG and DF plots of baseline settings with bounded phase errors. Red dashed line: cardioid. Green dash-dotted line: hypercardioid. Pink dotted line: supercardioid.

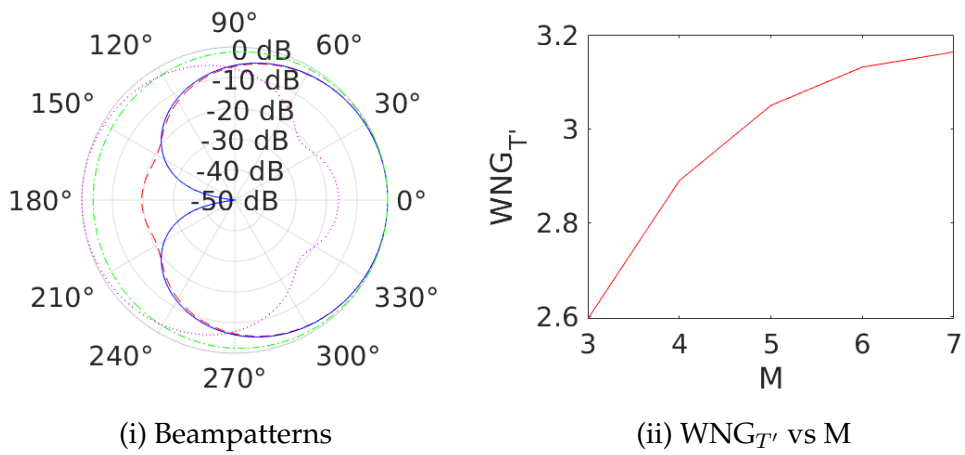


Figure 4.3: Cardioid beampatterns of baseline settings with unbounded phase errors. $\psi_r = [0 \ 12 \ 0.2]$, $\psi_g = [0 \ -10 \ 0.5]$, $\psi_p = [0 \ -0.1 \ -7]$.

Chapter 5

Neural Optimization of Non-Uniform Linear Arrays

Inspired by the robustness analysis presented in the preceding chapter concerning fixed beamforming, our objective is to formulate a novel linear array for fixed beamforming that excels in both robustness and directivity. Fixed beamforming based on uniform linear microphone arrays often suffers from non-optimal performance for broadband signals. This chapter addresses the issue by jointly optimizing the array geometry and spatial filters through a neural network based model. The model, composed of two feed forward neural networks, is optimized in an end-to-end manner. It satisfies the distortionless constraint in the look direction. Experimental results show that the proposed model outperforms the previous state-of-the-art fixed beamformer with overall better scores. Moreover, the proposed model can control the tradeoff between Directivity Factor (DF) and White Noise Gain (WNG) in a flexible way.

5.1 Introduction

Broadband beamformers are widely applied in many areas such as radar, sonar, microphone arrays and radio astronomy [160, 159, 104, 127, 108].

Conventionally, sensors with uniform spacing are deployed in broadband beamformers. However, they have limitations in processing broadband signals. For example, uniformly spaced microphone arrays with limited array aperture and microphones may not function well in all the frequency bands ranging from a few hundred to a few thousand Hertz [31]. Spatial aliasing can happen if the inter-microphone spacing is larger than half of the wavelength for high frequency bands. Meanwhile, a compactly arranged microphone array can be sensitive to white noise and microphone imperfections for low frequency bands [6, 9, 170]. Therefore, uniform arrays often do not yield optimal performance for broadband signals.

Much research has shown that non-uniform arrays have superior performance than their uniform counterparts [145, 147, 174]. The dilemma of spacing for both high and low frequency bands can be mitigated with non-uniform arrangement of microphones. In [31], a robust superdirective broadside beamformer was proposed through both stochastic and analytic optimization. This beamformer optimized array filters along with the non-uniform geometry. Its optimization objectives are either maximum directivity or frequency invariance. In [95], the array geometry optimization is reformulated from mixed-integer programming to convex optimization by relaxing some of the constraints and pre-selecting a set of potential microphone positions. The optimal microphone positions can be chosen from the pre-selected positions. However, mixed-integer problems are NP-hard. As a result, the computational complexity of the algorithm in [95] grows exponentially. It requires careful adjustment between solution optimality and computational feasibility.

Fixed beamformers have been employed for broadband beamforming as they are data independent and can be used in different acoustic environments. During the last decade, fixed beamformers like Differential Microphone Arrays (DMAs) have been popular in broadband beamforming due to their relative frequency-independent behaviour and high directivity gain [6]. Compared with other fixed beamformers such as Delay-and-

Sum (DS) and superdirective beamformers, DMAs have more balanced DF and WNG values. They are inspired by the spatial derivative of the acoustic pressure field [40] and thus have compact apertures.

DMAs of different geometries have been investigated, such as linear [6, 41], circular [114, 67] and concentric circular [66, 70]. Recently, DMA beamformers based on Particle Swarm Optimization (PSO) techniques [84] have successfully optimized the geometry for linear microphone arrays [131, 79]. We can observe that it is common to have microphone spacing larger than 1 cm even among DMAs. The DMA beamformer proposed in [79] focuses on frequency-invariant beampatterns by combining subarrays. In [131], a proposed DMA beamformer exhibited a better DF and WNG tradeoff than traditional approaches. However, the distortionless constraint is not guaranteed in its look direction. This can cause power distortion across different frequency bins, which undermines the quality of the broadband signal perceived. The white noise amplification phenomenon in low frequency bins also persists in these PSO-based DMA beamformers.

To address the above-mentioned issues in broadband beamforming, we propose a novel model called Neural Optimization of Non-Uniform Linear Array (NONULA) for fixed beamformers. The placement of microphones are not constrained to pre-defined locations. Maximum array size and minimum inter-microphone spacing are considered. Our contributions include: (i) To the best of our knowledge, NONULA is the first model that optimizes linear array geometry with neural networks. (ii) NONULA is the first end-to-end neural network-based model for simultaneous array geometry and filter optimization. (iii) NONULA can obtain overall better DF and WNG performance than previous models. (iv) NONULA facilitates designers with a choice of balance between DF and WNG in a flexible manner.

The rest of the chapter is organized into five more sections. In Section 5.2, the employed signal model of beamforming is explained. In Section

5.3, various performance measures utilized in our study are presented. In Section 5.4, we first describe the existing PSO models that can optimize geometry for linear microphone arrays. Then we propose the NONULA model in details. Simulation results of previous models and our proposed NONULA model are discussed in Section 5.5. Section 5.6 summarizes the characteristics of the proposed NONULA model.

5.2 Signal Model

We consider a non-uniform linear array comprised of M omnidirectional microphones. δ_k denotes the distance from the k th microphone to the first microphone and $\delta_1 = 0$. The steering vector can be expressed as [160]

$$\mathbf{d}(\omega, \cos \theta) = [1 \ e^{-j\omega\tau_2 \cos \theta} \ \dots \ e^{-j\omega\tau_M \cos \theta}]^T, \quad (5.1)$$

where $j = \sqrt{-1}$, $\omega = 2\pi f$, $\tau_k = \delta_k/c$, θ is the azimuth angle of the source signal, f is the temporal frequency and c is 340 m/s. We assume the source signal is from the endfire direction at $\theta = 0$.

Under anechoic conditions with far field assumption, the received signal vector $\mathbf{y}(\omega)$ by the microphone array is expressed as

$$\begin{aligned} \mathbf{y}(\omega) &= [Y_1(\omega) \ Y_2(\omega) \ \dots \ Y_M(\omega)]^T \\ &= \mathbf{d}(\omega, \cos \theta_\ell) \mathbf{X}(\omega) + \mathbf{v}(\omega), \end{aligned} \quad (5.2)$$

where $Y_k(\omega)$ is the signal received at the k th microphone, θ_ℓ represents the look direction, $\mathbf{X}(\omega)$ is the source signal and $\mathbf{v}(\omega)$ is the noise vector.

To estimate $\mathbf{X}(\omega)$ from the observed $\mathbf{y}(\omega)$, a complex linear filter $\mathbf{h}(\omega)$ is applied in beamforming. We have

$$\begin{aligned} \hat{\mathbf{X}}(\omega) &= \mathbf{h}^H(\omega) \mathbf{y}(\omega) \\ &= \mathbf{h}^H(\omega) \mathbf{d}(\omega, \cos \theta_\ell) \mathbf{X}(\omega) + \mathbf{h}^H(\omega) \mathbf{v}(\omega), \end{aligned} \quad (5.3)$$

where $\hat{\mathbf{X}}(\omega)$ is the estimate of $\mathbf{X}(\omega)$ from beamforming. The distortionless constraint requires that

$$\mathbf{h}^H(\omega)\mathbf{d}(\omega, \cos \theta_\ell) = 1 \quad \forall \omega \quad (5.4)$$

5.3 Performance Measures

Beampattern quantifies the input-output behaviour of a microphone array given a source signal from the direction θ [8]. It is defined as

$$\mathcal{B}[\mathbf{h}(\omega), \theta] = \mathbf{h}^H(\omega)\mathbf{d}(\omega, \cos \theta). \quad (5.5)$$

The robustness of a microphone array to sensor imperfections such as sensor noise and positional errors can be quantified by White Noise Gain (WNG) [46]. It is expressed as

$$\text{WNG}[\mathbf{h}(\omega)] = \frac{|\mathcal{B}[\mathbf{h}(\omega), \theta_\ell]|^2}{\mathbf{h}^H(\omega)\mathbf{h}(\omega)}. \quad (5.6)$$

Another performance measure commonly used together with WNG is Directivity Factor (DF). It evaluates the directivity of a microphone array in the presence of isotropic noise field. The formula of DF is

$$\text{DF}[\mathbf{h}(\omega)] = \frac{|\mathcal{B}[\mathbf{h}(\omega), \theta_\ell]|^2}{\mathbf{h}^H(\omega)\mathbf{\Gamma}_{0,\pi}(\omega)\mathbf{h}(\omega)}, \quad (5.7)$$

where $\mathbf{\Gamma}_{0,\pi}(\omega)$ is a $M \times M$ matrix. The elements in $\mathbf{\Gamma}_{0,\pi}(\omega)$ are given by

$$[\mathbf{\Gamma}_{0,\pi}(\omega)]_{ij} = \text{sinc}[\omega(\delta_i - \delta_j)/c], \quad (5.8)$$

where $\text{sinc}(x) = \sin x/x$.

When multiple measures are employed simultaneously for a physical system, naturally multi-objective optimization scenarios arise. To compare the performance of different beamforming techniques in a multi-objective manner, we can adopt a weighted sum approach with respect to both WNG and DF [26]:

$$J_s(\omega) = \text{DF}[\mathbf{h}(\omega)] + \text{WNG}[\mathbf{h}(\omega)] \cdot r_w, \quad (5.9)$$

where $J_s(\omega)$ is the multi-objective score for ω and r_w is the weighting coefficient for WNG.

5.4 Models For Geometry Optimization

5.4.1 PSO Models

The ideal beampattern of an N th-order DMA is:

$$\mathcal{B}_N(\theta) = \sum_{n=0}^N a_{N,n} \cos^n \theta, \quad (5.10)$$

where N is the order of derivative and $a_{N,n}$ is the n th coefficient of the beampattern.

Conventionally, a null-constrained approach is an effective way to design DMA beampatterns [6]. An N th-order DMA can have N distinct null directions, where the DMA beampattern is 0 in those directions. The matrix $\mathbf{D}(\omega)$ can be constructed with null constraints:

$$\mathbf{D}(\omega) = \begin{bmatrix} \mathbf{d}^H(\omega, \cos \theta_\ell) \\ \mathbf{d}^H(\omega, \cos \theta_1) \\ \vdots \\ \mathbf{d}^H(\omega, \cos \theta_N), \end{bmatrix} \quad (5.11)$$

where $\theta_1, \dots, \theta_N$ are N distinct null directions. This yields

$$\mathbf{D}(\omega)\mathbf{h}(\omega) = \mathbf{i}, \quad (5.12)$$

where $\mathbf{i} = [1 \ 0 \ \dots \ 0]^T$ is a binary vector of length $N+1$ that has zero entries everywhere except for the first entry.

Given $M > N+1$, a minimum-norm solution of (5.12) can be obtained:

$$\mathbf{h}_{\text{MN}}(\omega) = \mathbf{D}^H(\omega)[\mathbf{D}(\omega)\mathbf{D}^H(\omega)]^{-1}\mathbf{i}, \quad (5.13)$$

which maximizes WNG for DMA. This is also called the Maximum WNG (MWNG) differential beamformer [20].

To optimize the geometry of DMA, PSO techniques [131, 79] have been used to decide the geometry vector $\boldsymbol{\delta} = [\delta_1 \cdots \delta_M]$. In [131], two tradeoff parameters δ_w and δ_d are also employed to further refine the filters $\mathbf{h}(\omega)$:

$$\mathbf{h}(\omega) = \boldsymbol{\Gamma}_w^{-1}(\omega) \mathbf{D}^H(\omega) [\mathbf{D}(\omega) \boldsymbol{\Gamma}_w^{-1}(\omega) \mathbf{D}^H(\omega) + \delta_d \mathbf{I}]^{-1} \mathbf{i}, \quad (5.14)$$

where $\boldsymbol{\Gamma}_w(\omega) = [\boldsymbol{\Gamma}_{0,\pi}(\omega) + \delta_w \mathbf{I}]$. However, δ_d breaks the distortionless constraint when it is not zero.

The PSO algorithm in [131] starts with randomly initializing many candidate solutions for $\boldsymbol{\delta}$, δ_w and δ_d . They together form particles. A fitness function F is defined to evaluate and compare particles. In each iteration, the best particle, i.e., the best candidate solution, is picked from all the particles. Its information is utilized to guide the update of other particles. This update process repeats in every iteration until the specified number of iteration is reached. One of our baselines is a modified implementation of this PSO algorithm.

5.4.2 NONULA

The NONULA model proposed by us consists of two feed forward neural networks: SpacingNet and FilterNet. Fig. 5.1 demonstrates the workflow of NONULA. Denote inter-microphone spacing as $\boldsymbol{\eta} = [\eta_1 \ \eta_2 \ \cdots \ \eta_{M-1}]$, where $\eta_k = \delta_{k+1} - \delta_k$. Initially, the spacing input $\boldsymbol{\eta}_{\text{init}}$ is fed into SpacingNet. The output of SpacingNet is then used to calculate the steering vector $\mathbf{d}(\omega, \cos \theta_\ell)$. Subsequently, both $\mathbf{d}(\omega, \cos \theta_\ell)$ and the filter input are fed into FilterNet. If the termination condition is not met, SpacingNet and FilterNet will repeatedly optimize the spacing and filter output. In this process, the spacing and filter input will remain the same to make the convergence of optimization easier. The weights of SpacingNet and FilterNet and $\mathbf{d}(\omega, \cos \theta_\ell)$ are updated in each iteration.

SpacingNet and FilterNet both have 5 layers: the input layer, three hidden layers and the output layer. SpacingNet uses ReLu as the activation function in hidden layers, whereas FilterNet uses complex ReLu [155, 112]. ReLu is the default activation function in many neural networks by virtue of easy training and good performance. Complex ReLu [155] is necessary for facilitating the complex representation in the filter. The size of input and output layers is $M - 1$ for SpacingNet and M for FilterNet. SpacingNet also has the softmax activation in the final layer. Multiplying softmax outputs by the total array length allocates spacing between microphones.

Denote the minimum spacing by η_{\min} and the maximum array aperture by L_{\max} . Denote the optimized spacing and filter output of SpacingNet and FilterNet by \mathbf{s} and \mathbf{H} respectively. To satisfy the constraint of η_{\min} and L_{\max} , we allocate $L = L_{\max} - \eta_{\min} \times (M - 1)$ as the maximum spacing allocation. The actual spacing is $\boldsymbol{\eta} = \mathbf{s} + \eta_{\min} \cdot \mathbf{1}$, where $\mathbf{1}$ is a vector of 1's having the same length as \mathbf{s} . To satisfy the distortionless constraint, \mathbf{H} is obtained after dividing $\mathbf{h}^H(\omega)\mathbf{d}(\omega, \cos \theta_\ell)$ in every frequency bin for normalization.

The loss function J of NONULA is the mean of negative multi-objective score plus the penalty of under-achieved DF and WNG factors across all the frequency bins of interest:

$$J = \frac{1}{N_\omega} \sum_{\omega} \left[-J_s(\omega) + (\sigma_r(\text{DF}_{tgt}(\omega) - \text{DF}[\mathbf{h}(\omega)]) + (\sigma_r(\text{WNG}_{tgt}(\omega) - \text{WNG}[\mathbf{h}(\omega)])) \right], \quad (5.15)$$

where N_ω is the number of frequency bins, $\sigma_r(\cdot)$ represents the ReLu activation function, $\text{DF}_{tgt}(\omega)$ and $\text{WNG}_{tgt}(\omega)$ are the target DF and WNG for frequency ω . The NONULA model is trained by minimizing (5.15) with gradient descent.

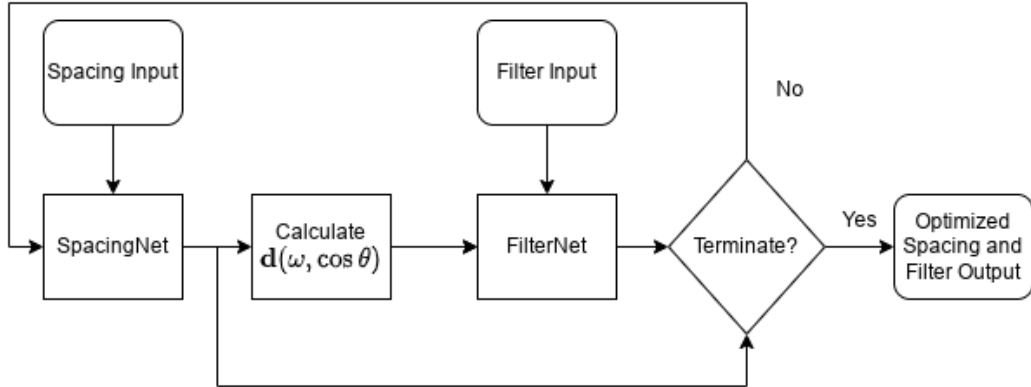


Figure 5.1: Workflow diagram of NONULA

5.5 Experimental Results

We use two baseline models in our experiments. The first one is a PSO-based endfire non-uniform linear array [131]. To have a fair comparison, we implemented this model without distortion in the look direction [117]. Henceforward we refer to this implementation as ‘PSO DMA’. The other baseline models is the uniform DMA [20]. In particular, the uniform DMA is derived from (5.13) and it employs the second-order supercardioid beampattern. The two null directions of are 106° and 153° . The uniform DMA filters are also utilized as the initial filter input for NONULA. The initial spacing input is the uniform spacing given L . η_{\min} is set to 1 cm.

To compare NONULA’s scores with PSO DMA, we conduct two series of experiments. $DF_{tgt}(\omega)$ is set to 13 dB to encourage NONULA to outperform the uniform DMA. When $r_w = 1$, we set $WNG_{tgt}(\omega)$ to 0 dB. This allows NONULA to focus on both WNG and DF. When $r_w = 0.5$, we set $WNG_{tgt}(\omega)$ to -10 dB so that NONULA can have a DF-focused design. NONULA and PSO DMA are optimized with the same settings in frequency bands from 100 Hz to 8 kHz.

A detailed comparison between NONULA and PSO DMA is presented in Tables 5.1 and 5.2. There are five choices for array length L : 13, 18, 23, 28

Table 5.1: Mean scores of NONULA and PSO DMA when $r_w = 1$

L \ M	8		10		12	
	NN	PSO	NN	PSO	NN	PSO
13	16.51	12.50	17.46	13.45	18.21	14.25
18	16.68	13.44	18.63	14.98	19.50	16.25
23	16.77	13.95	18.60	15.89	20.14	17.18
28	17.01	14.25	18.77	16.15	20.26	17.81
33	16.87	14.44	18.88	16.67	20.30	18.11

Table 5.2: Mean scores of NONULA and PSO DMA when $r_w = 0.5$

L \ M	8		10		12	
	NN	PSO	NN	PSO	NN	PSO
13	12.60	11.31	13.12	11.86	13.49	12.30
18	12.83	11.65	14.33	12.95	14.89	13.70
23	12.81	11.96	14.26	13.28	15.40	14.28
28	12.94	11.99	14.43	13.47	15.60	14.63
33	13.03	12.18	14.41	13.66	15.70	14.82

and 33 cm. There are also three choices for the number of microphones M : 8, 10 and 12. The table entries are scores calculated from (5.9) and averaged across frequency bins. Each column in tables is split into two sub-columns. The left sub-column shows the mean scores for NONULA, whereas the right sub-column for PSO DMA. We can observe that the mean scores of NONULA are always higher than its corresponding mean scores of the PSO DMA. In the table, NONULA is abbreviated as NN and PSO DMA is abbreviated as PSO.

The optimized array geometry from NONULA and PSO DMA with two different settings are illustrated in Fig. 5.2 and 5.4. In Fig. 5.2, the ge-

ometry optimized by NONULA has a more complicated layout, whereas the geometry designed by PSO DMA forms only three sub-arrays. This could be due to the fact that neural networks have more power for optimization. With fewer microphones and smaller array length, the complexity levels of geometry from NONULA and PSO DMA are similar in Fig. 5.4. Notably, the subarrays in both NONULA and PSO DMA have internal spacing around 0.02 m. This corresponds with the half wavelength λ of the highest frequency we are interested in, which is $\lambda = 340/(8000 \times 2) = 0.02125$ m. By having the spacing of sub-arrays less than λ , the whole microphone array can effectively avoid spatial aliasing in high frequency bins. Moreover, forming nested arrays with subarrays helps handle broadband signals in both high and low frequency bins.

To have a better understanding of how NONULA’s behaviour changes frequency-wise with respect to other techniques, in Fig. 5.3 and 5.5 we present the performance of DF and WNG. We observe that NONULA has the best overall DF values while maintaining a good level of WNG. For the DF-focused design in Fig. 5.5, NONULA has a tradeoff between DF and WNG and achieves better DF performance. This characteristic is desirable when customized performance is required. PSO DMA cannot enhance its WNG values in low frequency bins to the desired level, whereas NONULA never goes below -10 dB. The uniform DMA also suffers from low WNG values in low frequency bins and it is unstable at some frequency bins.

Since both NONULA and PSO DMA perform multi-objective optimization, we plot Pareto fronts in Fig. 5.6 to better visualize their performance. We use the negative scores as the training loss without penalties. Both NONULA and PSO DMA are retrained at the Mel scale, which better reflects perceptual distance in human hearing. The Pareto front consists of the set of non-dominated DF and WNG pairs. Each pair represents mean DF and WNG values of all frequency bins with a fixed WNG weight r_w . Different pairs are obtained by varying r_w from 0.1 to 1. Fig. 5.6 shows

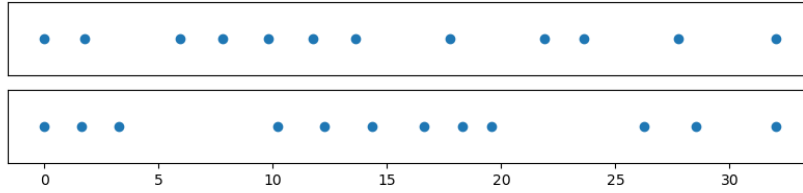


Figure 5.2: Optimized array geometry of NONULA (top) and PSO DMA (bottom), when $r_w = 1$, $M = 12$ and $L = 0.33$.

that the NONULA Pareto front is above the PSO DMA one. This indicates that a better solution always exists in NONULA when fixing one DF or WNG value from PSO DMA. Moreover, the NONULA curve spans a larger range. This illustrates that NONULA is more flexible in the trade-off between DF and WNG. The performance of PSO DMA is limited to a small range of values.

To demonstrate the effectiveness of NONULA at look directions other than the end-fire direction, we performed an additional simulation for the look direction at $\pi/2$. The parameters are $r_w = 1$, $M = 12$ and $L = 0.33$. When the look direction $\theta = \pi/2$, it follows that $\cos \theta = 0$ and the steering vector becomes a constant vector of 1's. There is no surprise that the optimized geometry is almost identical to the initial given geometry, which is a uniform linear array. The array geometry is illustrated in Fig. 5.7. The WNG and DF performance of this array is plotted in Fig. 5.8.

5.6 Conclusion

This chapter proposed a neural network based model that could optimize both linear array geometry and fixed beamforming in an end-to-end fashion. Compared with DMA-based techniques, our approach exhibited superior robustness in the low frequency region. The proposed model outperformed PSO DMA consistently in various settings with overall better scores while offered a more flexible tradeoff between DF and WNG. This

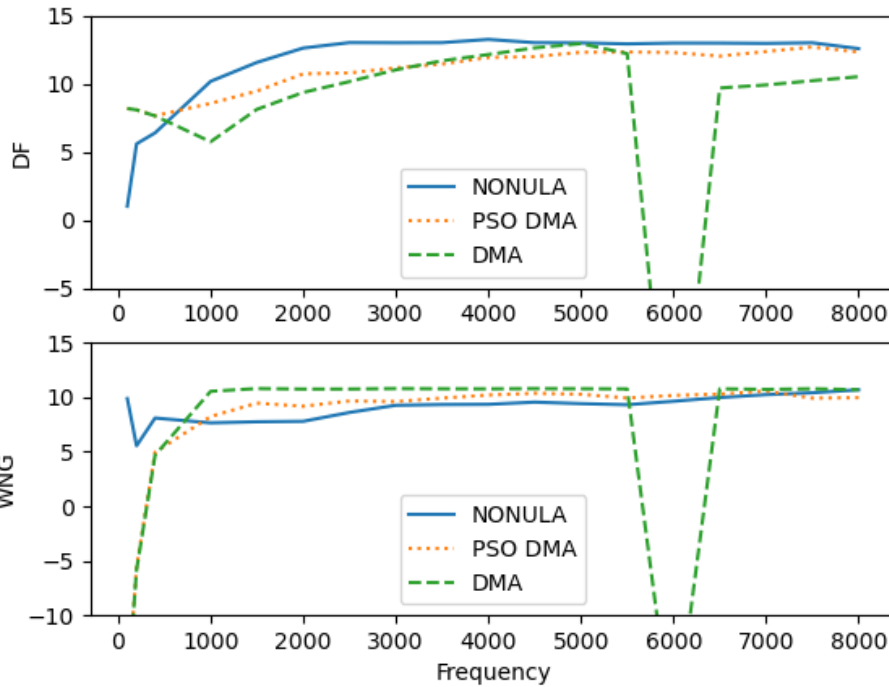


Figure 5.3: Performance of NONULA compared with other techniques when $r_w = 1$, $M = 12$ and $L = 0.33$.

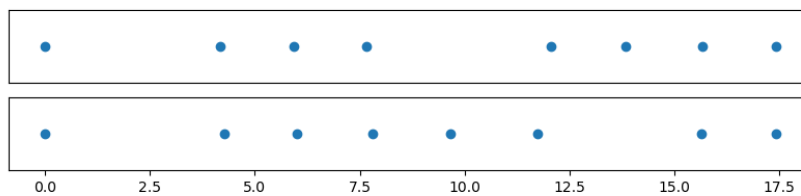


Figure 5.4: Optimized array geometry of NONULA (top) and PSO DMA (bottom), when $r_w = 0.5$, $M = 8$ and $L = 0.18$.

shows that neural networks are more powerful tools for linear microphone array optimization.

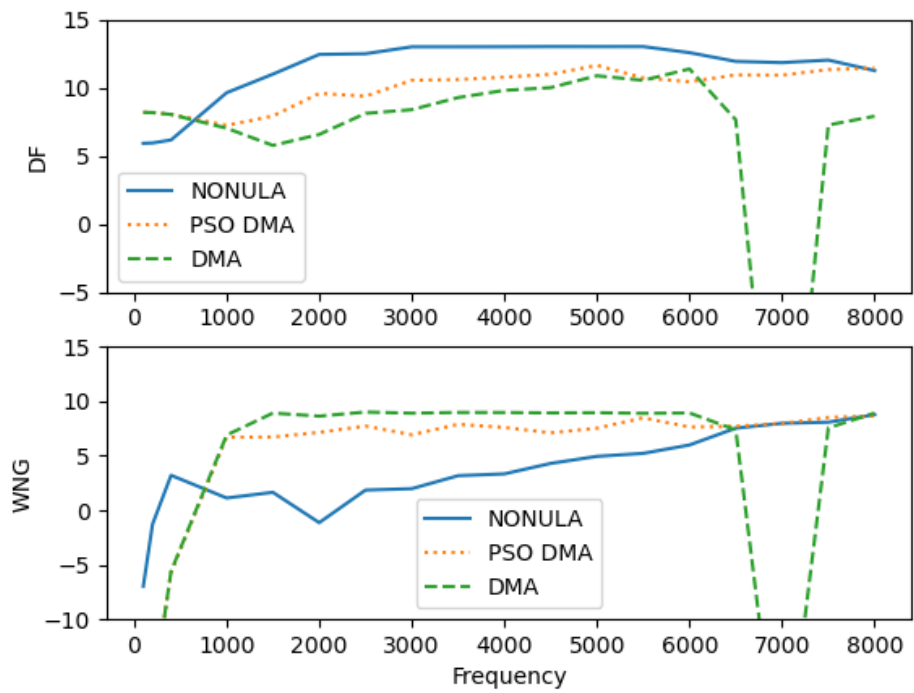


Figure 5.5: Performance of NONULA compared with other techniques when $r_w = 0.5$, $M = 8$ and $L = 0.18$. NONULA has a tradeoff between DF and WNG to achieve better DF when it is DF-focused.

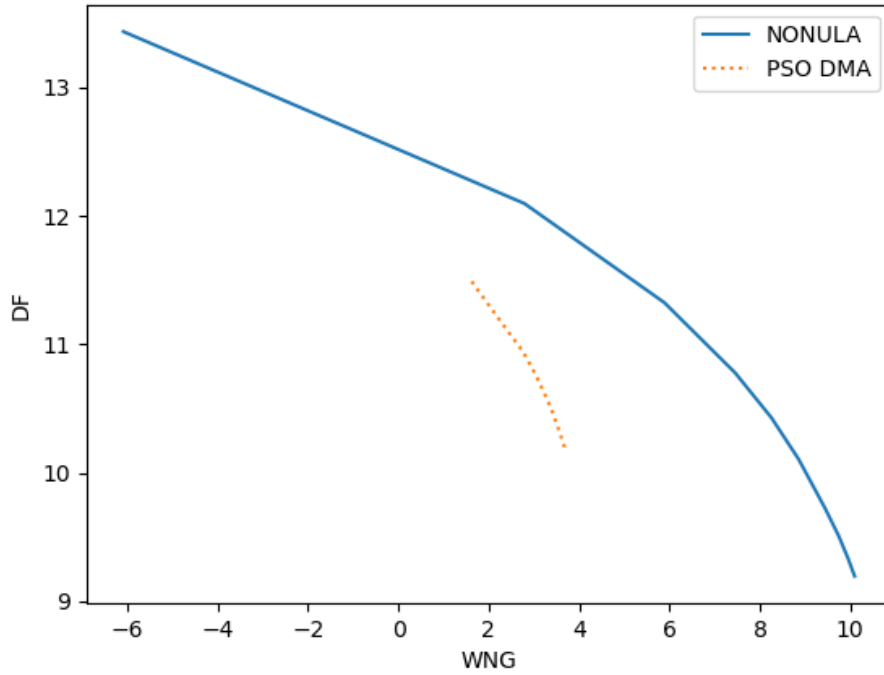


Figure 5.6: Pareto fronts of NONULA and PSO DMA when $M = 12$ and $L = 0.33$. Each pair of DFs and WNGs is averaged across frequency bins. Models are trained at the Mel scale.

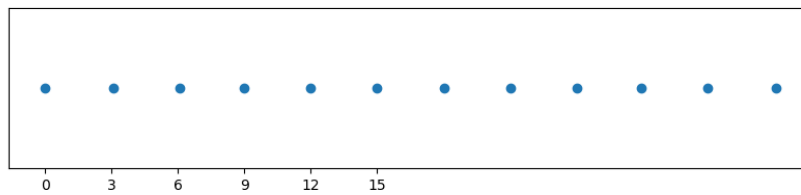


Figure 5.7: Optimized array geometry of NONULA when $r_w = 1$, $M = 12$ and $L = 0.33$. The look direction is $\pi/2$.

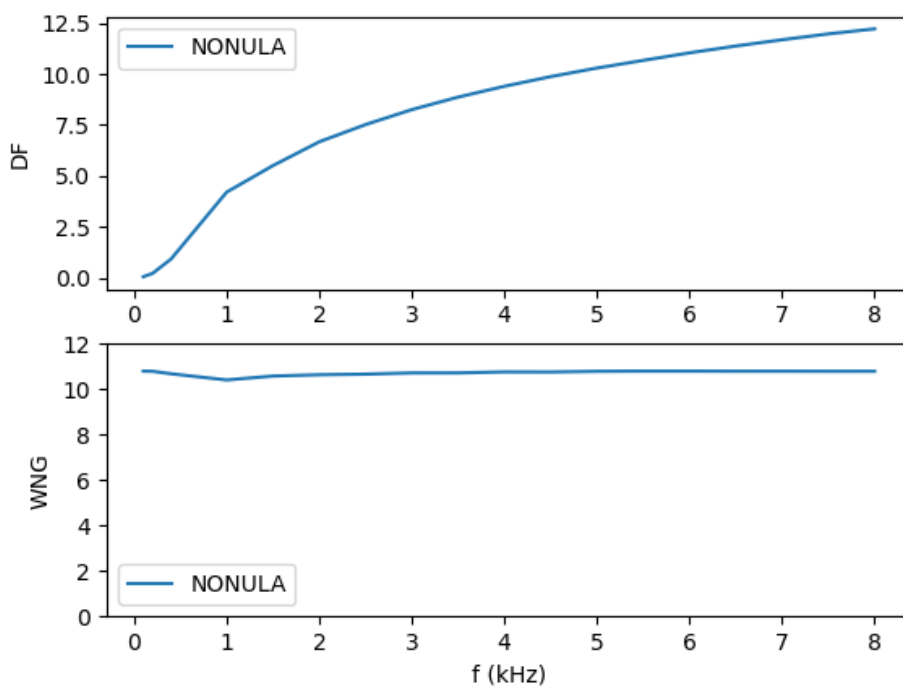


Figure 5.8: Performance of NONULA when $r_w = 1$, $M = 12$, $L = 0.33$ and $\theta = \pi/2$.

Chapter 6

Geometrically Optimized Neural Fixed Beamformers

This chapter presents a novel approach to optimizing fixed beamformers in speech signal processing using neural networks with flexible geometric constraints. While various microphone array geometries have been investigated, a unified neural network framework for optimizing fixed beamformers with different geometric settings is still lacking. Additionally, there is a lack of geometry optimization for non-linear microphone arrays. To address these issues, we propose a unified signal model applicable to all geometric settings and employ two heterogeneous neural networks to simultaneously optimize both the geometry and spatial filter of fixed beamformers. Our approach incorporates an augmented Lagrangian in the loss function to facilitate the optimization process. Experimental results show that our approach outperforms conventional approaches in terms of Directivity Factors (DFs) and white Noise Gain (WNGs). We also discovered a new geometric setting in the concentric circular array and validated the effectiveness of our model on an arbitrary disc setting.

6.1 Introduction

Microphone arrays are indispensable in various hands-free communication systems and far-field speech recognition systems, especially in challenging environments. Devices that are equipped with microphone arrays hold great potential for applications such as speaker separation, speaker localization, speech dereverberation, and speech enhancement. Beamforming, as a critical component of microphone arrays, has garnered significant attention. It acts as a spatial filtering process, enhancing the target signal from the desired direction while suppressing interference from undesired directions [160]. Generally, beamforming algorithms can be classified into two categories: adaptive beamformers and fixed beamformers [159]. Fixed beamformers, in comparison to adaptive beamformers, tend to be more robust as they do not involve a data adaptation procedure. Furthermore, fixed beamformers serve as an integral part of the generalized sidelobe canceller (GSC) structure, which provides an efficient real-time implementation for the widely used adaptive beamformer known as the Minimum Variance Distortionless Response (MVDR) [58, 65].

In the realm of fixed beamforming, there has been growing interest in the application of differential beamforming or Differential Microphone Arrays (DMAs) due to their distinct advantages over certain traditional beamformers [6, 20, 9, 15]. Firstly, DMAs generate a relatively frequency-invariant beampattern, making them well-suited to broadband speech processing. Secondly, DMAs have the potential to achieve high DFs despite small and compact apertures. Lastly, by incorporating appropriate optimization constraints [6] or predefined target beampatterns [67], DMAs can achieve a more balanced combination of DFs and WNGs compared to other fixed beamformers like Delay-and-Sum and superdirective beamformers.

Various DMA geometries have been studied, including uniform linear arrays [20, 13], non-uniform linear arrays [176, 78], uniform circular ar-

rays [7], and uniform concentric circular arrays [165]. When it comes to a microphone array with a fixed geometry, designing DMAs typically involves striking a balance between WNGs and DFs [68]. Robust DMAs, known for achieving maximum WNG with the minimum-norm solution, tend to have a lower DF. On the other hand, Maximum Directivity (MDF) differential beamformers can attain a high DF at the expense of WNG. To address this trade-off, a parameterized DMA has been proposed in [69], where DF and WNG are compromised based on a parameter. Breaking this compromise, it is possible to improve WNG without sacrificing DF by employing more microphone elements than what is required for the order robust DMAs [128, 67] or by leveraging the acoustic properties of directional sensors [72, 73, 74, 106]. Similarly, DF can be enhanced without sacrificing WNG through the use of acoustic vector sensors [107, 105]. However, such improvements come at the financial cost in practice. Incorporating more microphones not only increases the cost of the microphones themselves but also leads to a more complex hardware architecture. Additionally, implementing directional sensors in products necessitates sound transparency, resulting in a much more intricate industrial design compared to omnidirectional sensors.

As mentioned above, the majority of recent DMAs have been developed based on specific given geometries, without considering the optimization of geometry itself. To the best of our knowledge, the optimization of geometry design for DMA beamformers has only been explored for linear microphone arrays using techniques such as particle swarm optimization (PSO) [131, 79] or convex optimization processes [96]. In the PSO-based approach proposed in [131], DMA beamformers demonstrated a superior tradeoff between DF and WNG compared to traditional methods. However, the distortionless constraint in the desired direction is not guaranteed, leading to power distortion across different frequency bins and deteriorating the quality of perceived broadband signals. Additionally, these PSO-based DMA beamformers suffer from white noise ampli-

fication in low-frequency bins. To address these limitations, a neural optimization method for fixed beamformers on linear arrays was proposed utilizing machine learning techniques [171]. This approach exhibits improved overall WNG and DF compared to PSO-based DMA beamformers. However, it is important to note that this method is limited to linear arrays and does not provide separate improvements for WNG and DF individually.

Building upon the work presented in [171], we propose a novel neural network-based method that enables the joint optimization of array geometry and fixed beamformers. This method caters to a range of flexible geometries, including linear arrays, circular arrays, and concentric circular arrays. The key innovation lies in incorporating the ResNet structure and the augmented Lagrangian approach within the loss function to facilitate the optimization process. ResNets are well-known for their proven global convergence property [35, 36]. Inspired by this, we reformulate the constrained optimization problem associated with the performance of fixed beamformers within a neural network framework. Our framework focuses on enhancing the effectiveness of the optimization process by leveraging the power of nonlinear mappings between the inputs and outputs of neural networks. These mappings capture the optimization of geometric states and spatial filters, enabling us to achieve superior performance in the beamforming process.

Our contributions can be summarized as follows: (i) We establish a unified neural network framework for optimizing 3D geometry alongside fixed beamformers. (ii) We introduce Geometrically Optimized Neural Fixed Beamformers (GONFBs), which optimize beam patterns of fixed beamformers and array geometries using gradient descent. (iii) We effectively apply the augmented Lagrangian method in the loss function and demonstrate its convergence property within neural network models. Furthermore, we compare the fixed beamformers designed by GONFBs to existing DMA-based fixed beamformers on different types of arrays. Exper-

imental results show that our approach exhibit significant improvements in both WNG and DF compared to current DMA-based methods.

The remaining sections of this chapter are organized as follows: Section 6.2 presents a detailed description of our signal model and problem formulation. In Section 6.3, we outline the performance measures utilized in this study. Section 6.4 contextualizes DMA beamformers within our research framework. Building upon this, Section 6.5 introduces our neural network model, which optimizes both array geometry and spatial filters of fixed beamformers. Section 6.6 provides a comprehensive discussion on our experimental settings and the corresponding results. Lastly, in Section 6.7, we draw meaningful conclusions based on our findings.

6.2 Signal Model and Problem Formulation

The microphone array for a fixed beamformer practically can form any geometry in a 3D space. To accommodate the flexible geometry of real-world microphone arrays, we propose to unify the coordinate system for fixed beamformers, as shown in Fig. 6.1. Three axes x , y and z represent three orthogonal spatial dimensions. In Fig. 6.1, the microphone array is located on the xy -plane arbitrarily. M_k represents the k th microphone, the coordinates of which are $\mathbf{P}_k = [x_k, y_k, z_k]^T$. The direction of the plane wave can be represented by a unit vector

$$\mathbf{a} = [-\sin \theta \cos \phi \quad -\sin \theta \sin \phi \quad -\cos \theta]^T, \quad (6.1)$$

where θ is the elevation angle and ϕ is the azimuth angle of the plane wave. By utilizing the geometric definition of the dot product, we can derive the distance l_{τ_k} as:

$$\begin{aligned} l_{\tau_k} &= \mathbf{P}_k^T \cdot \mathbf{a} \\ &= -(x_k \sin \theta \cos \phi + y_k \sin \theta \sin \phi + z_k \cos \theta). \end{aligned} \quad (6.2)$$

Let $c = 340$ m/s be the speed of sound in air. The time difference of arrival between the origin o and microphone M_k is $\tau_k = l_{\tau_k}/c$. Thus, the steering vector [160, 158] can be defined as

$$\begin{aligned} \mathbf{d}(\omega, \mathbf{a}) &= [e^{-j\omega \mathbf{P}_1^T \cdot \mathbf{a}/c} \dots e^{-j\omega \mathbf{P}_S^T \cdot \mathbf{a}/c}]^T \\ &= [e^{-j\omega \tau_1} \dots e^{-j\omega \tau_S}]^T, \end{aligned} \quad (6.3)$$

where $j = \sqrt{-1}$, $\omega = 2\pi f$ and f is the temporal frequency.

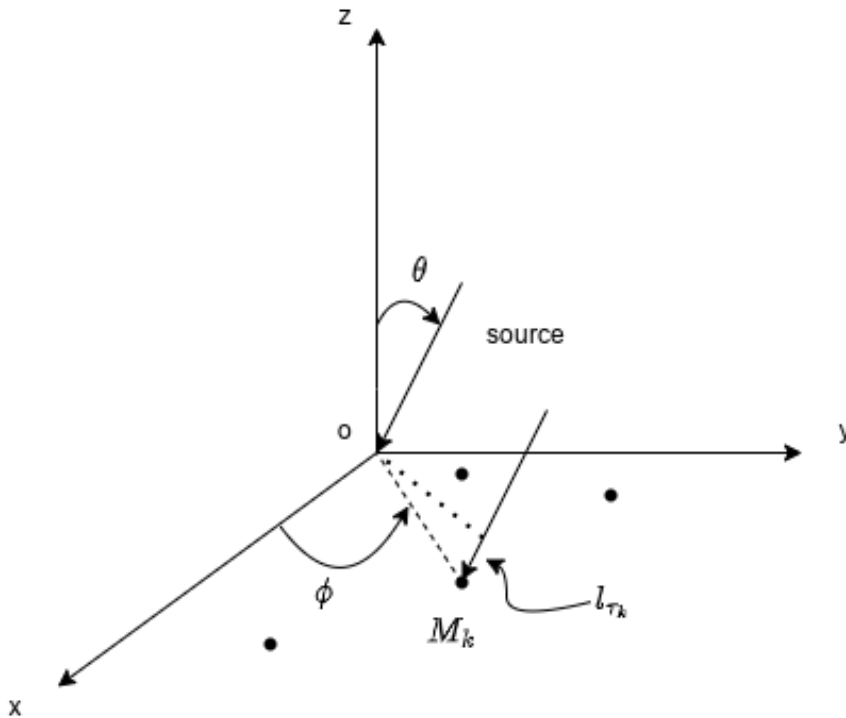


Figure 6.1: An illustration of the unified coordinate system in a 3D space. The elevation angle and the azimuth angle of the impinging plane wave are denoted by θ and ϕ respectively. The plane wave travels an extra distance l_{τ_k} to reach microphone M_k after arriving at the origin o .

We define $\mathbf{X}(\omega)$ as the far field source signal and $\mathbf{v}(\omega)$ as the noise vector. Under anechoic conditions, the received signal vector $\mathbf{y}(\omega)$ is given

by

$$\begin{aligned}\mathbf{y}(\omega) &= [Y_1(\omega) Y_2(\omega) \cdots Y_S(\omega)]^T \\ &= \mathbf{d}(\omega, \mathbf{a})\mathbf{X}(\omega) + \mathbf{v}(\omega),\end{aligned}\quad (6.4)$$

where $Y_k(\omega)$ is the signal received at the k th microphone, $\mathbf{v}(\omega)$ is the noise vector and S is the total number of microphones.

By applying a beamforming filter $\mathbf{h}(\omega)$ to $\mathbf{y}(\omega)$, $\hat{\mathbf{X}}(\omega)$ can be estimated:

$$\begin{aligned}\hat{\mathbf{X}}(\omega) &= \mathbf{h}^H(\omega)\mathbf{y}(\omega) \\ &= \mathbf{h}^H(\omega)\mathbf{d}(\omega, \mathbf{a})\mathbf{X}(\omega) + \mathbf{h}^H(\omega)\mathbf{v}(\omega).\end{aligned}\quad (6.5)$$

In this way, a beamformer tries to recover $\mathbf{X}(\omega)$ from estimating $\hat{\mathbf{X}}(\omega)$. The filter $\mathbf{h}(\omega)$ should satisfy the distortionless constraint, which is

$$\mathbf{h}^H(\omega)\mathbf{d}(\omega, \mathbf{a}) = 1 \quad \forall \omega. \quad (6.6)$$

The definition of the steering vector in Eq. 6.3 is a general description of the spatial information of a microphone array in any geometry. It can be further specified in each particular geometry. For example, for a linear array as illustrated in Fig. 6.2, the unit vector \mathbf{a} and the coordinates \mathbf{P}_k can both be simplified. Since the azimuth angle cannot be perceived by the linear array due to its one-dimensional geometry, \mathbf{a} can be redefined as

$$\mathbf{a}_L = [-\sin \theta \quad -\sin \theta \quad -\cos \theta]^T. \quad (6.7)$$

Similarly, \mathbf{P}_k can be redefined as $\mathbf{P}_{L,k} = [0, 0, z_k]^T$. Define $q_k = -z_k$ such that q_k is the non-negative distance between the reference microphone and the k th microphone, we have $\mathbf{P}_{L,k} = [0, 0, -q_k]^T$. Consequently, the distance l_{L,τ_k} is:

$$\begin{aligned}l_{L,\tau_k} &= \mathbf{P}_{L,k}^T \cdot \mathbf{a}_L \\ &= q_k \cdot \cos \theta.\end{aligned}\quad (6.8)$$

This leads to the commonly used steering vector formula for linear arrays [6, 79]:

$$\mathbf{d}_L(\omega) = [1 e^{-j\omega q_2 \cos \theta/c} \dots e^{-j\omega q_S \cos \theta/c}]^T, \quad (6.9)$$

where \mathbf{a}_L is omitted for the simplicity of the equation.

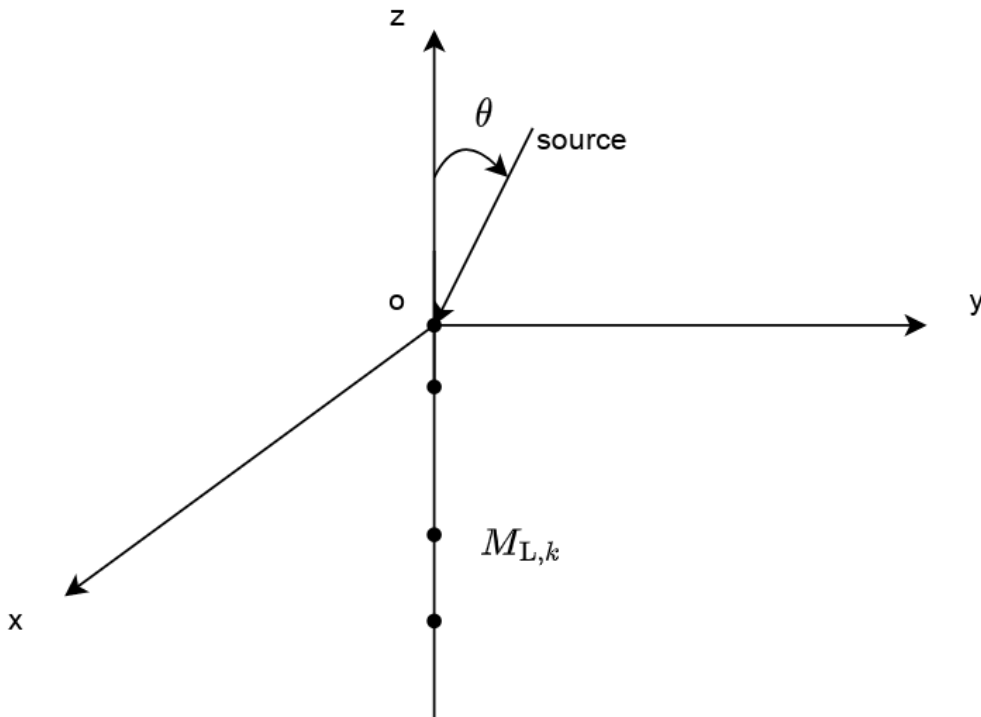


Figure 6.2: An illustration of a linear array in a 3D space . The origin is at the first microphone receiving signals.

A Uniform Circular Microphone Array (UCMA) as shown in Fig. 6.3 is often employed due to its good steering capability [67]. We use the x - y plane to compare with the state-of-the-art frequency-invariant UCMA approach. The radius of the circle is r . The angular position of the k th microphone $M_{C,k}$ measured anti-clockwise from the y axis is ψ_k . \mathbf{P}_k can be redefined as $\mathbf{P}_{C,k} = r[\cos \psi_k, \sin \psi_k, 0]^T$. Thus, the directional vector of the

plane wave \mathbf{a}_C is

$$\mathbf{a}_C = [-\cos \phi \quad -\sin \phi \quad 0]^T. \quad (6.10)$$

The distance l_{C,τ_k} can now be calculated:

$$\begin{aligned} l_{C,\tau_k} &= \mathbf{P}_{C,k}^T \cdot \mathbf{a}_C \\ &= -r(\cos \phi \cos \psi_k + \sin \phi \sin \psi_k) \\ &= -r \cos(\phi - \psi_k). \end{aligned} \quad (6.11)$$

The steering vector of a circular array is

$$\mathbf{d}_C(\omega) = [e^{j\omega \cos(\phi-\psi_1)r/c} \dots e^{j\omega \cos(\phi-\psi_S)r/c}]^T. \quad (6.12)$$

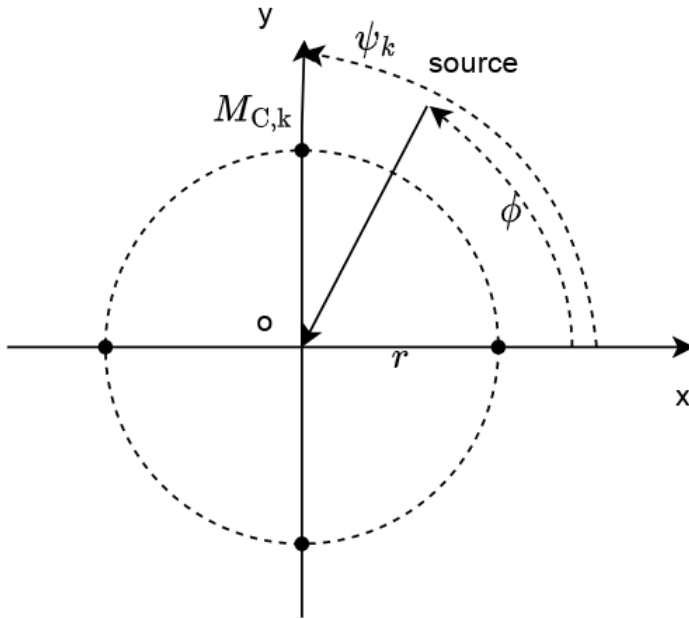


Figure 6.3: An illustration of a UCMA with 4 microphones. The z axis is not considered in this figure.

The geometry of a Uniform Concentric Circular Microphone Array (UC-CMA) composed of multiple UCMA's, is shown in Fig. 6.4. The radius of

the i th ring is r_i . The angular position of the k th microphone on the i th ring is $\psi_{i,k}$. \mathbf{P}_k can be redefined as $\mathbf{P}_{\text{CC},i,k} = r_i[\cos \psi_{i,k}, \sin \psi_{i,k}, 0]^T$. The directional vector of the plane wave \mathbf{a}_{CC} is the same as (6.10). We derive the distance $l_{\text{CC},\tau_{i,k}}$:

$$\begin{aligned} l_{\text{CC},\tau_{i,k}} &= \mathbf{P}_{\text{CC},i,k}^T \cdot \mathbf{a}_{\text{CC}} \\ &= -r_i(\cos \phi \cos \psi_{i,k} + \sin \phi \sin \psi_{i,k}) \\ &= -r_i \cos(\phi - \psi_{i,k}). \end{aligned} \quad (6.13)$$

The steering vector of the i th ring is

$$\mathbf{d}_{\text{CC},i}(\omega) = [e^{j\omega \cos(\phi - \psi_{i,1})r_i/c} \dots e^{j\omega \cos(\phi - \psi_{i,S_i})r_i/c}]^T, \quad (6.14)$$

where S_i is the total number of microphones on the i th ring. The steering vector of the whole UCCMA is

$$\mathbf{d}_{\text{CC}}(\omega) = [\mathbf{d}_{\text{CC},1}^T(\omega), \dots, \mathbf{d}_{\text{CC},I}^T(\omega)], \quad (6.15)$$

where I is the number of rings in the UCCMA.

For an array that is arbitrarily located on a disc, the coordinates of its k th microphone is denoted as $\mathbf{P}_{\text{AD},k} = r_k[\cos \psi_k, \sin \psi_k, 0]^T$. Following the derivation process of (6.12) and (6.14), we can also derive $\mathbf{d}_{\text{AD}}(\omega)$:

$$\mathbf{d}_{\text{AD}}(\omega) = [e^{j\omega \cos(\phi - \psi_1)r_1/c} \dots e^{j\omega \cos(\phi - \psi_S)r_S/c}]^T. \quad (6.16)$$

6.3 Performance Measures

Beampattern characterizes the response of a microphone array as a function of the filter and the direction of incident sound waves [8]. It yields a graphical representation of the spatial sensitivity of the array to signals arriving from different directions. It is defined as

$$\mathcal{B}[\mathbf{h}(\omega), \mathbf{a}] = \mathbf{h}^H(\omega)\mathbf{d}(\omega, \mathbf{a}). \quad (6.17)$$

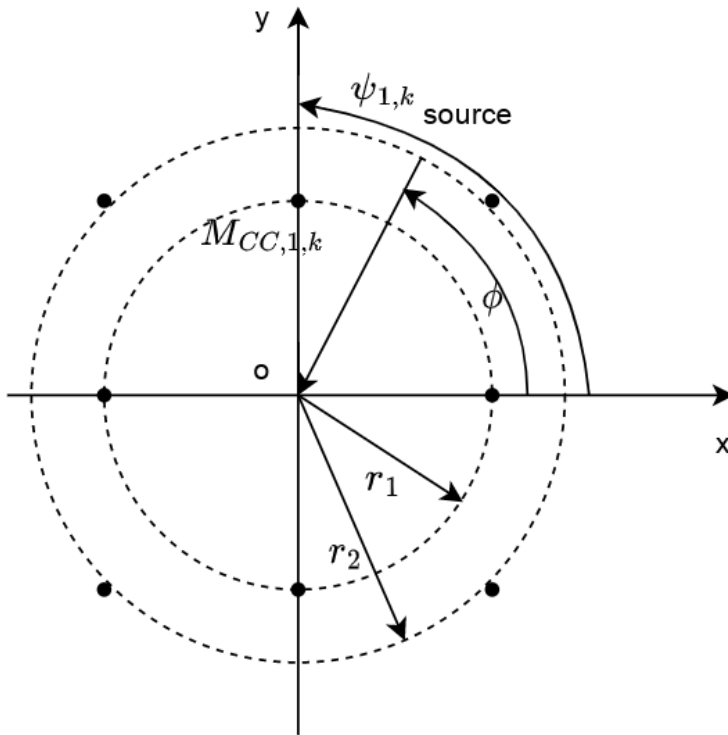


Figure 6.4: An illustration of a UCCMA with 2 rings and 4 microphones on each ring.

The robustness of a microphone array is indicated by White Noise Gain (WNG) [46]. The higher the WNG is, the more resilient the microphone arrays are against self-noise and microphone mismatches. The formula of WNG is

$$\text{WNG}[\mathbf{h}(\omega)] = \frac{|\mathcal{B}[\mathbf{h}(\omega), \mathbf{a}_\ell]|^2}{\mathbf{h}^H(\omega)\mathbf{h}(\omega)}, \quad (6.18)$$

where \mathbf{a}_ℓ is the desired look direction of the array.

The directionality of a microphone array is measured by Directivity Factor (DF). It is a ratio of the output power in the direction of interest to the total output power. High DF suggests that the array can focus on a particular direction while suppressing the energy from other directions. It

is defined as

$$\text{DF}[\mathbf{h}(\omega)] = \frac{|\mathcal{B}[\mathbf{h}(\omega), \mathbf{a}_\ell]|^2}{\mathbf{h}^H(\omega)\mathbf{\Gamma}_{0,\pi}(\omega)\mathbf{h}(\omega)}, \quad (6.19)$$

where $\mathbf{\Gamma}_{0,\pi}(\omega)$ is a square matrix of size S . The elements in $\mathbf{\Gamma}_{0,\pi}(\omega)$ are given by

$$[\mathbf{\Gamma}_{0,\pi}(\omega)]_{ij} = \text{sinc}[\omega\|\mathbf{P}_i - \mathbf{P}_j\|_2/c], \quad (6.20)$$

where $\text{sinc}(x) = \sin x/x$.

6.4 DMA Beamformers

DMAs are well known for their relative frequency-invariant beampatterns. On an x - y plane, the beampattern of an N th order DMA can be simplified to [6]:

$$\mathcal{B}_N(\phi) = \sum_{n=0}^N a_{N,n} \cos^n \phi, \quad (6.21)$$

where N is the order of DMA and $a_{N,n}$ is the n th coefficient of the beampattern. Some "ideal" beampatterns have been summarized for DMAs of different orders, like hypercardioid and supercardioid. However, an "ideal" beampattern is only optimal with respect to one performance measure. For example, hypercardioid maximizes DF but has poor WNG. Furthermore, the choice for the order of DMA is another issue. A higher order DMA is better at suppressing noise, but less robust.

One popular technique of expressing exponential terms in DMA beampatterns is utilising the Jacobi-Anger expansion [67]. In a uniform circular

DMA, we have:

$$e^{j\bar{\omega} \cos(\phi - \psi_k)} = \sum_{n=-\infty}^{\infty} j^n J_n(\bar{\omega}) e^{-jn(\phi - \psi_k)} \quad (6.22)$$

$$= \sum_{n=-\infty}^{\infty} j^n J_n(\bar{\omega}) e^{jn(\phi - \psi_k)} \quad (6.23)$$

$$= J_0(\bar{\omega}) + 2 \sum_{n=1}^{\infty} j^n J_n(\bar{\omega}) \cos[n(\phi - \psi_k)], \quad (6.24)$$

where $\bar{\omega} = \omega r/c$ and $J_n(\bar{\omega})$ is the n -th order Bessel function of the first kind. The approximated beampatterns exhibit least-square errors in relation to the “ideal” beampatterns. Nonetheless, the occurrence of zeros of the Bessel function gives rise to the issue of deep nulls, which significantly undermines the performance of the beamformer at specific frequencies.

An alternative way of designing DMA beamformers is by using the null-constrained approach [6]. This is inspired by the observation that an N th-order DMA can have N distinct null directions. On an x - y plane, a matrix $\mathbf{D}(\omega)$ can be constructed as:

$$\mathbf{D}(\omega) = \begin{bmatrix} \mathbf{d}^H(\omega, \phi_\ell) \\ \mathbf{d}^H(\omega, \phi_1) \\ \vdots \\ \mathbf{d}^H(\omega, \phi_N) \end{bmatrix}, \quad (6.25)$$

where ϕ_ℓ is the look direction and ϕ_1, \dots, ϕ_N are N distinct null directions. Thus, $\mathbf{h}(\omega)$ can be derived by solving

$$\mathbf{D}(\omega)\mathbf{h}(\omega) = \mathbf{i}, \quad (6.26)$$

where $\mathbf{i} = [1 \ 0 \ \dots \ 0]^T$ is a one-hot vector of length $N + 1$. In this null-constrained approach, it is crucial to decide the number and the value of null directions. Yet there is no good mechanism of selecting parameters for null directions other than manually picking some.

The limitations of DMA beamformers in selecting optimal parameters, such as the order of DMA and null directions, impede their ability to provide optimal solutions for beamforming tasks. In contrast, machine learning models, such as neural networks, excel at optimizing parameters and searching for near-optimal solutions when a globally optimal solution cannot be achieved analytically. As a result, there is a need for a neural network model that can enhance the performance of beamformers.

6.5 Neural Network Model

Deep neural networks are known for their universal representation power when combined with nonlinear activation functions [173]. Previous research efforts have demonstrated the excellent convergence characteristics of neural network architectures such as ResNet in the pursuit of global optima [35, 36]. Consequently, employing a ResNet-like neural network model for the optimization of fixed beamformers should be no exception when seeking near-optimal solutions. Empirical validation of the ResNet-like neural network architecture can be found in the next section.

We propose a model called Geometrically Optimized Neural Fixed Beamformers (GONFBs). The full model consists of two heterogeneous neural networks, GNet and FNet. GNet is a fully connected feed-forward neural network, and FNet has an architecture resembling ResNet. The model is trained in a cascaded manner, as shown in Fig. 6.5. GNet takes initial geometry inputs, i.e., the initial coordinates of microphones $\mathbf{P} = [\mathbf{P}_1, \dots, \mathbf{P}_S]^T$, and produces optimized microphone coordinates \mathbf{P}_{opt} . The steering vector $\mathbf{d}(\omega, \mathbf{a}_\ell)$ can be calculated by utilizing \mathbf{P}_{opt} and the direction of signals \mathbf{a}_ℓ . Subsequently, FNet takes $\mathbf{d}(\omega, \mathbf{a}_\ell)$ and the initial filter $\mathbf{h}(\omega)$ to produce the optimized filter $\mathbf{h}_{\text{opt}}(\omega)$. This process is iterated until the termination condition is met. During each iteration, the weights of GNet and FNet are updated by gradient descent in an unsupervised manner. The inputs \mathbf{P} , $\mathbf{h}(\omega)$ and \mathbf{a}_ℓ remain the same to make the training of

neural networks easier.

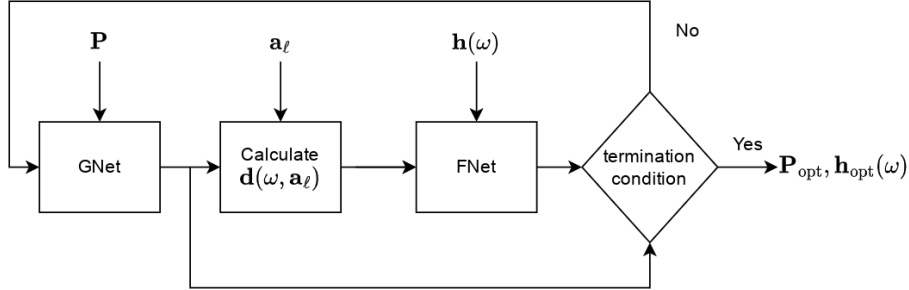


Figure 6.5: Workflow diagram of GONFB.

FNet composes an input linear layer, an output linear layer and multiple ResBlocks in between as shown in Fig. 6.8. All layers in FNet handle complex data by enabling independent processing of the real and imaginary parts of the input [112]. Specifically, the imaginary parts of the input are treated as though they were real. A linear layer multiplies the input with a weight matrix. The input linear layer allows for the transformation of the input into a new latent representation that captures important features of the data. The output linear layer extracts the latent representation into $\mathbf{h}_{\text{opt}}(\omega)$ with desired dimensions. A ResBlock is a building block inspired from ResNet [59], as shown in Fig. 6.7. We employ the residual learning mechanism in ResBlocks, which adds an identity mapping between the input and output, to ease the training of deep neural networks. The GELU function is expressed as [60]

$$\text{GELU}(u) = u\Phi(u) = u \cdot \frac{1}{2}[1 + \text{erf}(u/\sqrt{2})], \quad (6.27)$$

where u is the input of the function, $\Phi(u)$ is the standard Gaussian cumulative distribution function which can be algebraically represented by a manipulation of the error function

$$\text{erf}(u) = \frac{2}{\sqrt{\pi}} \int_0^u e^{-t^2} dt. \quad (6.28)$$

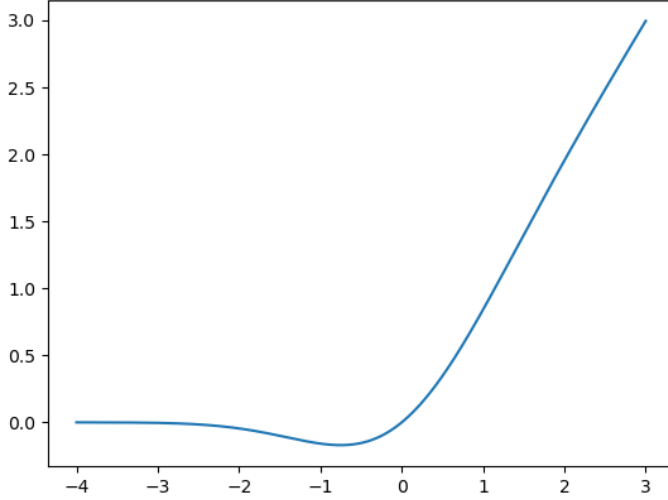


Figure 6.6: A plot of the GELU function with inputs from -4 to 3.

A plot of GELU is shown in Fig. 6.6. The GELU function scales inputs by their value instead of gating inputs by their signs. This has shown superior performance than the ReLU and ELU functions in computer vision, natural language processing, and speech tasks [60]. The hyperbolic tangent (tanh) function is a commonly used activation function in neural networks. Its range is between -1 to 1 and it helps prevent saturation of neurons. The normalization layer is incorporated to facilitate the optimization process by centering the input data and scaling it to have unit variance. Specifically, the normalization layer transforms the input by subtracting its mean and dividing it by its standard deviation, resulting in a zero mean and unit variance representation. Finally, to enforce the distortionless constraint, we divide $\mathbf{h}_{\text{opt}}(\omega)$ by the product $\mathbf{h}_{\text{opt}}^H(\omega)\mathbf{d}(\omega, \mathbf{a}_\ell)$.

GNet has three layers in total: an input linear layer, a hidden layer and an output linear layer. In our experiments, it turns out that the optimization of geometry requires significantly fewer parameters than the optimization of array filters. This is because geometry has limited com-

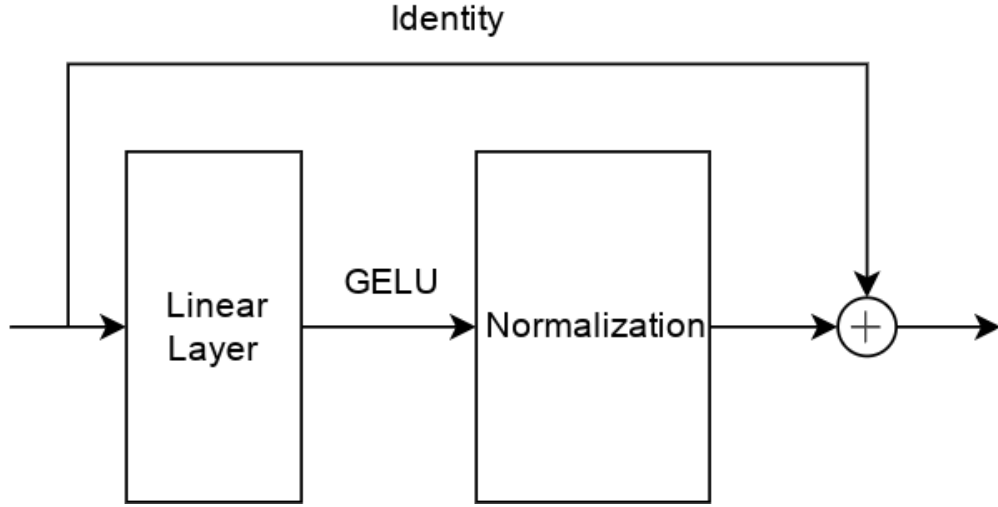


Figure 6.7: The diagram of a ResBlock.

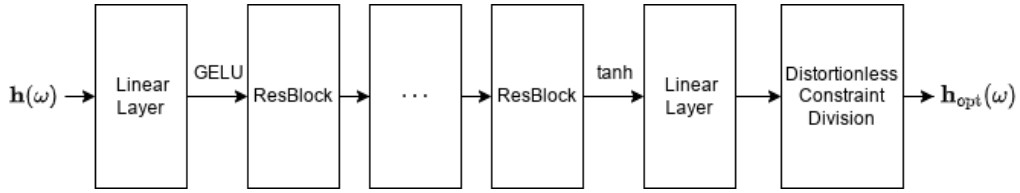


Figure 6.8: The diagram of FNet.

plexity on an x - y plane. The nonlinear activation functions adopted in the input linear layer and the hidden layer are Rectified Linear Units (ReLU) [124]. They are widely used in neural networks due to their simplicity and effectiveness. A ReLU function is expressed as:

$$\text{ReLU}(u) = \max(0, u), \quad (6.29)$$

where positive inputs are intact and negative inputs are converted to 0.

Different activation functions are used for various geometry scenarios after the output linear layer in GNet. For a linear array, a softmax function is applied, defined as:

$$\sigma(\mathbf{u})_i = \frac{e^{\mathbf{u}_i}}{\sum_{j=1}^{S-1} e^{\mathbf{u}_j}}, \quad (6.30)$$

where $\sigma(\cdot)$ is the softmax function, \mathbf{u} is the input latent embedding vector and u_i is its i th element. The softmax function has the desirable property that the sum of its elements is equal to 1. This property enables us to assign spacing between microphones based on the proportion of each element in the output vector. In other words, each element's value in the softmax function represents its relative position along the length of the linear array. A sigmoid function, defined as

$$\text{SIG}(u) = \frac{1}{1 + e^{-u}}, \quad (6.31)$$

is used for a UCCMA instead. As the sigmoid function's range is between 0 and 1, it can represent the proportion of an attribute by using its output, provided that the maximum value of the attribute is known. For instance, in a UCCMA, the angular position of the first microphone on a ring is at most $\frac{2\pi}{S}$, where S microphones are uniformly spaced. The angular position of the first microphone corresponds to a proportion of $\frac{2\pi}{S}$. The optimization of the radius of rings is another geometry parameter in a UCCMA, where the proportion of the maximum radius for different rings can also be optimized, given the maximum length of the radius is known.

6.5.1 Loss Function

For the convenience of presentation, we denote $\text{WNG}[\mathbf{h}(\omega)]$ by $f_i(\mathcal{X})$ and $\text{DF}[\mathbf{h}(\omega)]$ by $g_i(\mathcal{X})$, where i is the index of the frequency bin corresponding to ω . Assuming that the distortionless constraint is satisfied, we can formulate the optimization problem of our frequency-invariant beamformer as

$$\begin{aligned} \min \quad & \frac{1}{F} \sum_{i=1}^F f_i(\mathcal{X}) \\ \text{s.t.} \quad & \alpha_i \leq g_i(\mathcal{X}) \leq \beta_i, \quad i = 1, \dots, F, \end{aligned} \quad (6.32)$$

where F is the number of frequency bins, α_i and β_i are two-sided constraints of $g_i(\mathcal{X})$ with $\alpha_i < \beta_i$.

The augmented Lagrangian method is a powerful numerical optimization technique combining the Lagrangian function and a quadratic penalty function [135, 167]. It incorporates constraints and the objective into a single function, which is suitable to be a loss function of a neural network. It is more smooth and less ill-conditioned than using the penalty function directly [167]. We first write (6.32) in an equivalent form:

$$\begin{aligned} \min \frac{1}{F} \sum_{i=1}^F f_i(\mathcal{X}) \\ \text{s.t. } \alpha_i \leq g_i(\mathcal{X}) - u_i \leq \beta_i, \quad u_i = 0, \quad i = 1, \dots, F, \end{aligned} \quad (6.33)$$

Subsequently, (6.33) can be converted to \mathcal{L} [12]

$$\min \mathcal{L} = \frac{1}{F} \sum_{i=1}^F f_i(\mathcal{X}) + \sum_{i=1}^F p_i[g_i(\mathcal{X}), \mu_k^i, c_k^i], \quad i = 1, \dots, F. \quad (6.34)$$

where \mathcal{L} is the loss function of our neural network framework, μ_k^i is the i th Lagrangian multiplier in its k th iteration (see the iteration update rule in (6.38)), c_k^i is the i th penalty coefficient in its k th iteration and

$$p_i[g_i(\mathcal{X}), \mu_k^i, c_k^i] = \min_{\alpha_i \leq g_i(\mathcal{X}) - u_i \leq \beta_i} \left\{ \mu_k^i u_i + \frac{1}{2} c_k^i |u_i|^2 \right\}. \quad (6.35)$$

Analytically, we can obtain the optimal solution for (6.35)

$$u_k^i = \begin{cases} g_i(\mathcal{X}) - \beta_i & \text{if } \mu_k^i + c_k^i [g_i(\mathcal{X}) - \beta_i] > 0, \\ g_i(\mathcal{X}) - \alpha_i & \text{if } \mu_k^i + c_k^i [g_i(\mathcal{X}) - \alpha_i] < 0, \\ -\mu_k^i / c_k^i & \text{otherwise.} \end{cases} \quad (6.36)$$

Thus, (6.35) now becomes

$$\begin{aligned} p_i[g_i(\mathcal{X}), \mu_k^i, c_k^i] = \\ \begin{cases} \mu_k^i [g_i(\mathcal{X}) - \beta_i] + \frac{1}{2} c_k^i |g_i(\mathcal{X}) - \beta_i|^2 & \text{if } \mu_k^i + c_k^i [g_i(\mathcal{X}) - \beta_i] > 0, \\ \mu_k^i [g_i(\mathcal{X}) - \alpha_i] + \frac{1}{2} c_k^i |g_i(\mathcal{X}) - \alpha_i|^2 & \text{if } \mu_k^i + c_k^i [g_i(\mathcal{X}) - \alpha_i] < 0, \\ -(\mu_k^i)^2 / 2c_k^i & \text{otherwise.} \end{cases} \end{aligned} \quad (6.37)$$

The update rule for μ_k^i in the next iteration is

$$\mu_{k+1}^i = \begin{cases} \mu_k^i + c_k^i [g_i(\mathcal{X}) - \beta_i] & \text{if } \mu_k^i + c_k^i [g_i(\mathcal{X}) - \beta_i] > 0, \\ \mu_k^i + c_k^i [g_i(\mathcal{X}) - \alpha_i] & \text{if } \mu_k^i + c_k^i [g_i(\mathcal{X}) - \alpha_i] < 0, \\ 0 & \text{otherwise.} \end{cases} \quad (6.38)$$

The update rule for c_k^i in the next iteration is

$$c_{k+1}^i = \begin{cases} \max(\tilde{c}, 2c_k^i) & \text{if } g_i(\mathcal{X}) > \beta_i \text{ or } g_i(\mathcal{X}) < \alpha_i \\ c_k^i & \text{otherwise,} \end{cases} \quad (6.39)$$

where \tilde{c} is the maximum value for c_k^i .

6.6 Experiments

We conducted experiments on arrays with four different geometry scenarios: linear, circular, concentric circular and arbitrary discal. For the first three scenarios, we compared our approach with state-of-the-art frequency-invariant beamformers. Additionally, we demonstrated that our approach could obtain nearly global optimal solutions without any pre-specified geometry constraints for the arbitrary discal array.

6.6.1 Neural Network Training Details

The Adam optimizer [88] is used in all geometry scenarios. The learning rate is 0.00001. Early termination is applied if the loss decreases in the next evaluation. The gradient norm is clipped and the maximum gradient norm is 5. The parameters of the augmented Lagrangian in the first iteration are $\mu_0^i = 0$ and $c_0^i = 5$.

6.6.2 Linear Array

The linear array to be optimized has 16 microphones. The minimum spacing between microphones is set to 0.4 cm. The length of the array is 15

cm. The initial filter is obtained by applying a null-constrained method [6], with two nulls at 106° and 153° . The initial geometry is a uniform linear array. The FNet has 10 hidden layers. Each layer has 180 neurons. The loss is evaluated every 40000 epochs. Parameters of the augmented Lagrangian are updated in every 10000 epochs. The target DF value is 8.24 dB. With a tolerance of 0.1 dB, $\alpha_i = 8.14$ and $\beta_i = 8.34$. The frequency range is from 300 Hz to 8000 Hz. The look direction of the array is endfire.

The optimized geometry of the linear array is shown in Fig. 6.9. Three subarrays are formed to handle broadband signal processing in GONFB. The phenomenon that dense subarrays are in the middle of the array has been observed by another frequency-invariant linear array approach [85]. This middle subarray helps process higher frequency signals. In addition, our approach placed two smaller dense subarrays at both ends of the linear array. This novel design could potentially deal with lower frequency signals as well as optimizing WNGs. Similarly, three subarrays are also observed in the DMA approach, but the individual subarrays are not as dense. This could explain the inferior performance of DMAs as shown in Fig. 6.10, as more compact subarrays can better process high-frequency signals.

We compare the performance of our linear array with the DMA-based frequency-invariant nonuniform linear array described in [79], as shown in Fig. 6.10. We can observe that our approach has superior performance than the DMA-based approach in both DF and WNG values. This demonstrates that GONFB has found a more effective linear array geometry together with its filter.

6.6.3 Circular Array

The circular array to be optimized has 5 microphones. The radius of array is 1.5 cm. The initial filter is obtained in the same way as the linear array. The array geometry is fixed to a uniform circular array as shown in Fig.

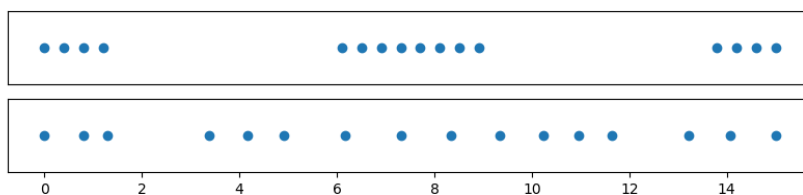


Figure 6.9: Optimized linear array geometry of GONFB (top) and DMA (bottom), when $M = 16$ and $L = 0.15$.

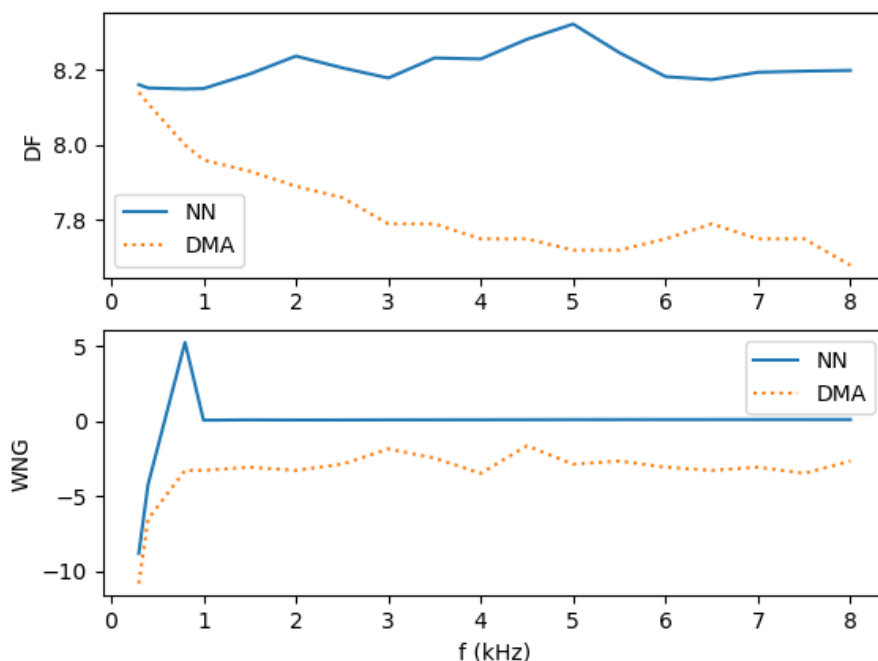


Figure 6.10: Performance of GONFB vs the DMA-based approach in a linear array.

6.11. Thus, we only train the FNet in this scenario. The FNet has 10 hidden layers. Each layer has 90 neurons. The loss is evaluated every 100000 epochs. Parameters of the augmented Lagrangian are updated in every 40000 epochs. The target DF value is 7.4 dB. α_i is set to the corresponding

DF value of [67]. $\beta_i = 7.4 + |7.4 - \alpha_i|$. The frequency range is from 100 Hz to 4000 Hz, as the compared DMA-based approach [67] can only be frequency-invariant below 4000 Hz. The direction of the incoming signal is 0° .

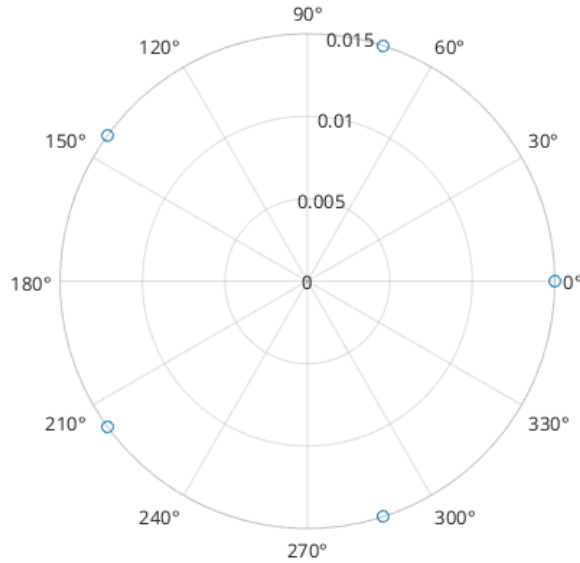


Figure 6.11: A uniform circular array geometry with $M = 5$ and $r = 0.015$. The look direction is 0° .

The performance comparison of our circular array with [67] is shown in Fig. 6.12. With the same geometry, our approach still exhibits superior performance in DF values, while our WNG values are either close to or slightly better than the WNGs in [67]. This shows that GONFB can not only provide better array geometry, but also optimizes the filter in a more flexible and effective manner.

6.6.4 Validation of ResBlocks Design

In ResBlocks, the benefits of identity mappings, also known as skip connections, are unknown in our beamforming tasks. As only FNet has Res-

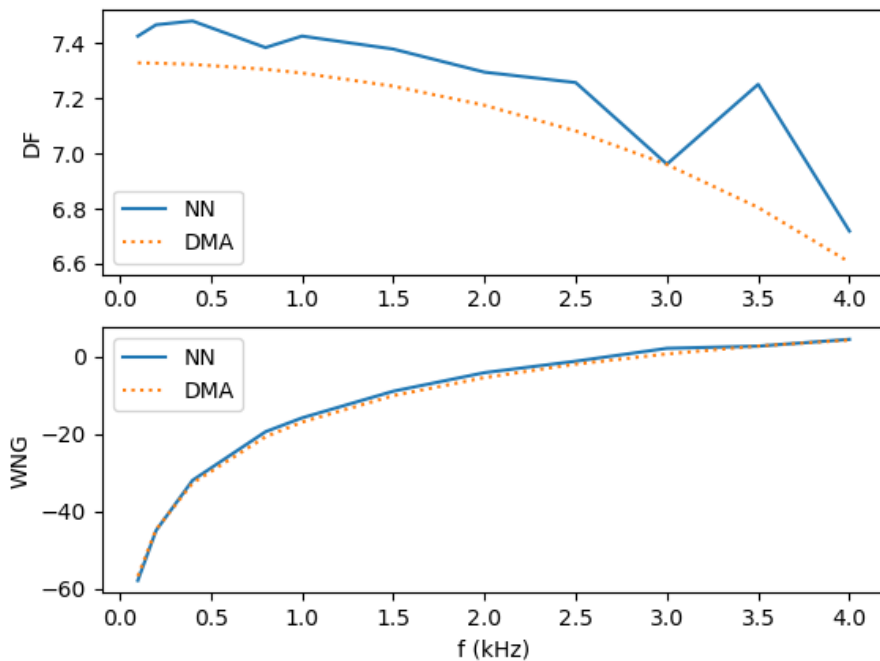


Figure 6.12: Performance of GONFB vs the DMA-based approach in a circular array.

Blocks, UCMA can serve as good testing scenarios where GNet is not involved. We performed experiments on a UCMA with 5 microphones to verify whether skip connections have positive effects on the optimization of beamforming filters. We used 15 hidden layers in FNet. Each layer had 40 neurons. The rest of the parameter settings followed the last subsection.

We ran experiments without skip connections for 10 times with different random seeds. The best performance without skip connections is picked and plotted against the performance with skip connections. As shown in Fig. 6.13, skip connections can improve DF and WNG performance slightly. Moreover, we observe that FNet without skip connections can sometimes fail to deliver good DF performance at certain frequencies. One of such experimental results is plotted in Fig. 6.14. Therefore, we

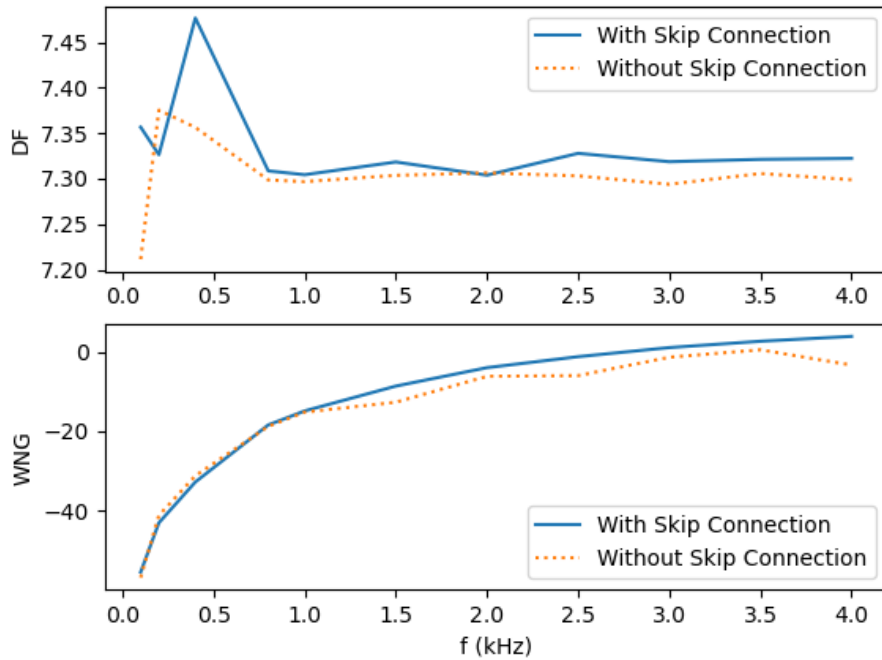


Figure 6.13: Performance of GONFB with and without skip connections in a circular array with 5 microphones. The best performance without skip connections from 10 experiments is hand-picked in this plot.

conclude that skip connections in ResBlocks have positive effects on the beamforming performance. Skip connections also make the optimization process more robust.

6.6.5 Concentric Circular Array

The concentric circular array to be optimized has 13 microphones in total. The initial geometry of the array consists of two rings. Each ring has 6 uniformly located microphones. One additional microphone is fixed at the centre of the array. The minimum radius of the inner ring is 1 cm and the maximum radius of the outer ring is 3 cm. The initial filter is

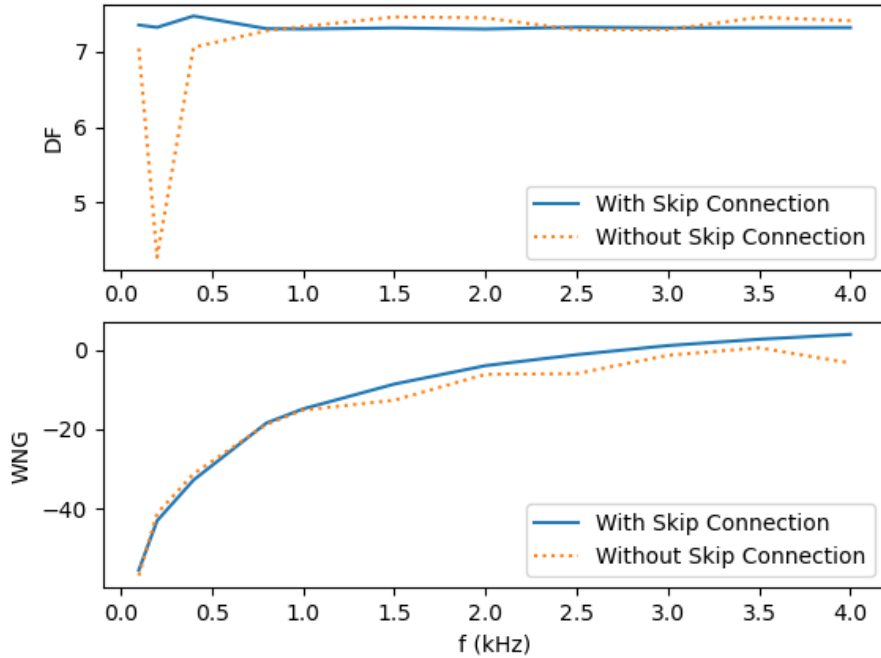


Figure 6.14: Performance of GONFB with and without skip connections in a circular array with 5 microphones. This plot shows one experiment where GONFB without skip connections fails to deliver good DF performance at certain frequency.

obtained by applying the null-constrained approach, with null directions at 102° and 174° . Before training, the angles of the starting microphones on the inner and outer rings are 30° and 0° respectively. In the GNet, the radius of each ring and the angular position of the first microphone on each ring are optimized. The FNet has 10 hidden layers. Each layer has 90 neurons. The loss is evaluated every 80000 epochs. Parameters of the augmented Lagrangian are updated in every 10000 epochs. The target DF value is 8.67 dB. α_i is set to the corresponding DF value of [67]. $\beta_i = 8.67 + |8.67 - \alpha_i|$. The frequency range is from 100 Hz to 8000 Hz. The direction of the incoming signal is 30° .

The optimized geometry of the concentric circular array is shown in Fig. 6.16. Contrary to the research finding in [165], our approach prefers to use only one ring instead of two rings. In other words, placing 12 microphones all in one ring can perform better than dividing microphones into two rings. The superior performance of two rings in [165] may be affected by the fact that the authors use 6 additional microphones in two rings.

We compare the performance of our UCCMA with the DMA-CCMA-II approach based on series expansions in [165], which is frequency-invariant. The performance plot can be seen in Fig. 6.15. Below 3 kHz, our approach has superior WNG values while maintaining comparable DF values. Conversely, beyond the 3 kHz mark, our approach excels in DF values while maintaining similar WNG values. This observation serves as an illustrative example of the inherent tradeoff between WNG and DF values. Furthermore, Fig. 6.15 demonstrates the efficacy GONFB in different geometry scenarios.

6.6.6 Arbitrary Discal Array

To explore the behaviour of GONFB in optimizing an arbitrary microphone array on a disc, we consider two straightforward scenarios: maximizing only WNG or maximizing only DF with two microphones. The minimum spacing between microphones is set to 0.5 cm. The radius of the disc is 3 cm. The initial filter is randomly sampled from a uniform distribution. The initial locations of the two microphones are at the intersections between the rim of the disc and the x -axis. The FNet has 10 hidden layers. Each layer has 90 neurons. The loss is evaluated every 80000 epochs. The frequency bin is 1000 Hz. As this is a not broadband scenario, we do not use the augmented Lagrangian in the loss function. Instead, the loss function maximizes (6.18) or (6.19). Additionally, a penalty term is appended in the loss function to ensure the minimum distance between the two microphones is not violated. The direction of the incoming signal is 30° .

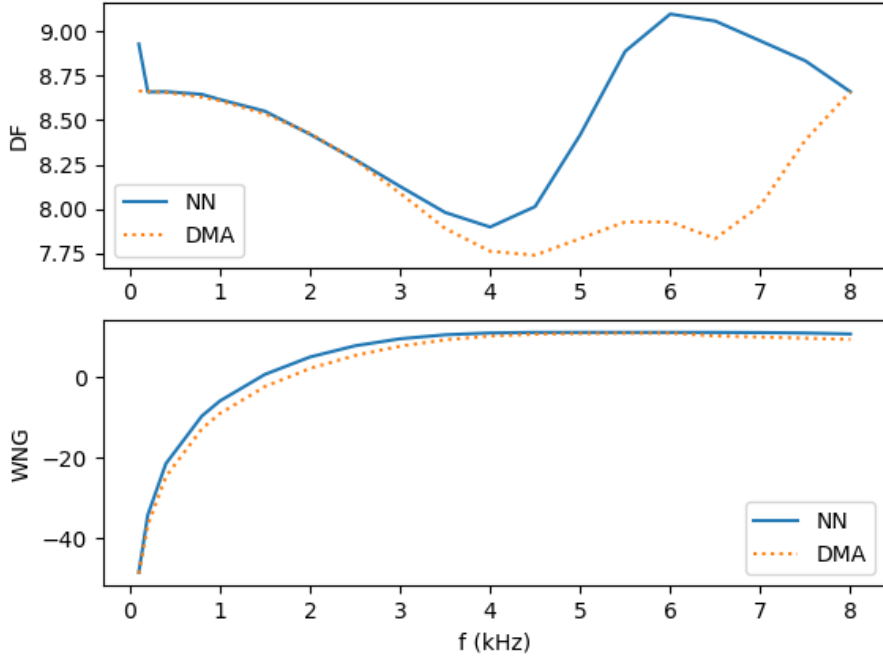


Figure 6.15: Performance of GONFB vs the DMA-based approach in a concentric circular array.

Two microphones will always form a linear array on a disc. The maximum WNG of a distortionless linear array is the number of microphones [10]. GONFB successfully finds the global optimum and obtains a WNG value of 2. As (6.18) does not require geometry information to maximize, the geometry shown in Fig. 6.17 is degenerate. In simpler terms, numerous viable geometric arrangements for a linear array on a disc can achieve the maximum WNG, provided the filter requirement is satisfied. The filter for the maximum WNG can be analytically derived as

$$\mathbf{h}(\omega) = \mathbf{d}_{AD}(\omega)/S. \quad (6.40)$$

The maximum DF of a distortionless linear array can also be analyti-

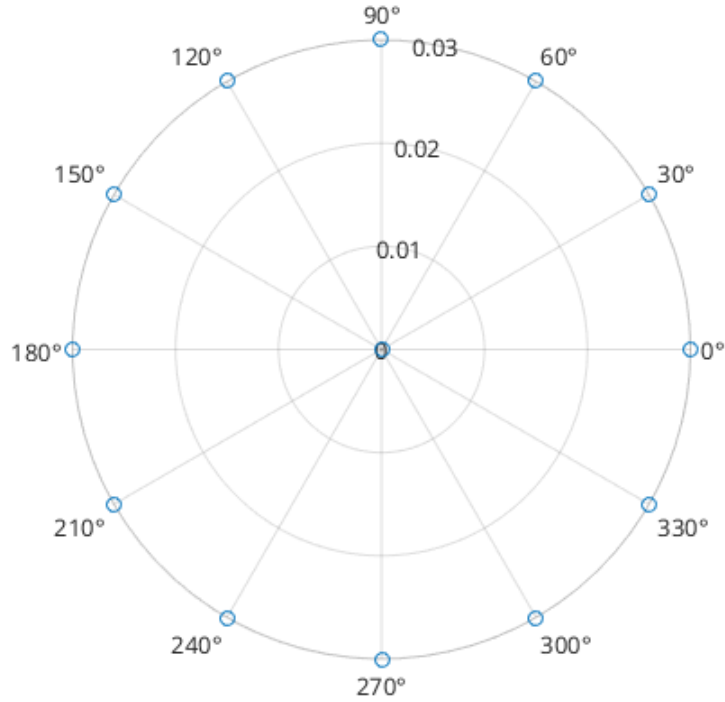


Figure 6.16: Optimized geometry for a uniform concentric circular array. 12 microphones in one ring and 1 additional microphone in the centre.

cally derived as [10]

$$DF[\mathbf{h}(\omega)]_{\max} = 2 \frac{1 - \text{sinc}(\omega\tau_0) \cos(\omega\tau_0 \cos \phi)}{1 - \text{sinc}^2(\omega\tau_0)}, \quad (6.41)$$

where τ_0 is the distance l_0 between two microphones divided by c . (6.41) indicates that ϕ should be 0 and l_0 should be as small as possible. From Fig. 6.18, we can see that the array aligns with the direction of the incoming signal. The distance between microphones is optimized to be the minimum distance. The DF value of the optimized array is numerically identical to the theoretical maximum DF value derived from (6.41). This means GONFB has also found the global optimum in this scenario.

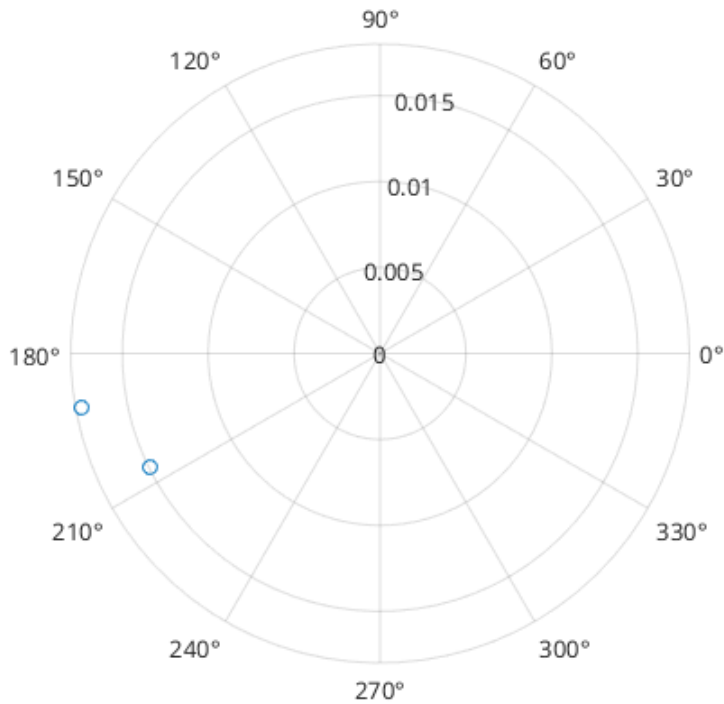


Figure 6.17: Geometry of two microphones when maximizing only WNG.

6.7 Conclusions

This chapter presented a novel and comprehensive framework for the neural optimization of fixed beamformers with varying geometries. The proposed neural network model, GONFB, successfully optimized both the array geometry and spatial filters of fixed beamformers. By leveraging the ResNet structure and incorporating an augmented Lagrangian-based loss function, GONFB surpassed DMA-based counterparts in linear, circular, and concentric circular arrays.

Our experimental results demonstrated that fixed beamformers designed by GONFB consistently exhibited superior DFs and WNGs across different frequency bins, while maintaining a desirable frequency-invariant property. Remarkably, we discovered that GONFB could effectively design

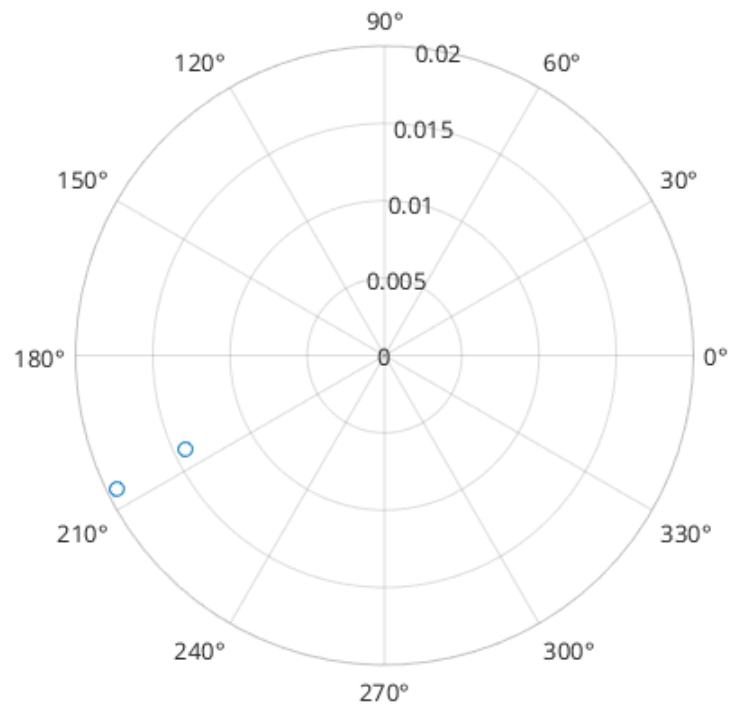


Figure 6.18: Optimized Geometry of two microphones when maximizing only DF.

CCMAs using only two rings. Furthermore, we explored the capabilities of GONFB in an arbitrary discal geometric setting, achieving globally optimal solutions. These findings highlight the versatility and robustness of GONFB in various array configurations.

Overall, this unified framework and the GONFB model presented in this chapter offer significant advancements in the field of neural optimization for fixed beamformers. The results demonstrate their potential for practical applications and further research in array signal processing.

Chapter 7

Conclusions and Future Research

This chapter provides an overview of the contributions presented in this thesis. It outlines the key findings and advancements made throughout the research. The chapter concludes by presenting a list of possible avenues for further exploration that can emerge from the valuable insights gained through this research.

7.1 Conclusions

In this section, we provide a comprehensive summary of the major contributions presented in this thesis. Firstly, we introduce a novel linear-time independence criterion in Chapter 3, known as FBIC. FBIC serves as an estimation of the Hirschfeld-Gebelein-Rényi maximum correlation coefficient and proves to be highly effective in guiding an ICA algorithm for signal separation. Notably, compared to kernel-based independence criteria, FBIC exhibits superior computational efficiency without compromising effectiveness.

Secondly, we conduct an in-depth analysis of the impact of phase errors on the robustness of first-order linear DMAs in Chapter 4. Through this analysis, we mathematically derive the WNG thresholds that prevent misorientation of the mainlobe in arrays. These WNG thresholds provide

valuable insights, indicating that deploying a greater number of microphones with larger spacing significantly enhances the robustness of the microphone array.

Thirdly, in Chapter 5, we propose an innovative fixed beamformer model based on neural networks, specifically designed to optimize the geometry of a linear microphone array. Moreover, we extend this model to encompass general geometric configurations by leveraging ResNets and augmented Lagrangian techniques in Chapter 6. The proposed model surpasses the performance of previous DMA-based approaches by a considerable margin, showcasing its efficacy in practical applications. This suggests that fixed beamformers with automatically designed beampatterns and array geometries using neural networks offer distinct advantages over their counterparts designed based on human expertise.

Collectively, these contributions significantly advance the signal enhancement field by introducing the FBIC for ICA, analyzing the impact of phase errors on DMAs, and developing a state-of-the-art fixed beamformer model based on neural networks. The findings and methodologies presented in this thesis contribute to the broader understanding of signal separation, extraction and suppression, with implications for various domains and applications. We firmly believe that our contributions will have a lasting impact and pave the way for the next generation of applications in BSS and fixed beamforming tasks.

7.2 Future Work

In this section, we discuss three possible directions for future works below.

7.2.1 Multi-channel Speech Separation Guided by Independence Criteria

In recent years, deep learning approaches, specifically Deep Neural Networks (DNNs), have emerged as the prevailing method for addressing multichannel audio source separation [110, 163, 162]. These approaches treat the task of multichannel audio source separation as a supervised learning problem, where acoustic features are acquired through training data [163]. One approach to accomplish this is through Ideal Binary Mask (IBM) classification, which translates the estimation of masks for each time-frequency unit into a binary classification problem [21]. Another approach involves estimating the target magnitude spectrogram instead of masks [169]. Many neural network models have been proposed to tackle audio source separation, such as Wave-U-Net [154], Multichannel Variational Autoencoder (MVAE) [82], and Multi-Resolution Convolutional Auto-Encoder (MRCAE) neural networks [51]. However, supervised learning approaches suffer from the mismatch between the training data and the real environment in which they are deployed. In contrast, unsupervised learning approaches are not reliant on the training data for their performance [126]. The FBIC proposed in this thesis has the potential to be employed in similar unsupervised multichannel speech separation algorithms, utilizing the independence criterion as a metric to separate speeches from different speakers.

7.2.2 Disentanglement

Signal separation techniques play a crucial role not only in the separation of audio sources but also in understanding data representation in machine learning. Disentangling explanatory factors can greatly benefit from employing signal separation techniques such as Blind Source Separation (BSS). In their work, Bengio et al. [11] emphasized the significance of disentangling underlying explanatory factors from directly observed

input signals for the success of Artificial Intelligence (AI). These factors, when effectively utilized, can enhance the performance of machine learning models and facilitate generalization by leveraging shared subsets of explanatory factors across different tasks. Mutual information has been the most commonly used metric for achieving disentanglement. However, it is worth exploring whether the proposed FBIC method can outperform mutual information in disentanglement tasks, given its superior performance exhibited in ICA tasks.

7.2.3 Fixed Beamforming with Rectangular Arrays

Having established a comprehensive neural network framework GONFB for optimizing microphone arrays with arbitrary geometries, it is logical to extend the application of this framework to other existing geometric configurations, including rectangular arrays. Rectangular arrays have been demonstrated to be beneficial for direction-of-arrival estimation tasks [180]. In order to evaluate the performance of the fixed beamformer generated by our model, a comparison can be made with the beamformer obtained using the Kronecker-product (KP) [76]. The KP approach enables the decomposition of a global beamformer into independent sub-beamformers, which can be individually optimized. Furthermore, GONFB can be applied to more practical scenarios, such as designing an optimal microphone array for a smart phone with a predetermined shape.

Bibliography

- [1] AMARI, S.-I., CICHOCKI, A., AND YANG, H. H. A new learning algorithm for blind signal separation. In *Advances in neural information processing systems* (1996), pp. 757–763.
- [2] ARCONES, M. A., AND GINE, E. On the bootstrap of u and v statistics. *The Annals of Statistics* (1992), 655–674.
- [3] BACH, F. R., AND JORDAN, M. I. Kernel independent component analysis. *Journal of machine learning research* 3, Jul (2002), 1–48.
- [4] BAHARI, M. H., BERTRAND, A., AND MOONEN, M. Blind sampling rate offset estimation for wireless acoustic sensor networks through weighted least-squares coherence drift estimation. *IEEE/ACM Transactions on Audio, Speech, and Language Processing* 25, 3 (2017), 674–686.
- [5] BELL, A. J., AND SEJNOWSKI, T. J. An information-maximization approach to blind separation and blind deconvolution. *Neural computation* 7, 6 (1995), 1129–1159.
- [6] BENESTY, J., AND CHEN, J. *Study and design of differential microphone arrays*, vol. 6. Springer Science & Business Media, 2012.
- [7] BENESTY, J., CHEN, J., AND COHEN, I. *Design of circular differential microphone arrays*, vol. 12. Springer, 2015.
- [8] BENESTY, J., CHEN, J., AND HUANG, Y. *Microphone array signal processing*, vol. 1. Springer Science & Business Media, 2008.

- [9] BENESTY, J., CHEN, J., AND PAN, C. *Fundamentals of differential beamforming*. Springer, 2016.
- [10] BENESTY, J., COHEN, I., AND CHEN, J. *Fundamentals of signal enhancement and array signal processing*. John Wiley & Sons, 2017.
- [11] BENGIO, Y., COURVILLE, A., AND VINCENT, P. Representation learning: A review and new perspectives. *IEEE transactions on pattern analysis and machine intelligence* 35, 8 (2013), 1798–1828.
- [12] BERTSEKAS, D. P., ET AL. *Constrained optimization and lagrange multiplier methods*. Belmont: Athena Scientific,, 1996.
- [13] BORRA, F., BERNARDINI, A., ANTONACCI, F., AND SARTI, A. Uniform linear arrays of first-order steerable differential microphones. *IEEE/ACM Transactions on Audio, Speech, and Language Processing* 27, 12 (2019), 1906–1918.
- [14] BREIMAN, L., AND FRIEDMAN, J. H. Estimating optimal transformations for multiple regression and correlation. *Journal of the American statistical Association* 80, 391 (1985), 580–598.
- [15] BUCHRIS, Y., COHEN, I., AND BENESTY, J. First-order differential microphone arrays from a time-domain broadband perspective. In *2016 IEEE International Workshop on Acoustic Signal Enhancement (IWAENC)* (2016), IEEE, pp. 1–5.
- [16] BUCK, M. Aspects of first-order differential microphone arrays in the presence of sensor imperfections. *European transactions on telecommunications* 13, 2 (2002), 115–122.
- [17] BUENO LARRAZ, B. Independence measures. Master’s thesis, Universidad Autónoma de Madrid, Escuela Politécnica Superior, Spain, 2015.

- [18] CARDOSO, J.-F., AND SOULOUMIAC, A. Blind beamforming for non-Gaussian signals. In *IEE proceedings F (radar and signal processing)* (1993), vol. 140, IET, pp. 362–370.
- [19] CHEN, A., AND BICKEL, P. J. Consistent independent component analysis and prewhitening. *IEEE Transactions on Signal Processing* 53, 10 (2005), 3625–3632.
- [20] CHEN, J., BENESTY, J., AND PAN, C. On the design and implementation of linear differential microphone arrays. *The Journal of the Acoustical Society of America* 136, 6 (2014), 3097–3113.
- [21] CHEN, J., AND WANG, D. Dnn based mask estimation for supervised speech separation. In *Audio source separation*. Springer, 2018, pp. 207–235.
- [22] CHEN, R. T., LI, X., GROSSE, R., AND DUVENAUD, D. Isolating sources of disentanglement in vaes. In *Proceedings of the 32nd International Conference on Neural Information Processing Systems* (2018), vol. 2615, p. 2625.
- [23] CHEN, R. T., RUBANOVA, Y., BETTENCOURT, J., AND DUVENAUD, D. K. Neural ordinary differential equations. *Advances in neural information processing systems* 31 (2018).
- [24] CHEN, Z., CHEN, H., AND TU, Q. Sensor imperfection tolerance analysis of robust linear differential microphone arrays. *IEEE/ACM Transactions on Audio, Speech, and Language Processing* 29 (2021), 2915–2929.
- [25] CHERRY, E. C. Some experiments on the recognition of speech, with one and with two ears. *The Journal of the acoustical society of America* 25, 5 (1953), 975–979.

- [26] CHIANDUSSI, G., CODEGONE, M., FERRERO, S., AND VAREGIO, F. E. Comparison of multi-objective optimization methodologies for engineering applications. *Computers & Mathematics with Applications* 63, 5 (2012), 912–942.
- [27] CHINAEV, A., ENZNER, G., GBURREK, T., AND SCHMALENSTROEER, J. Online estimation of sampling rate offsets in wireless acoustic sensor networks with packet loss. In *2021 29th European Signal Processing Conference (EUSIPCO) (2021)*, IEEE, pp. 1110–1114.
- [28] CHWIALKOWSKI, K. P., RAMDAS, A., SEJDINOVIC, D., AND GRETTON, A. Fast two-sample testing with analytic representations of probability measures. In *Advances in Neural Information Processing Systems* (2015), pp. 1981–1989.
- [29] COMON, P. Independent component analysis, a new concept? *Signal processing* 36, 3 (1994), 287–314.
- [30] COMON, P., AND JUTTEN, C. *Handbook of Blind Source Separation: Independent component analysis and applications*. Academic press, 2010.
- [31] CROCCO, M., AND TRUCCO, A. Stochastic and analytic optimization of sparse aperiodic arrays and broadband beamformers with robust superdirective patterns. *IEEE Transactions on audio, speech, and language processing* 20, 9 (2012), 2433–2447.
- [32] CYBENKO, G. Approximation by superpositions of a sigmoidal function. *Mathematics of control, signals and systems* 2, 4 (1989), 303–314.
- [33] DANIUŠIS, P., AND VAITKUS, P. Supervised feature extraction using hilbert-schmidt norms. In *Intelligent Data Engineering and Automated Learning-IDEAL 2009: 10th International Conference, Burgos, Spain, September 23-26, 2009. Proceedings 10* (2009), Springer, pp. 25–33.

- [34] DE SENA, E., HACIHABIBOGLU, H., AND CVETKOVIC, Z. On the design and implementation of higher order differential microphones. *IEEE Transactions on Audio, Speech, and Language Processing* 20, 1 (2011), 162–174.
- [35] DING, Z., CHEN, S., LI, Q., AND WRIGHT, S. On the global convergence of gradient descent for multi-layer resnets in the mean-field regime. *arXiv preprint arXiv:2110.02926* (2021).
- [36] DING, Z., CHEN, S., LI, Q., AND WRIGHT, S. J. Overparameterization of deep resnet: zero loss and mean-field analysis. *Journal of machine learning research* (2022).
- [37] DOCLO, S., AND MOONEN, M. Superdirective beamforming robust against microphone mismatch. In *2006 IEEE International Conference on Acoustics Speech and Signal Processing Proceedings* (2006), vol. 5, IEEE, pp. V–V.
- [38] DUMOULIN, V., AND VISIN, F. A guide to convolution arithmetic for deep learning. *arXiv preprint arXiv:1603.07285* (2016).
- [39] ELKO, G. W. Microphone array systems for hands-free telecommunication. *Speech communication* 20, 3-4 (1996), 229–240.
- [40] ELKO, G. W. Superdirectional microphone arrays. In *Acoustic signal processing for telecommunication*. Springer, 2000, pp. 181–237.
- [41] ELKO, G. W. Differential microphone arrays. In *Audio signal processing for next-generation multimedia communication systems*. Springer, 2004, pp. 11–65.
- [42] GBURREK, T., SCHMALENSTROEER, J., AND HAEB-UMBACH, R. Geometry calibration in wireless acoustic sensor networks utilizing doa and distance information. *EURASIP Journal on Audio, Speech, and Music Processing* 2021, 1 (2021), 1–17.

- [43] GBURREK, T., SCHMALENSTROEER, J., AND HAEB-UMBACH, R. On synchronization of wireless acoustic sensor networks in the presence of time-varying sampling rate offsets and speaker changes. In *ICASSP 2022-2022 IEEE International Conference on Acoustics, Speech and Signal Processing (ICASSP)* (2022), IEEE, pp. 916–920.
- [44] GEBELEIN, H. Das statistische problem der korrelation als variations-und eigenwertproblem und sein zusammenhang mit der ausgleichsrechnung. *ZAMM-Journal of Applied Mathematics and Mechanics/Zeitschrift für Angewandte Mathematik und Mechanik* 21, 6 (1941), 364–379.
- [45] GENTZSCH, W. Sun grid engine: Towards creating a compute power grid. In *Proceedings First IEEE/ACM International Symposium on Cluster Computing and the Grid* (2001), IEEE, pp. 35–36.
- [46] GILBERT, E., AND MORGAN, S. Optimum design of directive antenna arrays subject to random variations. *Bell System Technical Journal* 34, 3 (1955), 637–663.
- [47] GOLUB, G. H., AND REINSCH, C. Singular value decomposition and least squares solutions. In *Linear Algebra*. Springer, 1971, pp. 134–151.
- [48] GOODFELLOW, I., BENGIO, Y., AND COURVILLE, A. *Deep learning*. MIT press, 2016.
- [49] GOODFELLOW, I., POUGET-ABADIE, J., MIRZA, M., XU, B., WARDE-FARLEY, D., OZAIR, S., COURVILLE, A., AND BENGIO, Y. Generative adversarial networks. *Communications of the ACM* 63, 11 (2020), 139–144.
- [50] GORDON, C., AND PARDE, N. Latent neural differential equations for video generation. In *NeurIPS 2020 Workshop on Pre-registration in Machine Learning* (2021), PMLR, pp. 73–86.

- [51] GRAIS, E. M., WARD, D., AND PLUMBLY, M. D. Raw multi-channel audio source separation using multi-resolution convolutional auto-encoders. In *2018 26th European Signal Processing Conference (EUSIPCO)* (2018), IEEE, pp. 1577–1581.
- [52] GRARI, V. *Adversarial mitigation to reduce unwanted biases in machine learning*. PhD thesis, Sorbonne université, 2022.
- [53] GRAVES, A. Generating sequences with recurrent neural networks. *arXiv preprint arXiv:1308.0850* (2013).
- [54] GRETTON, A., BORGWARDT, K. M., RASCH, M. J., SCHÖLKOPF, B., AND SMOLA, A. A kernel two-sample test. *Journal of Machine Learning Research* 13, Mar (2012), 723–773.
- [55] GRETTON, A., BOUSQUET, O., SMOLA, A., AND SCHÖLKOPF, B. Measuring statistical dependence with Hilbert-Schmidt norms. In *International conference on algorithmic learning theory* (2005), Springer, pp. 63–77.
- [56] GRETTON, A., HERBRICH, R., AND SMOLA, A. J. The kernel mutual information. In *2003 IEEE International Conference on Acoustics, Speech, and Signal Processing, 2003. Proceedings.(ICASSP'03)*. (2003), vol. 4, IEEE, pp. IV–880.
- [57] GRETTON, A., SMOLA, A. J., BOUSQUET, O., HERBRICH, R., BELITSKI, A., AUGATH, M., MURAYAMA, Y., PAULS, J., SCHÖLKOPF, B., AND LOGOTHETIS, N. K. Kernel constrained covariance for dependence measurement. In *AISTATS* (2005), vol. 10, pp. 112–119.
- [58] GRIFFITHS, L., AND JIM, C. An alternative approach to linearly constrained adaptive beamforming. *IEEE Transactions on antennas and propagation* 30, 1 (1982), 27–34.

- [59] HE, K., ZHANG, X., REN, S., AND SUN, J. Deep residual learning for image recognition. In *Proceedings of the IEEE conference on computer vision and pattern recognition* (2016), pp. 770–778.
- [60] HENDRYCKS, D., AND GIMPEL, K. Gaussian error linear units (gelus). *arXiv preprint arXiv:1606.08415* (2016).
- [61] HERBORDT, W., HORIUCHI, T., FUJIMOTO, M., JITSUHIRO, T., AND NAKAMURA, S. Hands-free speech recognition and communication on pdas using microphone array technology. In *IEEE Workshop on Automatic Speech Recognition and Understanding, 2005.* (2005), IEEE, pp. 302–307.
- [62] HIGGINS, I., MATTHEY, L., PAL, A., BURGESS, C., GLOROT, X., BOTVINICK, M., MOHAMED, S., AND LERCHNER, A. beta-vae: Learning basic visual concepts with a constrained variational framework. In *International conference on learning representations* (2016).
- [63] HIRSCHFELD, H. O. A connection between correlation and contingency. In *Mathematical Proceedings of the Cambridge Philosophical Society* (1935), vol. 31, Cambridge University Press, pp. 520–524.
- [64] HOCHREITER, S., AND SCHMIDHUBER, J. Long short-term memory. *Neural computation* 9, 8 (1997), 1735–1780.
- [65] HOSHUYAMA, O., SUGIYAMA, A., AND HIRANO, A. A robust adaptive beamformer for microphone arrays with a blocking matrix using constrained adaptive filters. *IEEE Transactions on signal processing* 47, 10 (1999), 2677–2684.
- [66] HUANG, G., BENESTY, J., AND CHEN, J. Design of robust concentric circular differential microphone arrays. *The Journal of the Acoustical Society of America* 141, 5 (2017), 3236–3249.

- [67] HUANG, G., BENESTY, J., AND CHEN, J. On the design of frequency-invariant beampatterns with uniform circular microphone arrays. *IEEE/ACM Transactions on Audio, Speech, and Language Processing* 25, 5 (2017), 1140–1153.
- [68] HUANG, G., BENESTY, J., AND CHEN, J. Fundamental approaches to robust differential beamforming with high directivity factors. *IEEE/ACM Transactions on Audio, Speech, and Language Processing* 30 (2022), 3074–3088.
- [69] HUANG, G., BENESTY, J., COHEN, I., AND CHEN, J. A simple theory and new method of differential beamforming with uniform linear microphone arrays. *IEEE/ACM Transactions on Audio, Speech, and Language Processing* 28 (2020), 1079–1093.
- [70] HUANG, G., CHEN, J., AND BENESTY, J. Insights into frequency-invariant beamforming with concentric circular microphone arrays. *IEEE/ACM Transactions on Audio, Speech, and Language Processing* 26, 12 (2018), 2305–2318.
- [71] HUANG, G., CHEN, J., AND BENESTY, J. On the design of robust steerable frequency-invariant beampatterns with concentric circular microphone arrays. In *2018 IEEE International Conference on Acoustics, Speech and Signal Processing (ICASSP)* (2018), IEEE, pp. 506–510.
- [72] HUANG, W., AND FENG, J. Differential beamforming for uniform circular array with directional microphones. In *INTERSPEECH* (2020), pp. 71–75.
- [73] HUANG, W., AND FENG, J. Minimum-norm differential beamforming for linear array with directional microphones. In *Interspeech* (2021), pp. 701–705.
- [74] HUANG, W., AND FENG, J. Robust steerable differential beamformer for concentric circular array with directional microphones.

- In *2022 Asia-Pacific Signal and Information Processing Association Annual Summit and Conference (APSIPA ASC) (2022)*, IEEE, pp. 319–323.
- [75] HYVARINEN, A. Fast and robust fixed-point algorithms for independent component analysis. *IEEE transactions on Neural Networks* 10, 3 (1999), 626–634.
- [76] ITZHAK, G., AND COHEN, I. Differential and constant-beamwidth beamforming with uniform rectangular arrays. In *2022 International Workshop on Acoustic Signal Enhancement (IWAENC) (2022)*, IEEE, pp. 1–5.
- [77] JACKSON, D. A proof of weierstrass’s theorem. *The American Mathematical Monthly* 41, 5 (1934), 309–312.
- [78] JIN, J., BENESTY, J., HUANG, G., AND CHEN, J. On differential beamforming with nonuniform linear microphone arrays. *IEEE/ACM Transactions on Audio, Speech, and Language Processing* 30 (2022), 1840–1852.
- [79] JIN, J., HUANG, G., CHEN, J., AND BENESTY, J. Design of optimal linear differential microphone arrays based array geometry optimization. In *2019 IEEE International Conference on Acoustics, Speech and Signal Processing (ICASSP) (2019)*, IEEE, pp. 5741–5745.
- [80] JIN, W., TAGHIZADEH, M. J., CHEN, K., AND XIAO, W. Multi-channel noise reduction for hands-free voice communication on mobile phones. In *2017 IEEE International Conference on Acoustics, Speech and Signal Processing (ICASSP) (2017)*, IEEE, pp. 506–510.
- [81] JITKRITTUM, W., SZABÓ, Z., AND GRETTON, A. An adaptive test of independence with analytic kernel embeddings. In *Proceedings of the 34th International Conference on Machine Learning-Volume 70 (2017)*, JMLR. org, pp. 1742–1751.

- [82] KAMEOKA, H., LI, L., INOUE, S., AND MAKINO, S. Semi-blind source separation with multichannel variational autoencoder. *arXiv preprint arXiv:1808.00892* (2018).
- [83] KARUSH, W. Minima of functions of several variables with inequalities as side constraints. *M. Sc. Dissertation. Dept. of Mathematics, Univ. of Chicago* (1939).
- [84] KENNEDY, J., AND EBERHART, R. Particle swarm optimization. In *Proceedings of ICNN'95-international conference on neural networks* (1995), vol. 4, IEEE, pp. 1942–1948.
- [85] KENNEDY, R. A., ABHAYAPALA, T. D., AND WARD, D. B. Broadband nearfield beamforming using a radial beampattern transformation. *IEEE Transactions on Signal Processing* 46, 8 (1998), 2147–2156.
- [86] KIDGER, P., MORRILL, J., FOSTER, J., AND LYONS, T. Neural controlled differential equations for irregular time series. *Advances in Neural Information Processing Systems* 33 (2020), 6696–6707.
- [87] KIM, H., AND MNIH, A. Disentangling by factorising. In *International Conference on Machine Learning* (2018), PMLR, pp. 2649–2658.
- [88] KINGMA, D. P., AND BA, J. Adam: A method for stochastic optimization. *arXiv preprint arXiv:1412.6980* (2014).
- [89] KINGMA, D. P., MOHAMED, S., REZENDE, D. J., AND WELLING, M. Semi-supervised learning with deep generative models. In *Advances in neural information processing systems* (2014), pp. 3581–3589.
- [90] KINGMA, D. P., AND WELLING, M. Auto-encoding variational bayes. *arXiv preprint arXiv:1312.6114* (2013).
- [91] KINNEY, J. B., AND ATWAL, G. S. Equitability, mutual information, and the maximal information coefficient. *Proceedings of the National Academy of Sciences* 111, 9 (2014), 3354–3359.

- [92] KITAMURA, D., ONO, N., SAWADA, H., KAMEOKA, H., AND SARUWATARI, H. Determined blind source separation with independent low-rank matrix analysis. In *Audio Source Separation*. Springer, 2018, pp. 125–155.
- [93] KOFIDIS, E. Blind source separation: Fundamentals and recent advances. *Mini-curso no XIX Simpósio Brasileiro de Telecomunicações (SBrT 2001), Fortaleza-CE, Setembro (2001)*.
- [94] KOLMOGOROV, A. N., AND FOMIN, S. V. *Elements of the theory of functions and functional analysis*. Academic Press, 1961.
- [95] KONFORTI, Y., COHEN, I., AND BERDUGO, B. Array geometry optimization for region-of-interest broadband beamforming. In *2022 17th International Workshop on Acoustic Signal Enhancement (IWAENC) (2022)*, IEEE.
- [96] KONFORTI, Y., COHEN, I., AND BERDUGO, B. Array geometry optimization for region-of-interest broadband beamforming. In *2022 International Workshop on Acoustic Signal Enhancement (IWAENC) (2022)*, pp. 1–5.
- [97] KRASKOV, A., STÖGBAUER, H., AND GRASSBERGER, P. Estimating mutual information. *Physical review E* 69, 6 (2004), 066138.
- [98] KROGH, A., AND HERTZ, J. A simple weight decay can improve generalization. *Advances in neural information processing systems* 4 (1991).
- [99] KUHN, H. W., AND TUCKER, A. W. Nonlinear programming, in (j. neyman, ed.) *proceedings of the second berkeley symposium on mathematical statistics and probability*, 1951.
- [100] KULLBACK, S. *Information theory and statistics*. Courier Corporation, 1997.

- [101] KUMATANI, K., MCDONOUGH, J., AND RAJ, B. Microphone array processing for distant speech recognition: From close-talking microphones to far-field sensors. *IEEE Signal Processing Magazine* 29, 6 (2012), 127–140.
- [102] LEARNED-MILLER, E. G., AND JOHN III, W. F. Ica using spacings estimates of entropy. *Journal of machine learning research* 4, Dec (2003), 1271–1295.
- [103] LECUN, Y., BOTTOU, L., BENGIO, Y., AND HAFFNER, P. Gradient-based learning applied to document recognition. *Proceedings of the IEEE* 86, 11 (1998), 2278–2324.
- [104] LIU, W., AND WEISS, S. *Wideband beamforming: concepts and techniques*. John Wiley & Sons, 2010.
- [105] LUO, X., HUANG, G., JIN, J., CHEN, J., BENESTY, J., ZHANG, W., ZHU, M., AND LI, C. Design of maximum directivity beamformers with linear acoustic vector sensor arrays. *IEEE/ACM Transactions on Audio, Speech, and Language Processing* 31 (2023), 1421–1435.
- [106] LUO, X., JIN, J., HUANG, G., CHEN, J., AND BENESTY, J. Design of steerable linear differential microphone arrays with omnidirectional and bidirectional sensors. *IEEE Signal Processing Letters* 30 (2023), 463–467.
- [107] LUO, X., JIN, J., HUANG, G., CHEN, J., BENESTY, J., COHEN, I., AND ZHANG, W. Constrained maximum directivity beamformers based on uniform linear acoustic vector sensor arrays. In *2021 Asia-Pacific Signal and Information Processing Association Annual Summit and Conference (APSIPA ASC)* (2021), pp. 1221–1225.
- [108] MA, F., ABHAYAPALA, T. D., AND SAMARASINGHE, P. N. A time-domain nearfield frequency-invariant beamforming method. *arXiv preprint arXiv:2105.08219* (2021).

- [109] MA, W.-D. K., LEWIS, J., AND KLEIJN, W. B. The hsic bottleneck: Deep learning without back-propagation. In *Proceedings of the AAAI conference on artificial intelligence* (2020), vol. 34, pp. 5085–5092.
- [110] MAKINO, S. *Audio Source Separation*. Springer, 2018.
- [111] MAKINO, S., LEE, T.-W., AND SAWADA, H. *Blind Speech Separation (Signals and Communication Technology)*. Springer Netherlands, 2007.
- [112] MATTHÈS, M. W., BROMBERG, Y., DE ROSNY, J., AND POPOFF, S. M. Learning and avoiding disorder in multimode fibers. *Physical Review X* 11, 2 (2021), 021060.
- [113] MCCULLOCH, W. S., AND PITTS, W. A logical calculus of the ideas immanent in nervous activity. *The bulletin of mathematical biophysics* 5 (1943), 115–133.
- [114] MEYER, J. Beamforming for a circular microphone array mounted on spherically shaped objects. *The Journal of the Acoustical Society of America* 109, 1 (2001), 185–193.
- [115] MICHAEL, R., AND BARRY, S. *Methods of modern mathematical physics*, 1975.
- [116] MILJANOVIC, M. Comparative analysis of recurrent and finite impulse response neural networks in time series prediction. *Indian Journal of Computer Science and Engineering* 3, 1 (2012), 180–191.
- [117] MIRANDA, L. J. V. PySwarms, a research-toolkit for Particle Swarm Optimization in Python. *Journal of Open Source Software* 3 (2018).
- [118] MONGILLO, M. Choosing basis functions and shape parameters for radial basis function methods. *SIAM undergraduate research online* 4, 190-209 (2011), 2–6.

- [119] MOON, Y.-I., RAJAGOPALAN, B., AND LALL, U. Estimation of mutual information using kernel density estimators. *Physical Review E* 52, 3 (1995), 2318.
- [120] MÓRI, T. F., AND SZÉKELY, G. J. Four simple axioms of dependence measures. *Metrika* 82, 1 (2019), 1–16.
- [121] MROUEH, Y., SERCU, T., RIGOTTI, M., PADHI, I., AND NOGUEIRA DOS SANTOS, C. Sobolev independence criterion. *Advances in Neural Information Processing Systems* 32 (2019).
- [122] MÜLLER, A. Integral probability metrics and their generating classes of functions. *Advances in Applied Probability* 29, 2 (1997), 429–443.
- [123] NAIK, G. R., WANG, W., ET AL. *Blind source separation*. Springer, 2014.
- [124] NAIR, V., AND HINTON, G. E. Rectified linear units improve restricted boltzmann machines. In *Proceedings of the 27th international conference on machine learning (ICML-10)* (2010), pp. 807–814.
- [125] NGUYEN, X., WAINWRIGHT, M. J., AND JORDAN, M. I. Estimating divergence functionals and the likelihood ratio by convex risk minimization. *IEEE Transactions on Information Theory* 56, 11 (2010), 5847–5861.
- [126] OCHIENG, P. Speech separation based on contrastive learning and deep modularization. *arXiv preprint arXiv:2305.10652* (2023).
- [127] O’CONNOR, M., KLEIJN, W. B., AND ABHAYAPALA, T. Distributed sparse mvdr beamforming using the bi-alternating direction method of multipliers. In *2016 IEEE International Conference on Acoustics, Speech and Signal Processing (ICASSP)* (2016), IEEE, pp. 106–110.

- [128] PAN, C., CHEN, J., AND BENESTY, J. Theoretical analysis of differential microphone array beamforming and an improved solution. *IEEE/ACM Transactions on Audio, Speech, and Language Processing* 23, 11 (2015), 2093–2105.
- [129] PAPP, I. I., SARIC, Z. M., AND TESLIC, N. D. Hands-free voice communication with tv. *IEEE Transactions on Consumer Electronics* 57, 2 (2011), 606–614.
- [130] PARK, J., AND SANDBERG, I. W. Universal approximation using radial-basis-function networks. *Neural computation* 3, 2 (1991), 246–257.
- [131] PATEL, S. J., GRANT, S. L., ZAWODNIOK, M., AND BENESTY, J. On the design of optimal linear microphone array geometries. In *2018 16th International Workshop on Acoustic Signal Enhancement (IWAENC)* (2018), IEEE, pp. 501–505.
- [132] PEARSON, K. Contributions to the mathematical theory of evolution. *Philosophical Transactions of the Royal Society of London. A* 185 (1894), 71–110.
- [133] PETERSEN, K. B., PEDERSEN, M. S., ET AL. The matrix cookbook. *Technical University of Denmark* 7, 15 (2008), 510.
- [134] PHAM, D.-T. Fast algorithms for mutual information based independent component analysis. *IEEE Transactions on Signal Processing* 52, 10 (2004), 2690–2700.
- [135] POWELL, M. J. A method for nonlinear constraints in minimization problems. *Optimization* (1969), 283–298.
- [136] POWELL, M. J. D. *Approximation theory and methods*. Cambridge university press, 1981.

- [137] PRIEMER, R. *Introductory signal processing*, vol. 6. World Scientific Publishing Company, 1990.
- [138] REN, M., KORNBLITH, S., LIAO, R., AND HINTON, G. Scaling forward gradient with local losses. *arXiv preprint arXiv:2210.03310* (2022).
- [139] RÉNYI, A. On measures of dependence. *Acta mathematica hungarica* 10, 3-4 (1959), 441–451.
- [140] RESHEF, D. N., RESHEF, Y. A., FINUCANE, H. K., GROSSMAN, S. R., MCVEAN, G., TURNBAUGH, P. J., LANDER, E. S., MITZENMACHER, M., AND SABETI, P. C. Detecting novel associations in large data sets. *science* 334, 6062 (2011), 1518–1524.
- [141] RESHEF, D. N., RESHEF, Y. A., MITZENMACHER, M., AND SABETI, P. C. Cleaning up the record on the maximal information coefficient and equitability. *Proceedings of the National Academy of Sciences* 111, 33 (2014), E3362–E3363.
- [142] RESHEF, Y. A., RESHEF, D. N., FINUCANE, H. K., SABETI, P. C., AND MITZENMACHER, M. Measuring dependence powerfully and equitably. *The Journal of Machine Learning Research* 17, 1 (2016), 7406–7468.
- [143] ROSENBLATT, F. The perceptron: a probabilistic model for information storage and organization in the brain. *Psychological review* 65, 6 (1958), 386.
- [144] RUMELHART, D. E., HINTON, G. E., AND WILLIAMS, R. J. Learning representations by back-propagating errors. *nature* 323, 6088 (1986), 533–536.
- [145] SCHJÆR-JACOBSEN, H., AND MADSEN, K. Synthesis of nonuniformly spaced arrays using a general nonlinear minimax optimiza-

- tion method. *IEEE Transactions on Antennas and Propagation* 24, 4 (1976), 501–506.
- [146] SEJNOWSKI, T. J. *The deep learning revolution*. MIT press, 2018.
- [147] SHANAN, S., AND POMALAZA-RAEZ, C. The use of nonuniform element spacing in array processing algorithms. *The Journal of the Acoustical Society of America* 86, 4 (1989), 1416–1418.
- [148] SHEN, H., JEGELKA, S., AND GRETTON, A. Fast kernel-based independent component analysis. *IEEE Transactions on Signal Processing* 57, 9 (2009), 3498–3511.
- [149] SOHL-DICKSTEIN, J., WEISS, E., MAHESWARANATHAN, N., AND GANGULI, S. Deep unsupervised learning using nonequilibrium thermodynamics. In *International Conference on Machine Learning* (2015), PMLR, pp. 2256–2265.
- [150] SRIPERUMBUDUR, B. K., FUKUMIZU, K., GRETTON, A., SCHÖLKOPF, B., AND LANCKRIET, G. R. On the empirical estimation of integral probability metrics. *Electron. J. Statist* (2012).
- [151] SRIPERUMBUDUR, B. K., GRETTON, A., FUKUMIZU, K., SCHÖLKOPF, B., AND LANCKRIET, G. R. Hilbert space embeddings and metrics on probability measures. *Journal of Machine Learning Research* 11, Apr (2010), 1517–1561.
- [152] SRIVASTAVA, N., HINTON, G., KRIZHEVSKY, A., SUTSKEVER, I., AND SALAKHUTDINOV, R. Dropout: a simple way to prevent neural networks from overfitting. *The journal of machine learning research* 15, 1 (2014), 1929–1958.
- [153] SRIVASTAVA, R. K., GREFF, K., AND SCHMIDHUBER, J. Highway networks. *arXiv preprint arXiv:1505.00387* (2015).

- [154] STOLLER, D., EWERT, S., AND DIXON, S. Wave-u-net: A multi-scale neural network for end-to-end audio source separation. *arXiv preprint arXiv:1806.03185* (2018).
- [155] TRABELSI, C., BILANIUK, O., ZHANG, Y., SERDYUK, D., SUBRAMANIAN, S., SANTOS, J. F., MEHRI, S., ROSTAMZADEH, N., BENGIO, Y., AND PAL, C. J. Deep complex networks. In *International Conference on Learning Representations* (2018).
- [156] TU, Q., AND CHEN, H. On mainlobe orientation of the first-and second-order differential microphone arrays. *IEEE/ACM Transactions on Audio, Speech, and Language Processing* 27, 12 (2019), 2025–2040.
- [157] TU, Q., AND CHEN, H. Theoretical lower bounds on the performance of the first-order differential microphone arrays with sensor imperfections. *IEEE/ACM Transactions on Audio, Speech, and Language Processing* (2022).
- [158] VAN TREES, H. L. *Optimum array processing: Part IV of detection, estimation, and modulation theory*. John Wiley & Sons, 2002.
- [159] VAN TREES, H. L. *Optimum array processing: Part IV of detection, estimation, and modulation theory*. John Wiley & Sons, 2004.
- [160] VAN VEEN, B. D., AND BUCKLEY, K. M. Beamforming: A versatile approach to spatial filtering. *IEEE assp magazine* 5, 2 (1988), 4–24.
- [161] VINCENT, E., GRIBONVAL, R., AND FÉVOTTE, C. Performance measurement in blind audio source separation. *IEEE transactions on audio, speech, and language processing* 14, 4 (2006), 1462–1469.
- [162] VINCENT, E., VIRTANEN, T., AND GANNOT, S. *Audio source separation and speech enhancement*. John Wiley & Sons, 2018.

- [163] WANG, D., AND CHEN, J. Supervised speech separation based on deep learning: An overview. *IEEE/ACM Transactions on Audio, Speech, and Language Processing* 26, 10 (2018), 1702–1726.
- [164] WANG, S., KONG, X., PENG, X., MOVASSAGH, H., PRAKASH, V., AND LU, Y. Dasformer: Deep alternating spectrogram transformer for multi/single-channel speech separation. *arXiv preprint arXiv:2302.10657* (2023).
- [165] WANG, X., HUANG, G., COHEN, I., BENESTY, J., AND CHEN, J. Robust steerable differential beamformers with null constraints for concentric circular microphone arrays. In *ICASSP 2021-2021 IEEE International Conference on Acoustics, Speech and Signal Processing (ICASSP)* (2021), IEEE, pp. 4465–4469.
- [166] WATANABE, S. Information theoretical analysis of multivariate correlation. *IBM Journal of research and development* 4, 1 (1960), 66–82.
- [167] WRIGHT, S., NOCEDAL, J., ET AL. Numerical optimization. *Springer Science* 35, 67-68 (1999), 7.
- [168] WU, Y., WANG, H., ZHANG, B., AND DU, K.-L. Using radial basis function networks for function approximation and classification. *ISRN Applied Mathematics 2012* (2012).
- [169] XU, Y., DU, J., DAI, L.-R., AND LEE, C.-H. A regression approach to speech enhancement based on deep neural networks. *IEEE/ACM Transactions on Audio, Speech, and Language Processing* 23, 1 (2015), 7–19.
- [170] YAN, L., HUANG, W., KLEIJN, W. B., AND ABHAYAPALA, T. D. Phase error analysis for first-order linear differential microphone arrays. In *2022 17th International Workshop on Acoustic Signal Enhancement (IWAENC)* (2022), IEEE.

- [171] YAN, L., HUANG, W., KLEIJN, W. B., AND ABHAYAPALA, T. D. Neural optimization of geometry and fixed beamformer for linear microphone arrays. In *ICASSP 2023-2023 IEEE International Conference on Acoustics, Speech and Signal Processing (ICASSP)* (2023), IEEE, pp. 1–5.
- [172] YAN, L., KLEIJN, W. B., AND ABHAYAPALA, T. A linear-time independence criterion based on a finite basis approximation. In *International Conference on Artificial Intelligence and Statistics* (2020), PMLR, pp. 202–212.
- [173] YAROTSKY, D. Error bounds for approximations with deep relu networks. *Neural Networks* 94 (2017), 103–114.
- [174] YU, J., AND DONOHUE, K. D. Performance for randomly described arrays. In *2011 IEEE Workshop on Applications of Signal Processing to Audio and Acoustics (WASPAA)* (2011), IEEE, pp. 269–272.
- [175] ZARZOSO, V., COMON, P., AND PHLYPO, R. A contrast function for independent component analysis without permutation ambiguity. *IEEE transactions on neural networks* 21, 5 (2010), 863–868.
- [176] ZHANG, H., CHEN, J., AND BENESTY, J. Study of nonuniform linear differential microphone arrays with the minimum-norm filter. *Applied Acoustics* 98 (2015), 62–69.
- [177] ZHAO, L., BENESTY, J., AND CHEN, J. Design of robust differential microphone arrays. *IEEE/ACM Transactions on Audio, Speech, and Language Processing* 22, 10 (2014), 1455–1466.
- [178] ZHAO, L., BENESTY, J., AND CHEN, J. Design of robust differential microphone arrays with the jacobi–anger expansion. *Applied Acoustics* 110 (2016), 194–206.

- [179] ZHAO, S., AND MA, B. D2former: A fully complex dual-path dual-decoder conformer network using joint complex masking and complex spectral mapping for monaural speech enhancement. *arXiv preprint arXiv:2302.11832* (2023).
- [180] ZOLTOWSKI, M. D., HAARDT, M., AND MATHEWS, C. P. Closed-form 2-d angle estimation with rectangular arrays in element space or beamspace via unitary esprit. *IEEE Transactions on Signal Processing* 44, 2 (1996), 316–328.